

AUTONOMOUS NAVIGATION OF UNKNOWN PIPE NETWORKS

A THESIS SUBMITTED TO THE UNIVERSITY OF MANCHESTER
FOR THE DEGREE OF DOCTOR OF PHILOSOPHY
IN THE FACULTY OF SCIENCE AND ENGINEERING

2019

By
Liam R Brown
School of Electrical and Electronic Engineering

Contents

Acronyms	10
Units	12
Declaration	14
Copyright	15
List of Publications	16
Acknowledgement	17
The Author	18
1 Introduction	19
1.1 Pipe Networks	22
1.2 Pipe Inspection Robots	24
1.2.1 Challenges	24
1.3 Aim and Objectives	25
1.4 Thesis Structure	26
1.5 Contribution	26
2 Literature Review	29
2.1 Pipe Inspection	29
2.1.1 Alternative Methods of Pipe Inspection	30
2.2 Pipe Inspection Robots	30
2.2.1 Pipe Inspection Gauge	31
2.2.2 Wheeled	32
2.2.3 Tracked	33

2.2.4	Walking	34
2.2.5	Inchworm	34
2.2.6	Spiral	35
2.2.7	Other	36
2.2.8	Discussion	36
2.3	Navigating Elbows with a Wall-Pressing Robot	38
2.3.1	Control Strategies for Navigating Elbows	39
2.4	In-Pipe Sensing	40
2.4.1	Elbow Parameters	40
2.4.2	Current In-pipe Sensing Methods	41
2.4.3	Feeler Sensors	43
2.5	Conclusion	45
3	Corner Parameter Estimation	47
3.1	System Architecture Overview	47
3.2	Local and Global Axes	48
3.3	In-Pipe Sensing Requirements	49
3.4	Feeler Sensor	50
3.5	Corner Parameter Estimation	50
3.5.1	Corner Direction Estimation	51
3.5.2	Corner Radius	57
3.5.3	Algorithm Triggering	59
3.6	Summary and Contribution	60
4	Corner Parameter Estimation Experiment	61
4.1	Experimental Hardware and Methodology	61
4.1.1	Feeler Sensor	62
4.1.2	Linear Translation Test Rig	64
4.1.3	Experimental Procedure	66
4.2	Results and Discussion	66
4.2.1	Results	66
4.2.2	Discussion	69
4.2.3	Effect of Manufacturing Tolerances on Prediction	70
4.2.4	Comparison Other Detection Systems	71
4.2.5	Scalability	71
4.3	Summary and Contribution	72

5	Robot Design and Development	73
5.1	Tracked In-Pipe Robots	74
5.2	Design Requirements and Constraints	75
5.3	Prototype Development	78
5.3.1	NIVALIS I	78
5.3.2	FURO I	80
5.3.3	NIVALIS II	81
5.4	Final FURO II Prototype	82
5.5	Summary and Contribution	88
6	Autonomous Elbow Navigation Control	89
6.1	Low-Level Control	90
6.2	Proposed Method Of Autonomous Elbow Control	91
6.2.1	Entrance	93
6.2.2	Traversing	95
6.2.3	Exit Conditions	97
6.3	Experimental Hardware and Method	100
6.4	Results and Discussion	102
6.4.1	Experimental Results	102
6.4.2	Discussion	108
6.5	Summary and Contribution	110
7	Pipe Network Visualisation	111
7.1	Introduction	111
7.2	Pipework Mapping and Reconstruction	112
7.3	Method	113
7.4	Simulation of Pipe Networks	120
7.4.1	Network	121
7.5	Simulation of Hotspot Detection within a Pipe Network	122
7.6	Extension To Different Junction Types	123
7.7	Visualisation of Real Data	124
7.8	Limitations	125
7.9	Summary and Contribution	127
8	Conclusion and Further Work	129
8.1	Summary	129

8.2	Thesis Analysis	130
8.2.1	Corner Parameter Estimation	131
8.2.2	In-pipe Obstacles and Junctions	131
8.2.3	Sensing and Visualisation	132
8.2.4	Environmental Hardening	133
8.2.5	Tether and Communication	133
8.2.6	Retrieval and Autonomous Control	134
8.2.7	Miniaturisation	135
8.3	Contribution to Field	135
9	Appendix	137
9.1	Electronic Appendix	137
9.2	Figures	138
9.3	Tables	140
	Bibliography	142

Word Count: 38596

List of Tables

2.1	Overview of locomotion types	37
2.2	Design parameters of wheeled and tracked, differential drive robots . .	37
2.3	Control of elbows	39
2.4	Current in-pipe sensor suits	42
2.5	Comparison of bio-inspired whiskers and custom feelers	44
4.1	Linear translation test rig specification	65
4.2	Predicted angles of the multiple passes for $\theta_d = -70^\circ$	68
4.3	Comparison of sensor cost for elbow detection	71
5.1	Design parameters tracked, differential drive robots	74
5.2	Coefficient of static friction of the selected tracks on various materials	76
5.3	Coefficient of rolling friction of the selected tracks on various materials	77
5.4	Parameters of the custom in-pipe robots developed for this project . .	88
6.1	Low-level controller PID gains	90
6.2	AEC experimental conditions	102
6.3	Comparison of target and calculated drive unit velocities	103
6.4	Average time taken for the FURO prototype to turn through an elbow .	107
7.1	Feature parameters for the network	121
7.2	Estimated corner parameters for visualisation system	126
9.1	Design parameters of wheeled and tracked, differential drive robots . .	140
9.2	Design parameters tracked, differential drive robots	141

List of Figures

1.1	Photo of pipework from an exemplar facility	21
1.2	Nuclear life cycle	21
1.3	Short and long elbow	23
2.1	Pipe vehicle categories	31
2.2	PIG robot	32
2.3	Wheeled robot - MRINSPECT VI	32
2.4	Tracked robot - PAROYS-II	33
2.5	Walking robot - MORTIZ	34
2.6	Inchworm robot	35
2.7	Spiral robot	35
2.8	Wheeled/snake hybrid robot - AiRo-II	36
2.9	Corner parameter definitions	40
3.1	Autonomous elbow controller overview	48
3.2	Global and local axes	48
3.3	Simplified diagram of feeler	50
3.4	Corner entrance	51
3.5	Corner entrance for short elbow with samples S labelled	52
3.6	Corner direction stages	52
3.7	Kinematic model of feelers	53
3.8	Feeler end points layout in (y, z) plane	54
3.9	Sample changes in (y, z) plane	55
3.10	Combination of sample changes in (y, z) plane	56
3.11	Diagram of leg layout and robot and feeler centre points	57
3.12	Empirical approximation for calibrating θ_{fm}	58
3.13	Using Intersecting Chords Theorem (ICT) to determine corner radius	59
4.1	Simplified diagram of feeler	62

4.2	Feeler sensor for corner direction estimation experiment	63
4.3	Plot of change in angle vs feeler length	63
4.4	Feeler data for a straight section of pipe	64
4.5	Simplified diagram of test rig	64
4.6	Simplified diagram of test rig	65
4.7	Leg layout of feelers at start (S_1) and end of corner (S_n) entrance for $\theta_d = -70^\circ$	67
4.8	A single pass (Pass 5) of raw feeler angle data at $\theta_d = -70^\circ$	67
4.9	Mean estimated angles Vs target angle	69
5.1	Largest robot dimensions to fit around a short elbow	75
5.2	Evolution of design improvements through the prototypes	78
5.3	NIVALIS I tracked prototypes	79
5.4	Offset and central track alignment	79
5.5	FURO I tracked prototype	80
5.6	NIVALIS II tracked prototypes	81
5.7	System architecture diagram	83
5.8	Simplified diagram of wall-pressing assembly	84
5.9	Force diagram of wall-pressing	85
5.10	FURO II varying diameter	86
5.11	Diagram to show drive wheel radius selection to minimise size whilst giving 1 mm clearance	87
5.12	Labelled diagram of drive unit	87
5.13	FURO II prototype	88
6.1	Output of the PID controller	91
6.2	Autonomous elbow control stages	92
6.3	Autonomous elbow controller overview updated	93
6.4	Calculating radii	94
6.5	Impulse vs angle of entry	96
6.6	Impulse vs angle of entry	97
6.7	2D simplified diagram of exit conditions	98
6.8	Kinematic model of exit conditions	99
6.9	Feeler angles of exit conditions	99
6.10	Change in d_{yz} as the robot exits the corner	100
6.11	Test rig for Autonomous Elbow Controller	101

6.12	Modified feeler sensor	102
6.13	FURO-II prototype navigating corner at entrance angle $\theta_d = 0^\circ$	104
6.14	Estimated of direction during Autonomous Elbow Controller testing .	105
6.15	Time taken to turn using Autonomous Elbow Controller	106
6.16	Time taken to turn using Brute Force	106
6.17	Real change in d_{yz} when navigating elbow	108
7.1	Basic example of pipe network	114
7.2	Basic example of pipe network (2/2)	115
7.3	Transform of elbow from basic example of pipe elbow	116
7.5	Pipe visualisation with varying elbow direction θ_d and angle ϕ_a	119
7.4	Pipe visualisation example	120
7.6	Visualisation of the network	121
7.7	Visualisation of Network 2 with radiation hotspots	122
7.8	Network with T-junction	123
7.9	Visualisation of real and simulated data	125
9.1	Corner Prediction Flow Chart	138
9.2	PID Controller Architecture	139
9.3	Closed-loop Control Architecture	139

Acronyms

2D Two Dimensional. 8, 41, 42, 98

3D Three Dimensional. 43, 78, 80–82, 86, 112–114

ABS Acrylonitrile Butadiene Styrene. 43

AEC Autonomous Elbow Controller. 6, 9, 27, 89–93, 95, 101–103, 105–107, 109, 110, 124, 127, 129, 130, 132, 136

BF Brute Force. 9, 38, 82, 89, 95–97, 101–103, 105–107, 109, 110, 130

CCD Charged-Coupled Device. 41, 42

CoB Centre of Body. 98, 118, 120

DNF Did Not Finish. 105–107

DU Drive Unit. 39, 47, 48, 61, 74, 77, 78, 81–83, 86, 89, 90, 92–95, 97, 106, 108–110, 117, 118, 120, 132

FDM Fused Deposition Modelling. 78, 80

HLW High Level Waste. 20

I2C Inter-integrated Circuits. 82

ICT Intersecting Chords Theorem. 7, 57–59

ILW Intermediate Level Waste. 20

IMU Inertial Measurement Unit. 39, 112, 113, 126, 127, 132, 135

IR Infrared Radiation. 42

LLW Low Level Waste. 19, 20

LSA Laser Spot Array. 41, 42

PCB Printed Circuit Board. 86

PIC Pipe Inspection Crawler. 74, 79, 141

PIG Pipe Inspection Gauge. 2, 7, 30–32, 36, 112

PLA PolyLactic Acid. 78–81, 88

POCO Post Operational Clean Out. 22, 23, 133

POT Potentiometer. 43, 44, 62, 64, 70, 71, 101, 108

PSD Position Sensitive Device. 39, 41, 42

PTFE Polytetrafluoroethylene. 133

RF Radio Frequency. 134

ROS Robotics Operating System. 27, 82

SLA Stereolithography. 81, 88

SPI Serial Peripheral Interface. 82

UK United Kingdom. 19, 22, 23

US ultrasonic. 39, 42

VLLW Very Low Level Waste. 19, 20

Units

% Percent. 31, 38, 59, 61, 64, 66, 70, 112

° Degree. 6, 8, 9, 26, 41, 42, 57, 61, 64–72, 74, 84, 93, 96, 97, 99–104, 106, 108, 109, 111, 113, 114, 117–119, 121, 124, 125, 127, 129, 131, 135

£ Great British Pound. 19, 27, 71, 79, 80

bq Becquerel. 20

inch Inch. 32, 113, 132

kg Kilogram. 37, 74–76, 140, 141

m Meter. 8, 22, 24–27, 29, 32–38, 41–44, 62–64, 66, 68–75, 77, 79–81, 85–88, 98, 100–102, 108, 109, 111–113, 117, 119, 122, 124, 127, 129, 131–133, 135, 136, 140, 141

ms⁻¹ Meters per Second. 37, 74, 75, 102, 103, 140, 141

ms⁻² Meters per Second Squared. 76

N Newton. 76, 77, 83, 96, 105

Nm Newton Meter. 77, 85

Ns Newton Second. 27, 97, 105, 107, 109, 110, 130, 136

ppr Pulse Per Rotation. 101

s Second. 103, 105, 107, 109

Abstract

Nuclear decommissioning is forecast to cost the UK £121 billion over the next 120 years. This is due to the hazardous environment nuclear material creates making it very expensive to dispose of. In a large number of legacy facilities their contents is unknown and thus must be treated as contaminated waste, unless it is characterised. The aim of this project is to develop an in-pipe robot that can aid in characterisation by autonomously travelling along the unknown pipe networks and recording their geometric data. This enables a map to be generated with the radiation hotspots identified.

A key limitation of similar existing systems is the traversal through elbows and junctions. Their primary cornering method is brute force, which can lead to early fatigue and damage to the robots. To allow a robot to safely travel through unknown pipe networks a controlled method for turning is required.

The solution to overcome this challenge is the robust, novel wall-pressing robot FURO II, which has been designed and built as part of this project. This 150 mm diameter robot features both active and passive wall-pressing and is able to pass through elbows. It acted as the test platform for the developed control system.

The parameters of unknown corners have to determine before a control action can be determined. This is achieved with a novel, low-cost set of feeler sensors and an accompanying algorithm that is able to identify the corner direction with an absolute mean error of 4° , and is the only system to practically estimate the corner radius.

These estimated parameters are used as part of an autonomous elbow controller which was tested on FURO II. The controller showed a significant improvement over the brute force method with a reduction in the impulse applied to the robot of 213.97 Ns.

A method to visualise the captured data from the robot is proposed and showed to work on the captured data from the previous testing.

To summarise, this thesis presents a successful autonomous elbow controller for the navigation of small diameter pipe networks with unknown maps for an in-pipe, wall-pressing, differential drive robot.

Declaration

No portion of the work referred to in this thesis has been submitted in support of an application for another degree or qualification of this or any other university or other institute of learning.

Copyright

- i. The author of this thesis (including any appendices and/or schedules to this thesis) owns certain copyright or related rights in it (the “Copyright”) and s/he has given The University of Manchester certain rights to use such Copyright, including for administrative purposes.
- ii. Copies of this thesis, either in full or in extracts and whether in hard or electronic copy, may be made **only** in accordance with the Copyright, Designs and Patents Act 1988 (as amended) and regulations issued under it or, where appropriate, in accordance with licensing agreements which the University has from time to time. This page must form part of any such copies made.
- iii. The ownership of certain Copyright, patents, designs, trade marks and other intellectual property (the “Intellectual Property”) and any reproductions of copyright works in the thesis, for example graphs and tables (“Reproductions”), which may be described in this thesis, may not be owned by the author and may be owned by third parties. Such Intellectual Property and Reproductions cannot and must not be made available for use without the prior written permission of the owner(s) of the relevant Intellectual Property and/or Reproductions.
- iv. Further information on the conditions under which disclosure, publication and commercialisation of this thesis, the Copyright and any Intellectual Property and/or Reproductions described in it may take place is available in the University IP Policy (see <http://documents.manchester.ac.uk/DocuInfo.aspx?DocID=487>), in any relevant Thesis restriction declarations deposited in the University Library, The University Library’s regulations (see <http://www.manchester.ac.uk/library/aboutus/regulations>) and in The University’s policy on presentation of Theses

List of Publications

Published

- L. Brown, J. Carrasco, S. Watson, and B. Lennox, 'Elbow Detection in Pipes for Autonomous Navigation of Inspection Robots', *Journal of Intelligent & Robotic Systems*, pp. 1-15, Aug. 2018.
- F. Arvin, B. Bird, L. Brown, W. Cheah, A. Di Buono, J. Espinosa, K. Gornicki, A. Griffiths, K. Groves, A. Gupta, J. Jones, B. Lennox, H. Martin, M. Nancekivill, S. Tournier, T. Wright, S. Watson, 'Robotic Platforms for Remote Access and Sensing Applications for Nuclear Decommissioning', *Waste Management Symposium*, 2018.
- L. Brown, J. Carrasco, S. Watson, B. Lennox, 'FURO: Pipe Inspection Robot for Radiological Characterisation', *UK-RAS Proceedings*, pp. 56-58, Dec. 2017.
- F. Arvin, O. Ayoola, B. Bird, L. Brown, J. Carrasco, W. Cheah, J. Espinosa, P. Green, A. Griffiths, B. Lennox, S. Watson, T. Wright, 'Mobile Robots and Remote Characterisation Systems for Nuclear Decommissioning', *Waste Management Symposium*, 2016.

Submission Pending

- L. Brown, J. Carrasco, S. Watson, and B. Lennox, 'Autonomous Elbow Controller For A Differential Drive Pipe Inspection Robot', *Journal of Robotic and Autonomous Systems*.

Acknowledgement

I would sincerely like to thank my two supervisors, Simon and Joaquin. Without their guidance and help, I would never have ended up with a completed thesis or research of any merit.

I would also like to thank the workshops in SSB, without them it would have been impossible. The mechanical workshop who not only did an fantastic job of making all the robots I designed but also gave me guidance with the problems I faced and the PCB lab who never seemed to mind the endless revisions of boards sent their way. Thank you, Paul, Chris, Alan, Danny, Derrick, Gary and the rest.

A notable mention should be the support I've had from my wife. Her helping hand throughout the whole process has kept me just sane enough to have finished it.

A final word to all the others that aren't mentioned but have helped me throughout, for the many brews and supporting words, thank you all very much.

The Author

The author completed an MEng in Electrical and Electronic Engineering at the University of Manchester in 2015. Following this, began research into pipe inspection robots. The primary focus of this was the autonomous navigation of unknown pipe networks and the development of sensors for this task.

Chapter 1

Introduction

Nuclear decommissioning is a worldwide issue forecast to cost the United Kingdom (UK) alone £121 billion over the next 120 years [1]. This is due to the number of legacy sites that require decommissioning and the large cost to safely dispose of nuclear material.

The legacy sites date back to the 1930s from the discovery and early research into fission [2]. The initial interest in the nuclear industry was in weaponry, but later the technology was also used to create power stations. An example of this is the Sellafield site. It started its life as a munitions factory for the war effort, then in 1956 opened Calder Hall. This became the first nuclear power station connected to a national grid that could provide electricity on a commercial scale and operated until 2003. Calder Hall and its sister plant Windscale were combined and renamed Sellafield [3].

The Sellafield site also contains reprocessing facilities to recover the component parts of the spent nuclear fuel [4]. Calder Hall, as well as many other retired facilities now require decommissioning. For many of the old buildings the blueprints as well as records of the material they contain have been lost [4]. There is a major challenge to identify this information so that the facilities can be decommissioned.

It is important to know the contents of a building when it is being decommissioned, such that the waste can be correctly disposed of. It is categorised into four different types:

Very Low Level Waste (VLLW) or free release has very little activity limits for its radiation levels. VLLW can be disposed of at landfill sites [5].

Low Level Waste (LLW) contains relatively low levels of radiation. They are

mostly industrial items that have picked up traces of radiation from clean-up and maintenance activities, such as mops, cloths etc. To be classed as low level waste the radiation must not exceed 4 Gbq per tonne of alpha activity or 12 Gbq per tonne of beta/gamma [5]. LLW is compacted and sent for long-term storage in specially designed sites [6].

Intermediate Level Waste (ILW) exceeds the radiation levels of the LLW but does not pose a risk with the heat it generates [5]. Is mostly made up from reactor components that have had direct, long-term contact with the fuel. This material is mixed with a grout and stored in stainless steel drums to form a solid stable form. It is then placed in long-term storage [4].

High Level Waste (HLW) is highly radioactive and is often spent fuel from reactors. It is defined as waste which causes a significant temperature rise due to its radioactivity [5]. This waste is processed by drying it to a powder, mixing it with glass and melting it down into stainless steel containers before being stored using specialised methods to manage the heat levels [4].

Each waste level becomes increasingly expensive to dispose of, with VLLW being the cheapest and HLW being the most expensive. The reason why characterisation is important is because if there is any uncertainty in the radioactivity of an item it must be treated as HLW. This means if uncharacterised, the cost of disposing of the material increases dramatically. As such there is significant work being undertaken to characterise the facilities being decommissioned.

The current method of characterisation involves sending workers into the potentially hazardous zones to manually dismantle and scan the contents for traces of radiation. Due to the hazardous environment, the workers have to wear full air-fed Hazmat suits [7]. Their suits can be very uncomfortable and hot to wear making unpleasant working conditions. As well as this, there is a risk to the workers when sending them into these facilities, as they could be exposed to radiation if an accident were to occur.

The process of sending workers into these environments also generates large amounts of secondary waste. These are items that have to be disposed of because they have been exposed to, and therefore could have picked up traces of radiation, such as the workers' suits and tools taken into the facilities. This secondary waste then has to be disposed of, often classed as LLW.

A commonality between all the facilities, whether used for weapons manufacturing or power generation is the miles of pipework they contain. This pipework forms part of the decommissioning challenge and is the focus of this research.



Figure 1.1: Photo of pipework from an exemplar facility

Figure 1.1 shows a photo taken of pipework requiring decommissioning in an exemplar facility. Each section of pipework requires dismantling and scanning. If a low-cost, robotic solution existed to aid the workers in their task of characterising the pipework, it could help reduce the cost of decommissioning and reduce the time spent by the workers in the hazardous zones as well as the amount of secondary waste created. The development of this robotic solution is the overriding vision for the project.

The environment inside these pipe networks can be unpleasant, as they are in the final stages of the nuclear life cycle. To determine the potential hazards faced by the robotic system, the full life cycle is reviewed.

Nuclear Life Cycle

The stages of the nuclear life cycle is shown in Figure 1.2 as given in [7].

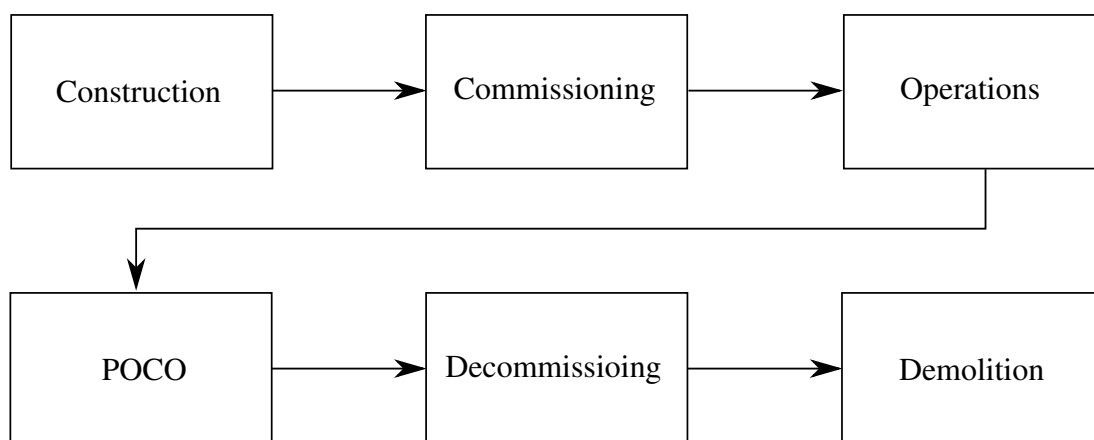


Figure 1.2: Nuclear life cycle

Each stage is expanded upon below,

- **Construction**, this is the design and building of the facility, no active material is in the plant at this point.
- **Commissioning**, is split into two main sections, the testing of the physical structure of the plant, then the introduction of nuclear materials.
- **Operations**, this is the running of the facility, completing whatever purpose it is designed for.
- **POCO**, Post Operational Clean Out (POCO) is completed when the site is shutting down. It is the removal of as much of the active material as possible. During this process, the pipework is flushed with highly acidic liquid to try to dissolve any traces of radioactive materials left in the pipes.
- **Decommissioning**, the final characterisation, removal then disposal of all the remaining nuclear material. The decommissioning stage is the focus of this research.
- **Demolition**, the removal of the building and supporting structure.

1.1 Pipe Networks

The pipework is reviewed in more detail to understand the operating environment for the robotic system being developed.

Like the legacy nuclear facilities, the pipework is generally unknown, specifically the structure of the networks. Some of the information available on the pipework networks is that standard-sized piping of between 50 - 150 mm in diameter was used.

The pipe networks can consist of vertical and horizontal sections of pipe as well elbows and other junctions. The lengths of the networks can vary dramatically, from small sections of a few meters between gloveboxes to much larger drainage systems, which in some cases can have runs for miles [8], [9].

It is assumed that the facilities are constructed to industrial standards, which constrain the material choices for the pipework as well as features such as elbow radius. The UK HSE (Health and Safety Executive) guide on the ‘Use of Pipeline Standards and Good Practice Guidance’ [10], follows the British Standard PD series of pipeline

standards or the European standards implemented in the UK as British Normative Standards (BS EN series). Specifically, the ‘Onshore Major Accident Hazard Pipelines - BS PD 8010 Part 1’ within the BS EN standards. It should be noted that these standards are for steel pipeline, which is likely the material used in the majority of the pipework but the exact materials are unknown. As various materials for pipework are used in construction such as plastics and other metals like cast iron. It will be taken as a general set of rules for the industrial pipework in the facilities this project is exploring.

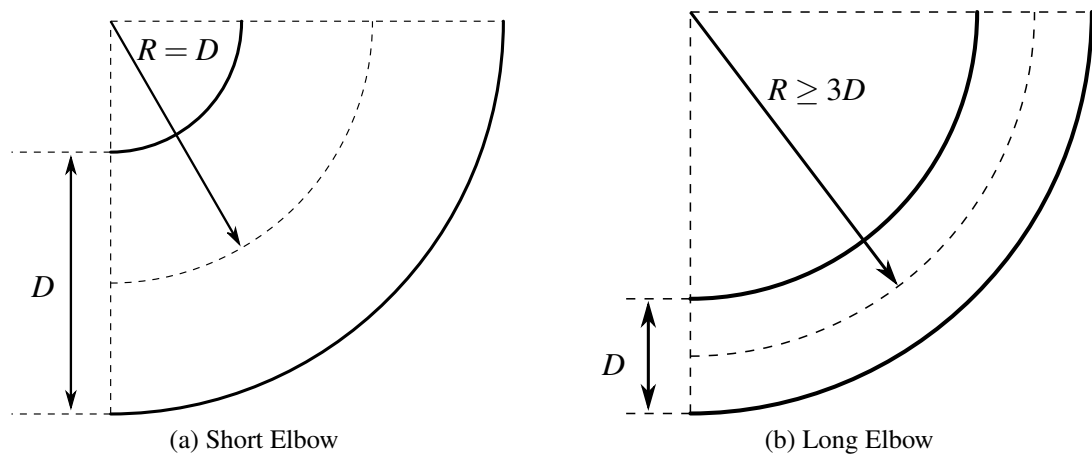


Figure 1.3: Short and long elbow

Elbows (or corners) can be classified into two types: long and short (Figure 1.3). A short elbow is the tightest bend within pipework and is not recommended to be used as the tighter a corner the larger resistance it has on the flow of the fluid within it. A short elbow is defined as the radius of the curve being equal to the diameter of the pipe. Note the radius of the curve is specified at the centre of the pipe. A long elbow is defined as the radius of the curve being equal to or greater than three times the pipe diameter.

As the pipework in the decommissioning stage of the nuclear life cycle (Section 1), it has undergone POCO. This means that most of the major radioactive sources are removed and only trace amounts remain. However, the environment inside these pipes is still hazardous.

Another effect of POCO is the possible pools of nitric acid left in recesses in the pipe networks. This could damage the robot as well as making traction more difficult. The pipework is likely to contain small amounts of debris that were not removed during POCO, however any major blockages would have been cleared.

As some of the facilities date back to the 1930s [2], the pipework could be corroded, fragile or damaged in sections.

As well as the characterisation application, pipe inspection could be used in other aspects of the nuclear life cycle, such as inspecting for maintenance purposes during operation. As well as other nuclear related applications, it could be used in a number of different industries. Oil, gas, water and sewage utilities all required miles of pipework to be regularly inspected. The robotic solution being developed for this project could be applicable in other industries and applications.

1.2 Pipe Inspection Robots

Pipework is abundant in buildings and infrastructure. It is a basic requirement for utility services as well as many other industries. All of this pipework requires inspection as damage to these pipes can cause large losses [11]. Robotic systems have been developed to speed up pipe inspection and make it more efficient [12]. As well as the utilities, the previous section highlights the need for robotic systems in the nuclear industry. The general challenges faced by robots navigating through pipework and the specifics for the nuclear industry are discussed in the following section.

1.2.1 Challenges

Navigating through pipework can be a difficult task, especially with small diameters. One major challenge of the project is the design of a robot which is able to navigate within 50 - 150 mm pipework.

Turning elbows within a pipe can also be a challenge for wall-pressing robots, which requires differential drive in order to turn [13]. Calculating this control action is a difficult task and any error in this will cause the robot to slip in the elbow and possibly damage or fatigue the robot [14].

For the pipework described in Section 1.1 there could be pools of acid in the pipes. Not only does this pose a challenge due to the effect of acid on the robot but surfaces of the pipes will be wet and could cause the robot to slip. Slippage could lead to the robot being unable to climb in sections of pipework causing it to get stuck.

Operating in an unknown environment is a challenge for any robotic system as the surroundings have to be detected. Not only does sensing these parameters pose a challenge for the system but the selection of sensors are also limited due to the size, budget and computational constraints. As the system will need to be disposed of once contaminated, it is required to be low cost.

Localisation within a network of pipes is another challenge that arises due to a lack of features in the pipework and orientation changes of the robot. This change in orientation is caused by small errors in the manufacturing of the robot, meaning the drive mechanisms are not aligned or there is an unsymmetrical weight distribution on the robot.

Some of the challenges highlighted above are targeted in the aim and objectives of this project.

1.3 Aim and Objectives

The aim of the project is to develop a robotic system that can autonomously navigate through unknown pipe networks, then produce a geometric map of the information gathered.

To achieve this aim a list of objectives have been created:

- Design and build a robot for navigating through pipe networks.
 - Research current in-pipe robots and identify the feasible designs for completing the aim.
 - Investigate current methods of in-pipe transportation and select the most feasible designs for prototyping at the larger 150 mm diameter.
 - Design and build a robotic platform.
- Develop autonomous controller for navigating through pipe networks.
 - Determine suitability of current control methods.
 - Identify requirements for the controller.
 - Develop method to determine the required information for the controller.
 - Test the controller on the robot previously developed.
- Visualisation of a geometric map of the data.
 - Review current mapping techniques and algorithms.
 - Develop visualisation system for viewing recorded data from the robot.
 - Test the system on captured data from the robot.

1.4 Thesis Structure

The thesis is structured as follows. First the literature is reviewed to highlight the challenges with cornering and present a robotic locomotion method which is best suited to meet the aim of the project (Chapter 2). It shows a controller is required and it is found that the parameters of the elbow are required to be sensed to be able to determine a control action. To identify them, a novel feeler sensor and accompanying algorithm is developed in Chapter 3. It is able to identify the corner direction and major radius. The proposed method is also tested on a real pipe elbow (Chapter 4).

A pipe inspection robot is developed for the task of turning elbows (Chapter 5). Once the corner parameters are determined the controller can be fully designed and tested on a prototype robot to confirm the method is successful (Chapter 6). Once the robot can successfully navigate elbows, work on visualising the captured data is completed. Chapter 7 presents a method to visualise large pipe networks and is tested on simulated and real data. Finally the summary and further work are presented in Chapter 8.

1.5 Contribution

This section summarises the four major contributions of the thesis:

1. The development of a sensor and algorithm for the purpose of elbow parameter estimation:

A novel feeler sensor is designed for the purpose of detecting the change in the pipe ahead of a robot. Alongside the feeler design is the development of an algorithm which takes the change from three feeler sensors and uses it to detect the parameters of an unknown elbow. The algorithm and sensor offers a low-cost solution (both computationally and financially) for estimating the parameters.

When practically tested, it is able to detect the corner direction with an absolute mean error of 4.69° . It is also able to estimate the radius with an absolute mean error of 0.91 mm. The solution offers a method that is scalable to any pipe diameter and specifically is suitable for small pipes with diameters of 50 mm. Comparing it to the literature gives a comparable error in terms of direction, but is able to function in small pipes. It also offers some practical results of radius prediction which is not offered by any of the literature.

2. A pipe inspection robot is designed for the task of navigating elbows:

FURO II is a novel, custom built, differential drive, wall-pressing, tracked robot which is able to operate within 150 mm pipes and with components costing less than £250. To develop the final design, four pipe inspection robots were constructed and tested in house with continual design and material improvement. It is largely constructed from aluminium to give a robust design to allow it to overcome the high forces generated when turning through elbows. The robot features both active and passive wall-pressing to allow it to passively overcome small obstacles as well as actively alter its diameter for different sized pipes. FURO II utilises off the shelf motors and belt kits to help reduce the cost of the robot and is controlled through the Robotics Operating System (ROS) framework.

3. An Autonomous Elbow Controller (AEC) is developed for the navigation of unknown elbows in a pipe:

It is identified that differential drive, wall-pressing robots required a control action to turn as the brute force method can lead to early fatigue of a robot. A controller is designed to overcome this issue. It takes the corner parameters previously estimated and determines the control action for a differential drive robot. It utilises the detection of exit conditions using the feeler sensor to determine the end of an elbow, thus allowing it to navigate through any corner angle.

FURO II is used as the test platform for the controller. The controller proves successful, allowing the robot to navigate through the corner 39 times. Comparing the results with the brute force method shows an improvement of 213.97 Ns applied to the robot when using the controller. This shows that the controller not only works but is able to safely navigate around unknown pipe elbows.

4. A visualisation system is designed to reconstruct the pipework the FURO II robot has navigated through:

The system uses homogeneous transformation matrices to generate the pipework. This allows large complex networks to be mapped and viewed. The system takes the sensor outputs from the robot, the encoder counts and feeler predictions. Using this it is able to determine the distances between landmarks (elbows, pipes, etc.) and generate the visualisation from their estimated parameters. The visualisation system is able to reconstruct complex networks from simulated data and able to accurately show the sections of pipework from the elbow controller tests.

Blank Page

Chapter 2

Literature Review

This chapter contains a review of the literature for pipe inspection robots, and identifies the challenges faced by them to navigate around elbows. It also provides the literature on sensing / detecting pipework.

The contribution of this chapter is the identification of the need for a controller to navigate a differential drive robot through an elbow. As well as the identification and selection of a feeler sensor for the detection of the elbow parameters.

2.1 Pipe Inspection

Pipework is crucial to modern life; having sewage systems, water, oil and gas to every house means a large amount of pipework is required. These pipes need to have scheduled inspection as defects in the pipe can lead to large losses [11]. Closing off and digging up sections of pipework to send humans in can be very expensive and time consuming [15]. Therefore pipe inspection robots have been developed. They started with systems that were basic, manually controlled and required large amounts of supporting equipment and workers to use them.

Using systems such as these was shown to be successful, but the time and cost of deploying these robots meant more new pipework was being laid than inspected. Due to this more efficient solutions were needed [12]. For some of these new systems, autonomous control was introduced to remove the need for as many workers.

These systems were designed for their specific application and pipe diameter. For oil pipelines, the robots vary in diameter from 200 - 500 mm [16], sewage pipes vary between 200 - 300 mm [17] and urban gas pipelines vary between 160 - 240 mm

[18]. As oil, gas and water pipe networks tend to be long straight sections of pipe, the autonomous systems had few challenges for the task of navigating them. They are also larger than the pipework in question for this project. As part of the development of these robots, many different types of locomotion were created. Each type of pipe inspection robot is reviewed in detail in Section 2.2.

An overview of alternate methods of pipe inspection are reviewed in the following section.

2.1.1 Alternative Methods of Pipe Inspection

The majority of pipe inspection is done with robots travelling down the pipelines. However, some other methods have been presented in the literature.

One method is sending workers into the hazardous facilities in fully air fed suits, to dismantle the pipework then scan with hand sensors. This is unpleasant, a potential risk to their health and there is a limited diameter of pipes they are able to inspect.

Acoustics can be used at the end of pipes to determine features about the network, such as distance to junctions and locations of obstacles [19]. Acoustic methods can be successful but cannot give details such as the direction of the pipeline only distances to features.

Robotic manipulators can also be used such as the complex snake like robots that have been summarised by Buckingham and Graham [20]. They can provide high quality scans of pipework and can also offer methods to dismantle them such as laser cutters [21]. Systems such as these require very large hardware for their deployment and are limited to short sections of pipework.

As the networks in question can have runs for miles (Section 1.1) the above solutions would not be suitable or would be very time and labour intensive, so pipe inspection robots have been selected.

2.2 Pipe Inspection Robots

Pipe inspection robots are commonly classified into different categories as presented in [11]. They are as follows, Wall-Pressing, Pipe Inspection Gauge (PIG), Tracked, Wheeled, Walking, Inchworm and Spiral. All of the categories are locomotion methods, with the exception of wall-pressing which is a feature of a robot. The categories are shown in Figure 2.1.

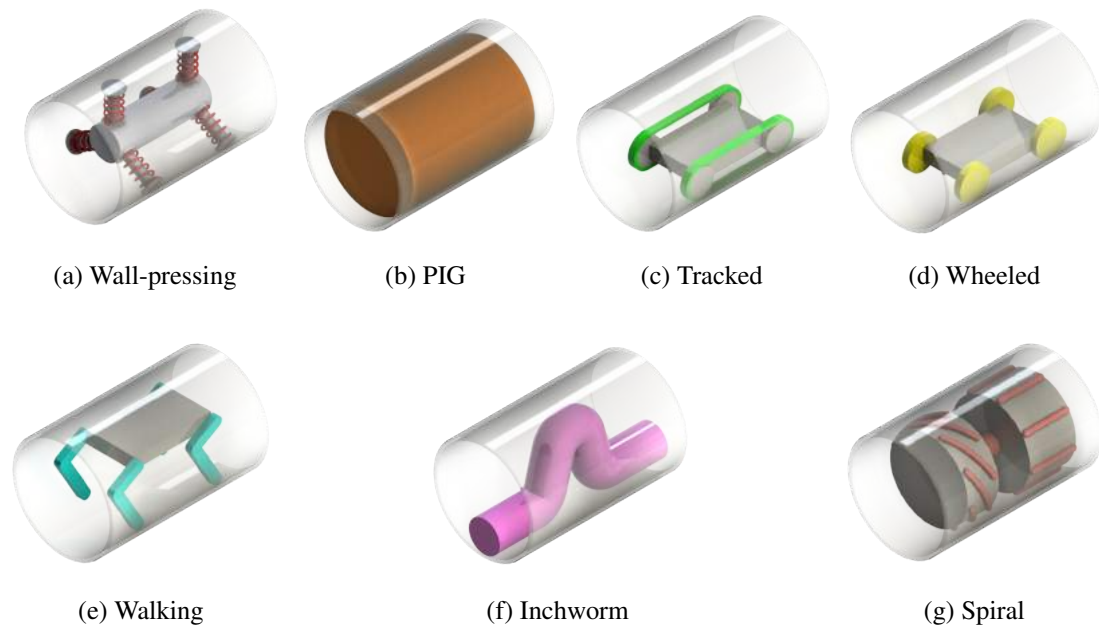


Figure 2.1: Pipe vehicle categories, as presented in [11]

Wall-pressing was first proposed on the MOGRER [22] and FERRET-1 [23] robots in 1987. Wall-pressing is the use of a force to press the robot into the walls of a pipe (Figure 2.1(a)). This gives the robot the ability to climb but adds complexity to the design with the extra actuation that is required. According to Mills et al. [24] it is used by 23 % of pipe inspection robots. Wall-pressing only describes if a robot can apply force on to pipe, an additional locomotion method is required to allow the robots to move. It will be required on this project to allow climbing.

Each of the locomotion categories from [11] are discussed in detail below and one identified for the design of the robot for this research.

2.2.1 Pipe Inspection Gauge

A PIG robot is a passive system that moves with the flow of fluids within a pipe [25] (Figure 2.2). PIGs are the most common in-pipe robot as they are widely used in the oil and gas industries to inspect and clean pipelines [26]. PIGs are very simple systems as they require very few to no moving parts for locomotion, which means they are easily scalable. As the PIG moves with the flow of the fluid it has little to no control in the direction it travels. The pipework in question contains no flowing fluids so the PIG would be unable to move and is unsuitable for this project.

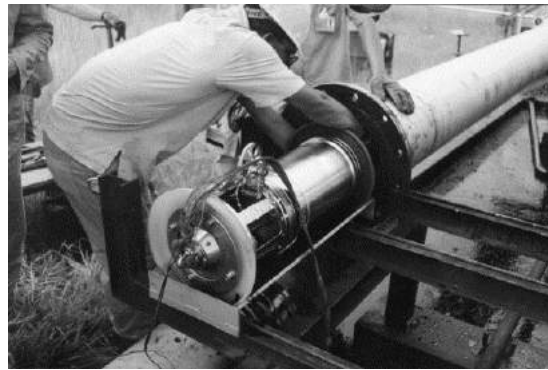


Figure 2.2: PIG robot, as presented in [25]

2.2.2 Wheeled

Wheeled robots use driven wheels as their method of propulsion. These are the most common form of self-propelling locomotion, and often have a similar designs combining six wheels in pairs with wall-pressing. An example is the MRINSPECT series [27] (shown in Figure 2.3) which uses that design to explore various methods of navigating within pipes. This configuration of robot is widely used as it offers wall-pressing and high mobility Choi and Ryew [28], Roh and Choi [14].



Figure 2.3: Wheeled robot - MRINSPECT VI, as presented in [27]

Wheeled vehicles can have simple designs which can easily be miniaturised down to smaller pipes. Hirose et al. [29] has developed the THES series of wheeled inspection robots in the 25 - 150 mm range and Suzumori et al. [30] has made an inspection robot to fit in a 1 inch pipe.

Other adoptions of wheeled systems include Yoon and Park's [31] robot which uses magnetic wheels to attract to the pipe surface. A commercially available version of this

is made by Honeybee [32] who also uses omni-wheels to increase the robot's mobility. The major downfall of the magnetic method is the need for ferrous pipes.

Wheels inherently have high energy efficiency for moving and have good mobility. However, they can suffer in environments with low friction and rough terrain.

2.2.3 Tracked

A tracked robot uses a band, timing belt, caterpillar track or similar that connects the wheels providing a greater area of contact to walls of the pipe and increasing grip [33]. Like wheeled systems, it is often combined with wall-pressing to give the ability to climb. Park et al. [34], [35] developed the PAROYS-II (shown in Figure 2.4), a three tracked radial layout robot with manoeuvrable segments within the tracks for increased control. This was designed for 400 – 700 mm diameter pipes.

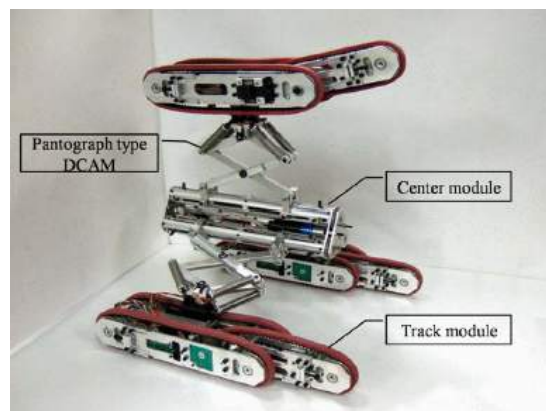


Figure 2.4: Tracked robot - PAROYS-II, as presented in [34]

Another variation of a tracked system using multiple segments is presented by Sato et al. [36], utilizing a very complex tracked system with independent control of each segment to give a very robust navigation ability within a pipe.

Tracked robots have good mobility and efficiency of locomotion, they also offer increased traction in comparison to the wheeled type. However, with the addition of a track they can face issues with derailing and increased design complexity making miniaturisation more difficult.

2.2.4 Walking

These use legs or similar, to walk through the pipe [37]. They are highly complex systems but offer very high mobility and can work in complex, rough in-pipe environments that other methods of transportation are unable to overcome [38]. The high complexity makes them very complicated systems in both design and control, causing them to be difficult to miniaturise. The MORTIZ robot [39] (shown in Figure 2.5), has simulated results to control the robot through junctions but can only operate in very large pipes of diameter 600 - 700 mm.

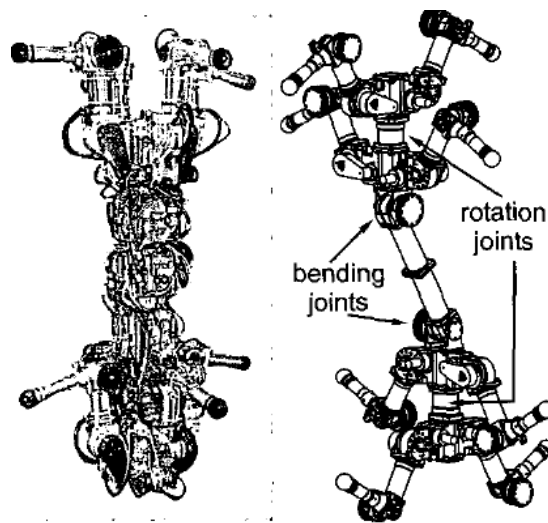


Figure 2.5: Walking robot - MORTIZ, as presented in [39]

Walking robots also require multiple motors for locomotion and thus have a large power usage. To reduce the number of legs and thus actuation Yu et al. [37] produced a walking system that uses two legs on one side and wheels on the other. This causes a problem when trying to navigate due to only being able to control the robot from one side of the pipe.

2.2.5 Inchworm

An inchworm robot uses the same principle of motion as the titled caterpillar to move, they require a minimum of two sections, a front and rear pod. The general process of movement is as follows: the back pod is locked in place then the front pod is translated up the pipe, which is then locked in place and the back pod detaches from the pipe and moves up to the front pod, the cycle then repeats [40]. A model of a typical inchworm is shown in Figure 2.6.

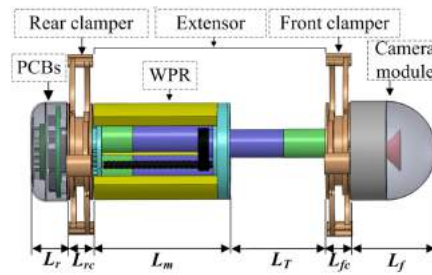


Figure 2.6: Inchworm robot, as presented in [40]

To allow long robots to navigate turns flexible joints can be added [41]. Due to their method of movement they have low motion efficiency but are highly stable systems and are often used in low friction environments. They do provide a challenge with control around junctions as extra actuation has to be added.

2.2.6 Spiral

A classic spiral drive system consists of a two-bodied design: a rotor and a stator. The stator has wheels pressed against the pipe walls, inline with its direction. The rotor has wheels at an angle to the pipe walls which, when the rotor is turned, drive the robot up the pipe in a spiral motion. This provides a very simple design requiring only one motor for locomotion. Due to this they can be easily miniaturised [42] (Figure 2.7).

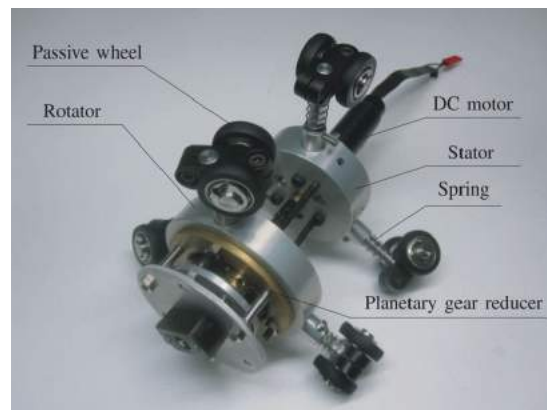


Figure 2.7: Spiral robot, as presented in [42]

A spiral drive system is inherently wall-pressing as it uses this to move. Due to their simplicity spiral drive systems have very limited navigation ability apart from forward and reverse. Kakogawa and Nishimura et al. [43], [44] have developed a modified spiral drive system able to navigate T-junctions in 125 mm pipes. However, it was experimentally found to have inconsistent results.

2.2.7 Other

There are other methods of locomotion which have their own unique advantages and disadvantages. Snake type robots move in a wave-like motion, very similar to an inchworm system on a basic level. An example of this is Suzumori et al [45]’s system for 55 – 331 mm pipes. These systems tend to be more complex and require large numbers of motors and thus energy to move.

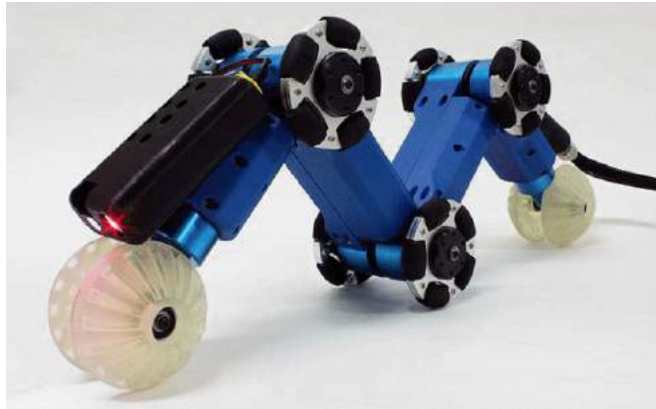


Figure 2.8: Wheeled/snake hybrid robot - AiRo-II, As Presented In [46]

Another example is a hybrid wheeled/snake type vehicle, AiRo-II [46] (Figure 2.8). It is able to pass around the corner without the need for differential drive. Despite having the advantage of easier cornering, it is a less stable platform for a sensitive sensor package, as the body is not in a fixed position within the pipe and it is not able to controllably select a direction at a junction.

2.2.8 Discussion

From the overview of each locomotion method, each type has been summarised in Table 2.1.

As the PIG is a passive system its locomotion efficiency is very high but it is unable to move under its own power (Denoted as ‘Passive*’ in Table 2.1). Due to this it is unsuitable for this project as there is no flow of fluids within the pipe. For overcoming junctions, both the spiral and the inchworm require major mechanical modifications to their designs.

Wall-pressing is a requirement for the robot as it must climb vertical pipes. This leaves wheeled, caterpillar and walking, all of which have high mobility. The pipework in question has diameters of 50 - 150 mm, as walking robots have very complex designs

Table 2.1: Overview of locomotion types

	Design Complexity	Ability to Navigate Junctions	Control	Locomotion Efficiency
PIG	Low	No	Simple	Passive*
Tracked	Medium	Yes	Average	Medium
Wheeled	Medium	Yes	Average	High
Walking	High	Yes	Complex	Very Low
Inchworm	Medium	Limited	Average	Low
Spiral	Low	Limited	Simple	Medium

making them difficult to miniaturise they are unsuitable. Therefore, the selected robot design is a wall-pressing, wheeled or tracked type.

The design parameters of the wall-pressing, wheeled or tracked robots summarised above are shown in Table 2.2. It can be seen that the robots vary dramatically in size and weight and very few of the systems are autonomous. A larger version of the table can be found in the Appendix Table 9.1.

Table 2.2: Design parameters of wheeled and tracked, differential drive robots

Robots		Size		Length	Number of		Wall-pressing		Maximum Speed	Weight	Tethered	Control	
		Diameter	Max		Drive Units	Drive Modules	Passive	Active				Autonomous	Manual
MRINSPECT VI [27]		150	200	-	3	1	Yes	No	-	-	Yes	Yes	-
Choi and Ryew [28]		160	240	-	3	2	Yes	No	-	-	Yes	Straights	Yes
MRINSPECT IV [14]		85	109	150	3	1	Yes	No	150	0.7	Yes	Yes	Yes
THES-II		50			2	2	Yes	No	-	-	Yes	No	Yes
THES-III [29]		100	200		4	1	Yes	No	-	-	Yes	No	Yes
Suzumari et al. [30]		23		110	2	1	No	Limited	6	0.016	Yes	No	Yes
Yoon and Park [31]		110		110	2	1	No	Magnetic	12	0.15	Yes	No	Yes
Kim et al. [33]		600	800	680	3	1	No	Yes	217	80	Yes	No	Yes
PAROYS-II [34]		400	700	390	3	1	Yes	Yes	41.7	7.8	-	Yes	-
Sato et al. [36]		69	-	-	1	variable	No	Yes	-	0.613	Yes	-	-

Navigating junctions: This can be a difficult task for pipe inspection robots, even those with manual control. Most pipe inspection robots are tele-operated and the appropriate direction at a junction can be selected using a camera. However, once the direction is known the junction must still be traversed. The focus of the thesis is navigating through an elbow junction, but other junction types will be discussed. The ability of wall-pressing robots to corner is discussed in the following section.

2.3 Navigating Elbows with a Wall-Pressing Robot

Most systems use the Brute Force (BF) method for cornering, i.e. there is no or little control on how to overcome junctions, the robot is driven as if it is in a straight section of pipe. Using BF causes extra forces to be applied to the robot as it pushes its way around the corner, which can lead to damage and early fatigue. As well as this it can also cause the robot to become lodged in the pipe. For this application of characterising nuclear-contaminated pipework it would be unsuitable to deploy a robot which is able to get stuck and become irretrievable.

Work has been completed on reducing the effect of the extra forces on the robot when using BF by making it compliant. The simplistic tracked robot from Nagase and Fukunaga [47], requires only one motor for navigating junctions, vertical sections and variable pipe diameters but as it is not differential drive it is unable to actively chose direction so is unsuitable.

Some wheeled and tracked systems use their design to allow them to corner. Both NIRVANA [48] and MRINSPECT VII [49] use multi-axis gear mechanisms that allow for the wheels to spin at different speeds, providing differential drive without the need of controlling individual motors. This solution contains very complex gear mechanisms that would be very difficult to miniaturise for a 50 mm pipe making it unsuitable for this application. They also would be unable to select a direction at a junction such as a T-junction, due to not having independent differential drive.

Wheeled and tracked type robots with wall-pressing require differential drive to allow them to corner [13]. In addition to this Roh and Choi [11] found the current consumption was increased by 10 % when no control was used and states “It can be concluded that the speed modulation of the differential-drive robot is very important for moving in the elbow.” (Roh and Choi [11]), showing there is a requirement for a method of cornering control when using a differential drive robot.

The major challenge with this is determining the control action required to corner which can be complex, and multiple approaches have been taken. Lee et al. [50] uses a double actuated joint to force the drive unit to stick to the centre of the elbow. This method essentially still uses BF but tries to control the position of the robot inside the elbow with an extra actuator. Zhang et al. [51] and Chen et al. [52] both analyse the kinematics of a wheeled robot to determine the wheel velocities. They provide a very complex solution to the problem and have no practical implementation. Chen et al. [52] again uses a kinematic model with a wheeled robot to determine the wheel velocities. Zhang and Wang [53] determine the optimal posture for a track robot turning an elbow

but do not use this to determine any control actions for the robot. These also all assume that the parameters of the corner are known.

Fully autonomous pipe inspection robots such as FAMPER [54] require a pre-determined map of the pipe network such that it is not required to sense the corners ahead. This is demonstrated to work, but for the use case of the research the pipe network is assumed to be unknown, so this method would be unsuitable.

There is a clear need to control the robots as they navigate around an elbow, with very few that will work in networks with very little or no prior knowledge. The following section contains a review of the controlled cornering methods with wall-pressing wheeled or tracked robots where the elbow is considered to be unknown.

2.3.1 Control Strategies for Navigating Elbows

There are only a very limited number of systems that can controllably navigate unknown elbows. Their elbow sensing and control methods are summarised in Table 2.3.

Table 2.3: Control of elbows

Robot		Sensors	Control
MRINSPECT	[55]	PSD with Camera	Velocities Calculated
Lee et al.	[56]	IMU	-
IPR-D300	[57]	US	Velocity Halved

MRINSPECT V [55] proposes using pose sensing after its prediction of corner parameters, measuring the change in its orientation to determine when the robot has turned the corner. There is very limited information on whether this method is viable as it requires a knowledge of the elbow angle such that the pose can be sensed for that change. As the pipework in question is unknown this is not suitable for this project.

Lee et al. [56] also used an Inertial Measurement Unit (IMU) to detect when the robot is in an elbow. By reviewing the change in angular velocity they can determine when the robot has exited the elbow. This work, despite being accurate, is unsuitable as the robot needs to have exited the corner so the end of the corner and the direction can be detected. This would mean the robot would have already completed the corner before the control action is calculated.

The IPR-D300 [57] uses ultrasonic (US) sensors to detect the wall distance from the Drive Unit (DU). When the distance passes a pre-set threshold the motor speed of that DU is halved. This offers some aid in turning, but it is a very inaccurate method of sensing and would still lead to large amounts of extra force being exerted on the robot.

They show images of the robot successfully navigating an elbow but this led to a track derailing which is likely an effect of the increased forces.

There is a clear gap in the literature for a controlled method of navigating an unknown small elbows with a differential drive, wall-pressing robot.

2.4 In-Pipe Sensing

To be able to determine the control action for the unknown elbow, the parameters of the elbow are required to be detected. The parameters of the elbow are summarised in the following section.

2.4.1 Elbow Parameters

The parameters of the elbow are reviewed to determine which of them the estimation system is required to predict.

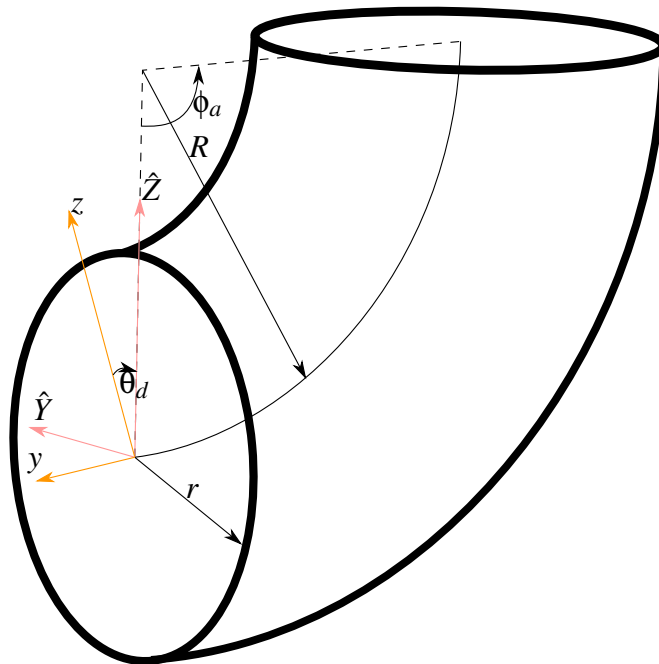


Figure 2.9: Corner parameter definitions

The required parameters to be determined are shown in Figure 2.9. It shows a pipe elbow with the variables defined. R is the major radius of the elbow also called the corner radius; r is the elbow minor radius or pipe radius; ϕ_a is the corner angle; the

difference between the local robot axis, z , and the corner axes, \hat{Z} is the corner direction, denoted as θ_d . A corner direction of $\theta_d = 0$ would mean the z and \hat{Z} axes are aligned.

In-pipe sensing is used for two different purposes: environmental observations and robot navigation. This section discusses the methods used to detect and characterise the pipework geometry for navigation and defines the sensor selected for use.

2.4.2 Current In-pipe Sensing Methods

Tamura et al. [58] utilise a Charged-Coupled Device (CCD) camera with ring type laser to detect junctions and defects within the pipe. However, they are not used to determine the parameters of the junctions. Kakogawa et al. [59] use a Laser Spot Array (LSA) and camera. They assume the radius of the pipe is known and state the accuracy of the system is inadequate, but they are able to identify junction types.

The IPR-D300 [57], has a more scalable solution which does not involve detecting the corner parameters as discussed in Section 2.3.1. Despite this method being unsuitable due to the lack of accuracy, similar techniques reviewing the change in the pipe can be considered.

Kim et al.'s [60] robot uses a Two Dimensional (2D) LIDAR to scan elbows and T-junctions. It is able to determine corner direction with a mean error of 0.64° ; this test was completed on two different corner angles. Despite the result being accurate the sensor itself has a package size of $75 \times 60 \times 60$ mm which is too large for the end goal of a 50 mm pipe. LIDAR sensors also have a minimum distance threshold of approximately 100 - 150 mm and are very costly which is problematic as the system is required to be disposable.

The most advanced in-pipe autonomous robots for unknown pipes are the MRINSPECT series [27]. They utilise Position Sensitive Device (PSD)s, lasers and a CCD camera to provide corner directional information. Early versions used a camera to detect the patterns of shadows for identifying landmarks within the pipe [55]. Using the PSDs they are able to detect corner direction and distinguish between a T-junction and mitre [61]. The camera and laser system is also able to determine features ahead in the pipe, including corner direction [62].

Both the PSDs and camera work in fixed radius pipe networks, although a method determining radius has been proposed [27]. This system has a mean error of 2.84° for predicting the angle of the corner direction.

Despite MRINSPECT's [27] method being computationally light, the requirement

of a camera and image processing would add an additional unwanted load to the system. They also utilised 6 - 8 Infrared Radiation (IR) sensors for the PSD system which would add further load in sampling and powering the sensors themselves. Their IR sensors also have a minimum range of 20 mm meaning they would be unsuitable for the 50 mm diameter pipe as for large segments of the junctions, they would be out of range. This method is proven to be successful and suitable for their application. However, this thesis will review an alternative method for detection which will be better suited for the intended application of 50 mm pipework.

Each of the discussed sensor systems are summarised in Table 2.4.

Table 2.4: Current in-pipe sensor suits

Robot		Sensors	Detection	Accuracy of Detection	
				Direction	Radius
Tamura et al.	[58]	CCD and Ring Laser	Defects	-	-
Kakogawa et al.	[59]	LSA and Camera	Direction	“Inadequate”	-
IPR-D300	[57]	US	Threshold	Inaccurate	-
Kim et al.	[60]	2D LIDAR	Direction	$\bar{\epsilon} = 0.64^\circ$	-
MRINSPECT	[27]	PSDs and CCD	Direction and Radius	$\bar{\epsilon} = 2.84^\circ$	-

There are very few sensor packages that are able to detect the required corner parameters, none of which are suitable for the proposed application. Therefore an in-pipe sensor for this purpose will be developed as part of this thesis. As MRINSPECT [27] and Kim et al. [60] are the only methods that give quantitative results, these will be used as a benchmark the sensor suite being developed. They express their results in mean error, the absolute mean error will be used as the metric in this analysis to allow comparison but with a fairer representation of the error.

As there are no suitable sensors in the literature other methods of detection are considered. An extrinsic sensor is required as the sensor parameters need to be determined before the robot enters the elbow. IR, ultrasonic (US), laser and cameras have been considered above. An alternative is a whisker-like sensor, despite not previously being used on in-pipe robots they can provide a suitable form factor for a small pipe and can be highly sensitive.

2.4.3 Feeler Sensors

Whisker sensors have been well researched, a good summary is provided by Pipe and Martin [63]. Their summary and others are expanded upon in the following section.

Kaneko and Tsuji [64] are able to achieve very high sensitivity ($5\ \mu\text{m}$) using a whisker and torque sensor. Their findings are that a curved whisker did not work for surface reconstruction with their torque sensor alone and only a straight-lined whisker sensor was suitable. They are able to detect surface irregularities irrespective of contact friction. Their sensor is made from piano wire, which is sufficient for their experiments but a more robust design will be required for the sensor being developed.

Jung and Zelinsky [65] as well as others are able to achieve robot navigation with them. Their design uses piano wire which when moved contacts a conductor to give a binary feedback of contact.

Russell [66] proposes a Potentiometer (POT) and spring system to determine the angle of the whisker when it has been moved. It was found to have “encouraging” (Russell [66]) results, the sensor provided a good visual representation of the object it was scanning. They conclude that a slight curve to the contact point of the whisker sensor similar to that of a cat will increase the likelihood of the tip touching the required object. Some error conditions are also discussed, when the body of the whisker contacts the object before the tip and when an object prevents the point from sliding which could lead to damaging the sensors.

The SCRATCHbot [67] uses a bank of 18 whisker sensors on a robotic head, they are 185 mm in length and have a tapering width from 2 - 0.5 mm. The Crunchbot is developed by the same team [67], it uses shorter whiskers (160 mm in length) made from Three Dimensional (3D) printed Acrylonitrile Butadiene Styrene (ABS) plastic to allow them to be more robust and be able to not break under high impacts. The design tapers down from 1.45 - 0.3 mm at the tip to mimic a rats whisker. However, the plastic is still very thin and a large force could damage these sensors.

Due to the research discussed above being bio-inspired with a thin whisker extending from a pivot point with detection method, it has led to their sensors being fragile. Due to the environment the pipe inspection robot is required to operate in (Section 1.1), a single point tipped feeler like this would be unsuitable. A more robust design is required. There are a limited number of other mechanical (none whisker) sensors which are reviewed below.

Cowan et al. [68] use a tactile passive sensor to mimic a cockroach’s antenna. Their sensors consists of a flexible beam designed to be bent and a flex sensor along it to use

tactile flow to determine. the rate at which it is approaching a wall so they can then follow it. It curves so that the arm is bent back along the wall, meaning it would be able to overcome defects or steps without getting stuck and breaking.

Lee et al. [69] also use a cockroach inspired sensor to follow a wall, this has a very robust design. It is made from a cured urethane casting compound with embedded flex sensors. This again uses a curved design to overcome defects in a wall.

Laperski et al. [70] provides a robust passive tactile sensor design from 3.2 mm laser cut plastic, a two-link sprung arm uses two POTs to provide angular feedback to allow a robot to follow a curved wall. Their design would be too large for an in-pipe robot and is complex but the sprung passive mechanism provides a good approach to keep the sensor following a wall.

Both bio-inspired and generic custom feeler sensors are compared in Table 2.5. It can be seen that custom feelers tend to be much more robust than the thin whisker type sensors, they can also be used to provide angular feedback which is desirable for this application. Being very thin, bio-inspired is both an advantage and a disadvantage compared to a large wheel, as they can have very high sensitivity to small changes but it also makes them weak.

Table 2.5: Comparison of bio-inspired whiskers and custom feelers

	Bio-Inspired Whisker	Custom Feeler
Feedback	On / off	Angular
Arm Robustness	Low / weak	High
Sensitivity	Very high	High
Contact Shape	Point	Wheel / curve

The literature shows that a feeler sensors are often bio-inspired which leads to a limited number of designs but it shows that they can offer a highly sensitive output and can work with various sizes of beam or arm. The required sensor for this project needs to be robust when contacting the pipe walls. Methods of using a curved arm poses one method of achieving this, however, others such as wheels have not been considered.

The feeler sensor shows it is a viable option for a detection system and is selected for further development.

2.5 Conclusion

Section 2.2 identifies that for the specified pipework a differential drive, wall-pressing wheel or tracked robot is required. The design and development of this robot is shown in Chapter 5. Section 2.3 highlights that there is a requirement for a control method when a differential drive, wall-pressing robots in turning through an elbows. To determine this control action the parameters of the elbow need to be sensed, Section 2.4 identifies a feeler sensor as the best detection system for further development. Chapter 3 presents the design of the feeler sensor and accompanying algorithm to estimate the parameters of the elbow so the control action can be determined. Finally the control action is estimated and tested in Chapter 6.

Blank Page

Chapter 3

Corner Parameter Estimation

There is a gap in the literature for an autonomous controller that is able to navigate differential drive, wall-pressing robots through small unknown pipe elbows (Section 2.3.1). It has been identified in Section 2.4.3 that to determine the control action, a feeler sensor to detect the corner parameters is required. This chapter presents an overview of the proposed controller as well as the design of the feeler sensors and the accompanying algorithm to estimate the corner direction and radius.

3.1 System Architecture Overview

As identified in Section 2.3 a controller is required for a differential drive robot to safely navigate through an elbow. This section presents the overview for an autonomous controller which will be developed as part of this project to reduce the forces applied to a robot when turning in an elbow.

As the controller doesn't know its environment, it must be able to sense the information it requires. This will allow it to appropriately determine a control action to be able to safely navigate through the corner. The output of the controller will be the velocities of each of the robots DUs. Once in the elbow it will try to detect exit conditions of the corner to allow it to enter the straight pipe again. The state machine for this controller is shown in Figure 3.1.

The controller shows various states which form the bases of the structure of the thesis. This chapter proposes a sensor and algorithm to determine the required parameters for the control system. Chapter 6 presents the full elbow traversing controller and tests the full system on a pipe inspection robot.

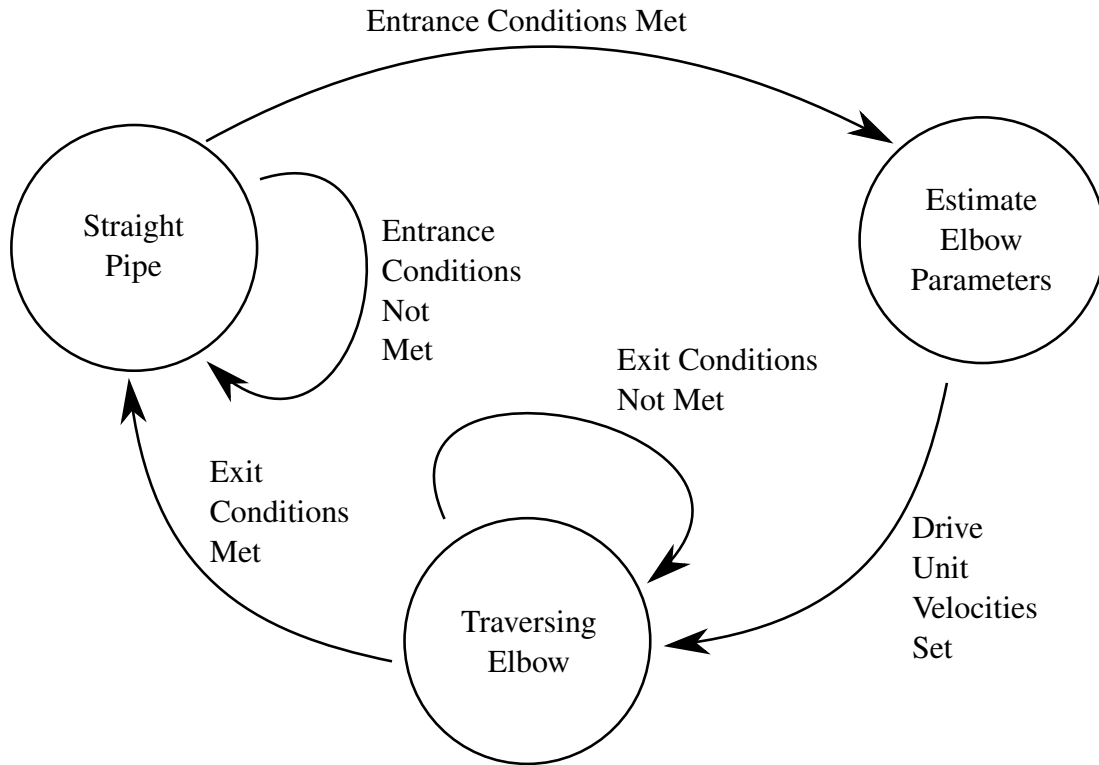


Figure 3.1: Autonomous elbow controller overview

3.2 Local and Global Axes

This section defines some of the global parameters that are used throughout the chapter.

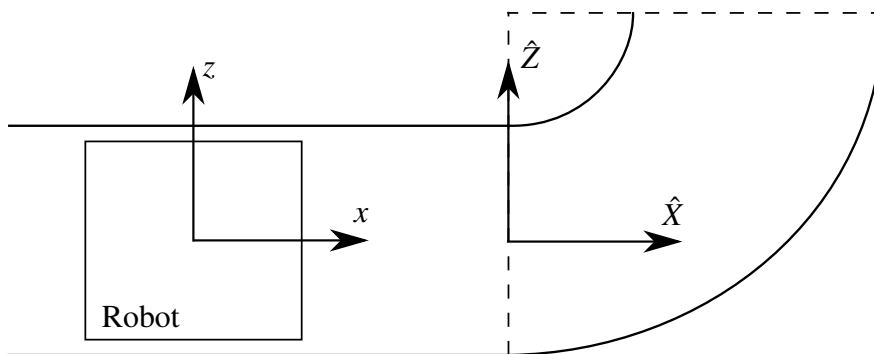


Figure 3.2: Global and local axes

The axes shown in Figure 3.2 are the local and global coordinate frames for the robot and corner. The local coordinate frame, x , y and z are referenced to the centre of the inspection robot itself. In this case the x axis points in the direction the robot is travelling and the z axis points in the direction of the first Drive Unit (DU) on the

robot, usually coloured red. The global coordinate frame is defined as \hat{X} , \hat{Y} and \hat{Z} , and is referenced to the elbow. \hat{Z} intersects the shortest radius of the elbow, i.e the direction of the curve, and \hat{X} points into the back of the corner. The global axes are fixed as the elbows do not move, whereas the robot axes change with the robot so that despite what is shown in Figure 3.2 the \hat{Z} and z axes are unlikely to be aligned, unless manually set at the start.

3.3 In-Pipe Sensing Requirements

To determine the requirements of the sensing system the elbow parameters (Section 2.4.1) are reviewed. The four major parameters of an elbow are: corner direction (θ_d), minor radius (r), major radius (R) and corner angle (ϕ_a). As r is the pipe radius it can be found using feedback from the wall-pressing system of the robot. A feedback mechanism can be used to determine the diameter of the robot and thus the pipe radius. Alternately, this could be measured by the sensing system on the robot or as the robot is placed in the pipe.

For a first approximation, R is assumed to be fixed for that of a standard short elbow [10] where it is equal to the diameter of the pipe. However, a method of detecting this would be advantageous. As a result, ϕ_a and θ_d are the only unknowns. Assuming the robot is approaching the elbow, unless ϕ_a was sufficiently shallow that the end of the corner could be seen, it cannot be determined at the start of the elbow.

The controller proposed in Section 3.1 checks for exit conditions to leave the elbow. This allows ϕ_a to be unknown as it enters the pipe. Leaving θ_d , corner direction, as the final required parameter to be detected.

To be competitive with the systems in the literature (Section 2.4), a target accuracy for the estimation system is selected: an absolute mean error of $\theta_{d_{target}} = 10^\circ$ for corner direction. Despite being untested by other methods, a 5% error for the major radius is selected.

The estimation system must be able to identify the corner direction (θ_d) and major radius (R) ahead of the robot. To allow the control action to be determined before the robot enters the elbow. The feeler sensors are also required to have a mechanism to press them against the walls of the pipe, the force required to be exerted on the wall needs to be sufficient to hold in the arm against the pipe wall but not so high it damages the pipe or the sensor.

The contribution of this chapter is the presentation of a novel sensor and algorithm designed for the task of estimating the corner direction to allow autonomous navigation in an unknown pipe network. The focus of the estimation is corner direction. However, a method for predicting the elbow major radius (R) is also proposed.

3.4 Feeler Sensor

The proposed designs will consist of an arm that follows the pipe wall with a method of feeding back the angle. As the corner can change in any direction, a set of three feelers which are equally separated around the pipe are required. Their separation is defined by δ_i . The feelers are mounted ahead of the robot to allow the estimation to be made before the robot enters the elbow.

The measured angle from the sensor is defined as α_f . It is recorded as it travels along the pipe ahead of the robot. Figure 3.3 shows a simplified diagram of the design. The mounting height (m_d) and feeler length (l_f) are also shown.

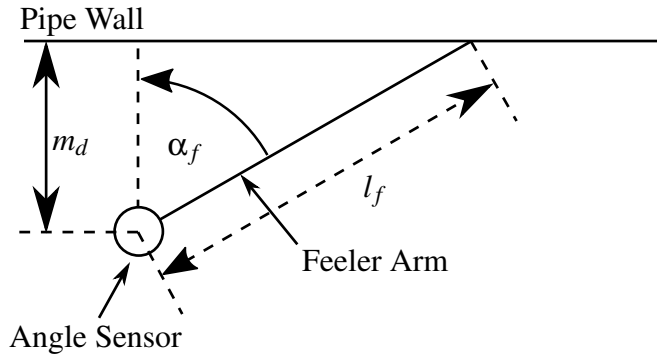


Figure 3.3: Simplified diagram of feeler

In addition to the feeler an on-board encoder is required, the use of which will be discussed later. To simplify visualising the feeler data, the three sensors are referred to by colour, Red, Green and Blue.

3.5 Corner Parameter Estimation

This section presents the proposed method for predicting the corner direction, θ_d , which is the primary contribution of this chapter. It also presents an extension to the method to determine the corner radius, R , for the case that the robot is not travelling in a standard short elbow.

As discussed, the feelers are mounted ahead of the robot. As such, the feelers enter the corner before the robot. During that time, the mounting point of the feeler is in the straight pipe and the feeler arms are passing through the corner. The corner parameters for the control system need to be calculated before the robot enters the corner. This gives a region in the elbow in which the estimation needs to be made. This region is called the corner entrance, which is shown in Figure 3.4.

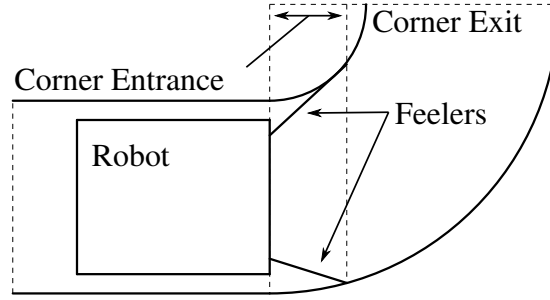


Figure 3.4: Corner entrance

The length of the corner entrance (d_x) is based on the feeler length (l_f): the longer the feeler the greater the entrance size. As α_f changes when the robot is in the corner, d_x is calculated with the straight pipe value ($\alpha_{f_{\text{NOM}}}$) to ensure the estimation is always made before the robot enters the elbow, $d_x = l_f \sin \alpha_{f_{\text{NOM}}}$.

As the feelers pass into the corner, through the entrance, all three are sampled. The combination of the three samples is S . These samples are taken multiple times $\{S_1, S_2, \dots, S_n\}$ as the feelers progress into the corner, see Figure 3.5. The number of samples taken vary depending on the sample rate (s_r) and robot velocity (V_r), i.e. $S_{\text{max}} = \frac{d_x s_r}{V_r}$.

The algorithm requires a minimum of two samples to be taken in the corner. The final sample (S_n) is the sample at the end of the entrance, and the first (S_1) is the start.

3.5.1 Corner Direction Estimation

The direction, θ_d , to be estimated is the angle between the robot and the corner's z axis. This direction is crucial to determine the control action for the robot.

The process of predicting the direction has been split into three stages: Stage I: Sample Processing, Stage II: Sample Combination, and Stage III: Final Estimation, as shown in Figure 3.6.

The full process is summarised in a flow chart shown Appendix Figure 9.1.

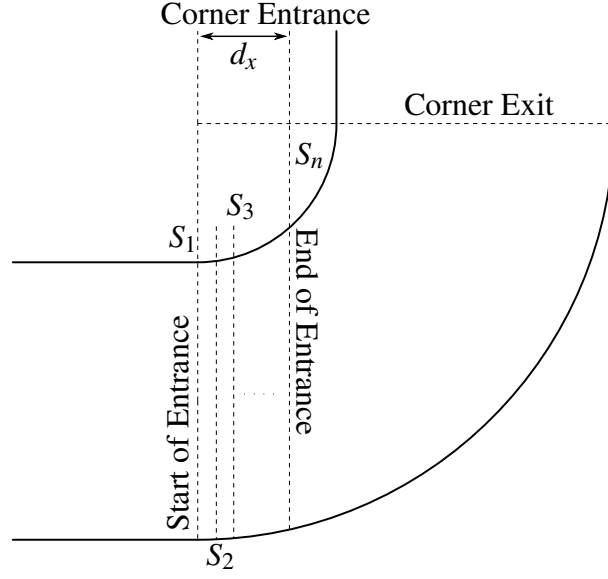
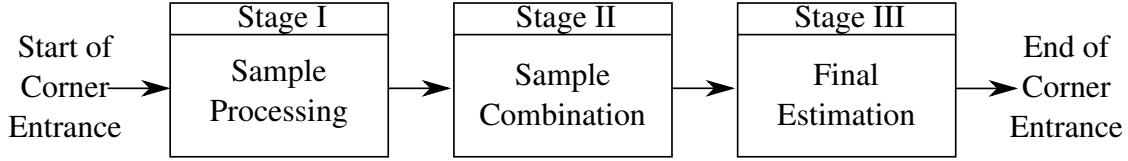
Figure 3.5: Corner entrance for short elbow with samples S labelled

Figure 3.6: Corner direction stages

Stage I: Sample Processing

In the first stage data is collected from all the feelers. The data is taken over multiple samples $\{S_1, S_2, \dots, S_n\}$ as the feelers travel through the corner entrance, Figure 3.5. Note the sample distance in Figure 3.5 is not to scale as it will vary depending on robot velocity and sample speed. The method of dealing with a single sample will be explained in more detail in the following. The method is the same for all the samples taken in the corner.

The three feeler sensors are sampled and the angle determined; $\{\alpha_{f_R}, \alpha_{f_G}, \alpha_{f_B}\}$ are the feeler angles for the Red, Green and Blue sensors at a single sample point (S_i). These three angles can be entered into the kinematic model to give the end coordinates of the three feelers; $\{P_R, P_G, P_B\}$ are the contact points of each feeler with the elbow wall. Each end point has its own set of coordinates in the robot's local coordinate frame, $P_R = (x_R, y_R, z_R)$, $P_G = (x_G, y_G, z_G)$ and $P_B = (x_B, y_B, z_B)$.

A simplified diagram of the kinematic model is shown in Figure 3.7. l_l is defined by the mounting height (m_d) of the feelers and the radius of the pipe $l_l = r - m_d$.

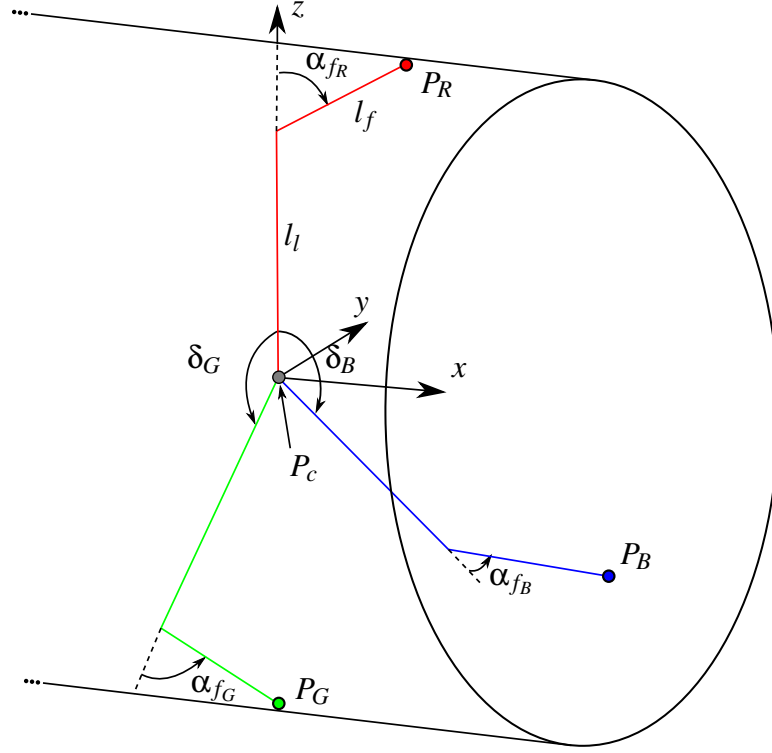


Figure 3.7: Kinematic model of feelers

The kinematic model can be determined as follows,

$$x_i = l_f \sin \alpha_{fi}, \quad (3.1a)$$

$$y_i = (l_l + l_f \cos \alpha_{fi}) \sin \delta_i, \quad (3.1b)$$

$$z_i = (l_l + l_f \cos \alpha_{fi}) \cos \delta_i; \quad (3.1c)$$

where $i = R, G$ or B depending on if the feeler angle has been entered from the Red, Green or Blue feeler and δ_i is the angular separation of each feeler sensor from the robot's local z axis.

Once the end of the three feelers has been found they can be combined to give their middle point, P_{fm} . The central point can be found by finding the mean of the end points as shown in the following equations,

$$\bar{y} = \frac{y_R + y_G + y_B}{3}, \quad (3.2a)$$

$$\bar{z} = \frac{z_R + z_G + z_B}{3}, \quad (3.2b)$$

$$P_{fm} = (\bar{y}, \bar{z}). \quad (3.2c)$$

Figure 3.8 shows the local (y, z) and global (\bar{y}, \bar{z}) axis of the robot with the feeler end locations (P_i), feeler centre point (P_{fm}) and robot centre (P_c) labelled. For comparison both the offset when in a straight pipe and when in an elbow are shown. When in the straight pipe, the robot centre (P_c) and the feeler centre (P_{fm}) are at the same point and as the feeler angles change in the corner they become separated.

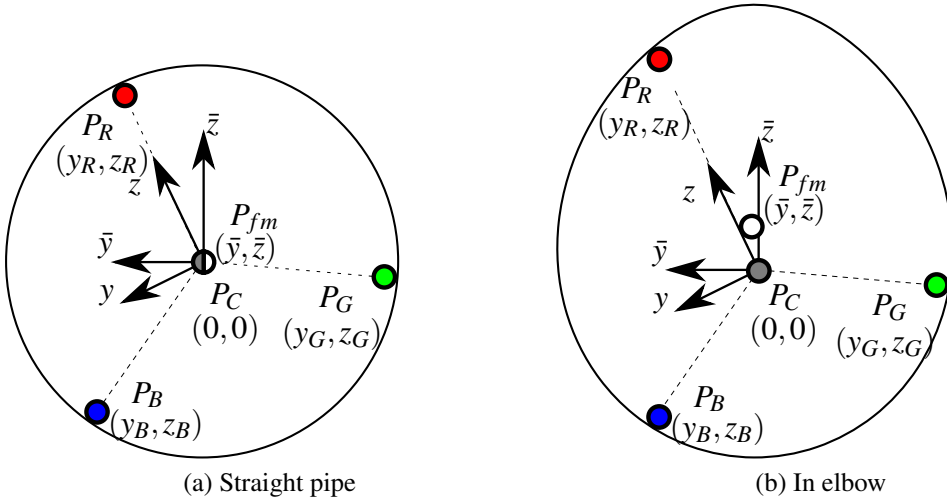


Figure 3.8: Feeler end points layout in (y, z) plane

The next step is to find the change between the feeler central point, P_{fm} , and the robot centre, P_c . This will give the overall change in y and z for that sample. The changes d_y and d_z are given by,

$$d_y = P_{fmy} - P_{cy}, \quad (3.3a)$$

$$d_z = P_{fmz} - P_{cz}. \quad (3.3b)$$

This process is repeated for each new sample of the feelers to give a change in y and z for each sample. As the feelers travel further into the corner entrance, it is expected that d_y and d_z will increase as P_{fm} moves further away from P_c and more towards the direction of the corner. This is because the deeper they go the more the pipe itself changes thus giving a greater angle change to the feelers. Figure 3.5 shows the change in the pipe as the samples progress into the corner entrance. It should also be noted that as each sample sees a single slice of the corner, the shape tends from a circle in the first sample, S_1 , to an ellipsoid like shape in S_n (shown in Figure 3.8(b)).

Stage II: Sample Combination

The second stage of the corner direction estimation is the combination of the previous samples (shown in Figure 3.9) to give a single angle output.

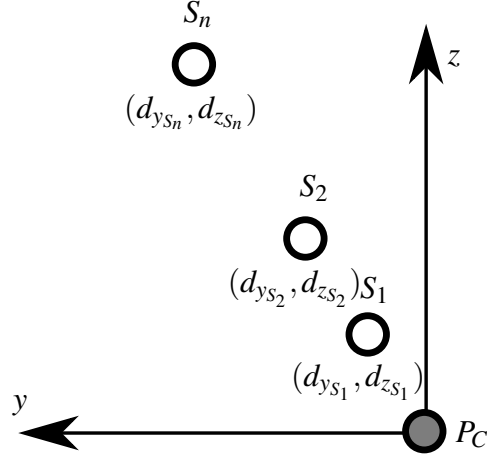


Figure 3.9: Sample changes in (y, z) plane

Their change, d_y and d_z is summed giving a total displacement in y and z over all the samples for the direction. For the real system, combining them in this method would allow for the rejection of small errors in the changes, as the overall change would be in the corner direction. The sum of the changes are denoted by D_y and D_z and given by:

$$D_y = \sum d_{y_{S_1}} + d_{y_{S_2}} \dots + d_{y_{S_n}}, \quad (3.4a)$$

$$D_z = \sum d_{z_{S_1}} + d_{z_{S_2}} \dots + d_{z_{S_n}}. \quad (3.4b)$$

Once the total changes in y and z has been found, they can be used to find the direction (θ_{fm}). Figure 3.10 shows the summed samples and identifies θ_{fm} . As a result, the angle θ_{fm} is given by:

$$\theta_{fm} = \arctan2(D_y, D_z), \quad (3.5)$$

where $\arctan2$ is the four-quadrant inverse tangent.

To simplify the computation for the combination of the samples, it is assumed that averaging the feeler ends to give the total displacement will represent the corner direction. However, the feelers actually follow an ellipsoid shape as they enter the corner (Figure 3.8). A second assumption is that the feeler angles which are taken at a single sample are in the same vertical plane (as shown in Figure 3.5). These assumptions introduce a small error in θ_{fm} . This error is shown in Figure 3.11 in the

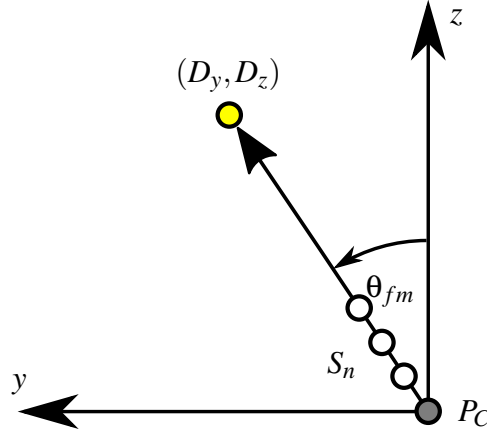


Figure 3.10: Combination of sample changes in (y, z) plane

difference between θ_d and θ_{fm} . Figure 3.11 shows the final sample S_n for a simulated corner. The feeler layouts, feeler central point (P_{fm}) and robot centre (P_C) are shown.

To more accurately identify the corner direction from the feeler data an elbow would need to be fitted to the three sets of feeler end coordinates, then the accurate direction could be inferred from that. This would be very complex and computationally heavy. This is why an average was used.

Stage III: Final Estimation

The final stages compensates for the small discrepancy introduced earlier by analysing the correlation of θ_{fm} and θ_d .

Figure 3.12 shows the comparison of the ideal estimation of the corner direction (θ_d) and the angle generated from θ_{fm} . It can be seen that there is a clear correlation between the estimated (θ_{fm}) and actual (θ_d) direction. This correlation is independent to each estimate and can be corrected for. Due to the error being introduced by the estimation method, it is true for all elbows with the following features: constant major and minor radius, and continual direction (meeting the standard elbow classification in Section 1.1).

To be able to correct for the difference, curve fitting is used to best approximate the function. This is done using a sine function and the best fit is shown in Figure 3.12. The following approximation (θ_{dest}) of θ_d is found,

$$\theta_{dest} = \theta_{fm} + 13 \sin(3.0184\theta_{fm}). \quad (3.6)$$

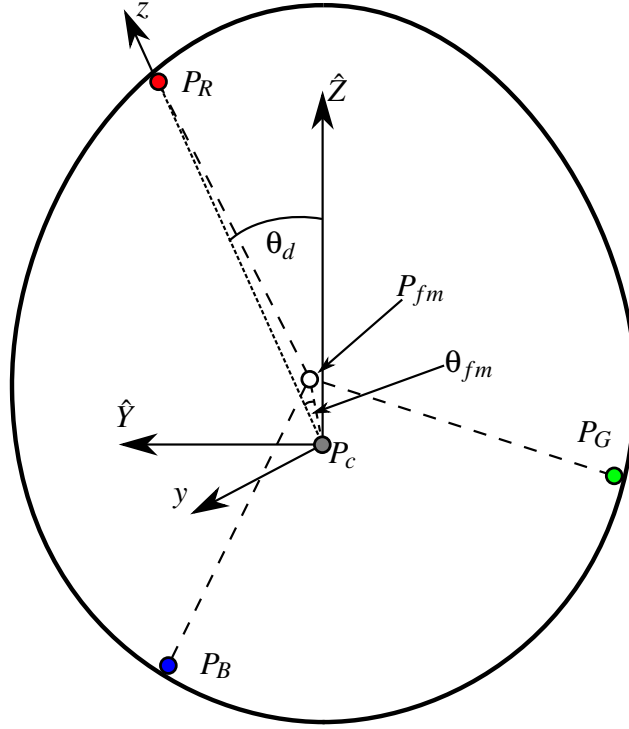


Figure 3.11: Diagram of leg layout and robot and feeler centre points

It can be seen from (3.6) that the variable affecting the phase of the sine function is very close to three. This is related to the three feeler units in the pipe. The response from the feelers will repeat every 120° and the factor will be treated as 3 from this point. This extra term is the compensation term (ζ), where $\zeta = 13 \sin(3\theta_{fm})$.

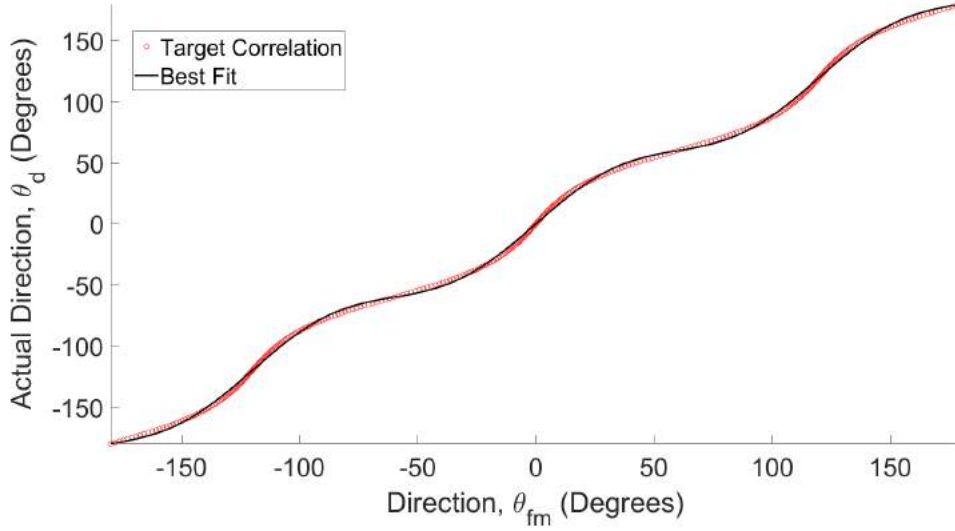
As a result, the compensated angle for the corner direction is given by,

$$\theta_{dest} = \theta_{fm} + \zeta. \quad (3.7)$$

This method offers a light-weight estimation with a maximum systematic error (ϵ_{\max}) of less than 2° .

3.5.2 Corner Radius

A method of extending the corner direction to also determine the major radius, R , is proposed. The process of predicting R utilises the Intersecting Chords Theorem (ICT). This theory, with some manipulation, allows the radius of a circle to be determined from a chord across it. Following [71], the radius R of a circle with a chord of width

Figure 3.12: Empirical approximation for calibrating θ_{fm}

(W) and height (H) is defined by:

$$R = \frac{H}{2} + \frac{W^2}{8H}. \quad (3.8)$$

As the feelers take multiple samples through the corner entrance, Figure 3.5, the change in the x axis (from an on board encoder) is also recorded, d_x . To apply this to the ICT, d_x is used as half the chord width W . To give a height from the chord, the final sample taken in the corner entrance can be used, $S_n = (d_{y_{S_n}}, d_{z_{S_n}})$ to give a magnitude, d_{yz} , to that point from the robot centre, P_C , i.e.

$$d_{yz} = \sqrt{d_{y_{S_n}}^2 + d_{z_{S_n}}^2}. \quad (3.9)$$

As the change has already been calculated for the corner direction this requires no more sensing of the feelers. For this application, d_{yz} is used as H . Substituting the values and rearranging (3.9) gives the following equation to calculate the radius,

$$R_{est} = \frac{d_x^2 + d_{yz}^2}{2d_{yz}}. \quad (3.10)$$

Figure 3.13 shows the method of applying the feeler data to the ICT.

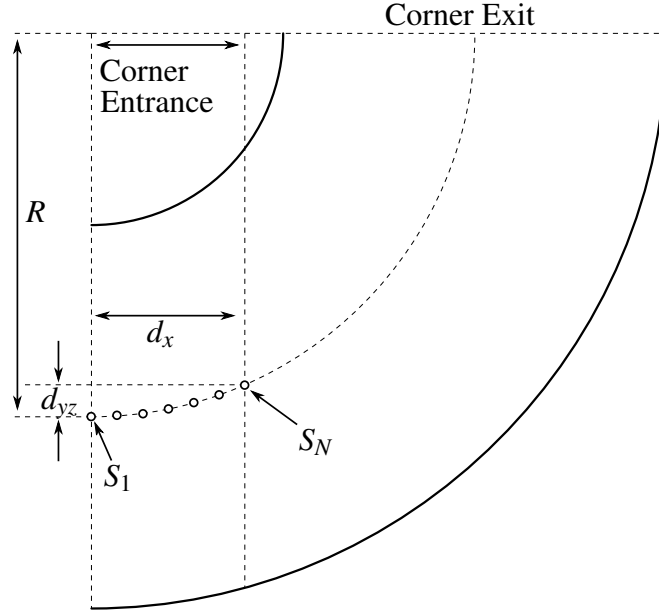


Figure 3.13: Using Intersecting Chords Theorem (ICT) to determine corner radius

3.5.3 Algorithm Triggering

When no noise is present the algorithm can simply be triggered when any change is detected, but when using real sensors that have noise, a threshold value (T_{start}) is set. This value is selected based on the noise characteristics of the sensors. As a guideline value, a threshold of 20 % of the minimum final expected change can be selected, $T_{\text{start}} = 0.2d_{yzs_n}$. Where d_{yz} is the magnitude of change of P_{fm} calculated by $d_{yz} = \sqrt{d_y^2 + d_z^2}$ and S_n is the final sample. The minimum change is selected as, d_{yz} varies based on the corner direction and thus the worst case is considered.

In the real application the previous feeler values can be placed in a buffer so they can be referred back to for finding the first sample (S_1). The number of samples stored in the buffer (B_n) will be depended on the sample frequency (F_s), robot velocity (V_R) and corner entrance distance (d_x), $B_n \geq \frac{0.2d_x}{V_r/F_s}$.

Storing the information allows the algorithm to be triggered further into the corner entrance when the change in the feeler angles is large. Then the samples previously gathered can be recalled to allow the estimation of the corner parameters. Using this method allows greater noise rejection.

3.6 Summary and Contribution

The chapter proposes a method of detecting and estimating the parameters of an unknown elbow. The method presented utilises a feeler sensor that is developed for the task of detecting the change ahead of a robot within a pipe. A set of three sensors are used and the data from them manipulated to give an estimation of the corner direction with an error of less than 2°. A method of extending the algorithm to predict corner radius is also proposed. The proposed algorithm provides a computationally light method of determining the corner parameters, and the solution is scalable to small or large pipe diameters.

Chapter 4

Corner Parameter Estimation Experiment

This chapter provides the method and results for testing the corner parameter estimation algorithm and sensors presented in Chapter 3. The motivation for the experiment is the validation of the proposed method of direction and radius estimation. This can then be used to calculate the velocity for each Drive Unit (DU) to form the ‘Estimate Elbow Parameters’ state of the proposed elbow controller, shown in Figure 3.1.

The Contribution of this chapter is the validation of the feeler sensors and algorithm of the estimation of direction and radius in an unknown elbow.

The chapter first describes the hardware used in the experiment, then presents the results and discusses them. The requirements of the detection system are laid out in Section 3.3. They are summarised in the following:

- Corner direction estimation target accuracy of $\theta_{d_{target}} = 10^\circ$.
- Major radius estimation target accuracy of 5%.
- Detection method that can complete its estimation before the main body of the robot enters the elbow. The exact distance is dependent on the length of the feeler arm.

4.1 Experimental Hardware and Methodology

To practically test the algorithm developed for the estimation of unknown corner parameters, an experiment was derived to measure the feeler data as it passed through an

elbow with various directions (θ_d) over multiple samples. To achieve this, the feeler sensor and a linear translation test rig were designed and constructed. The experiment was created for a 150 mm diameter pipe and elbow with $R = 152.4$ mm.

4.1.1 Feeler Sensor

The feeler sensors are designed around the basic diagram shown in Figure 3.3. A Potentiometer (POT) was used as the method of determining angle (similar to Russell [66]) as they are low-cost and very computationally light to sample. For the contact point of the feeler a passive roller ball was used to remove any effect of the lateral forces damaging the feelers. A spring was used to pull the feeler on to the wall such that it has a constant contact. For the use in T-junctions an active way to retract the feelers could be considered but this will be reviewed in further work. A labelled simplified diagram of the feeler is shown in Figure 4.1.

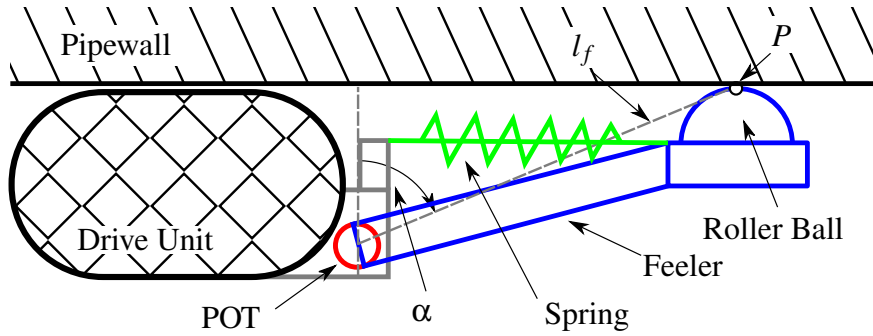


Figure 4.1: Simplified diagram of feeler

Due to the low tolerances of the POTs, there were errors between the outputs of the three feelers for the same angle of the POTs. To overcome this issue, the feelers have been individually characterised and a look up table of voltage output from the potential divider and input angle was used for each feeler to give a more accurate angle output.

The finalised feeler sensors for the corner direction estimation experiment is shown in Figure 4.2.

The length of the feelers (l_f) was calculated by modelling the detection angle range for differing lengths as shown in Figure 4.3. The model simulates a feeler passing into the entrance of a 150 mm elbow (on the shortest path) and determines the angle (α_f) as it progresses through. It does this for varying lengths of feeler. This allows the full range of angles for each feeler length to be found and thus the one with the greatest range of angles can be selected.



Figure 4.2: Feeler sensor for corner direction estimation experiment

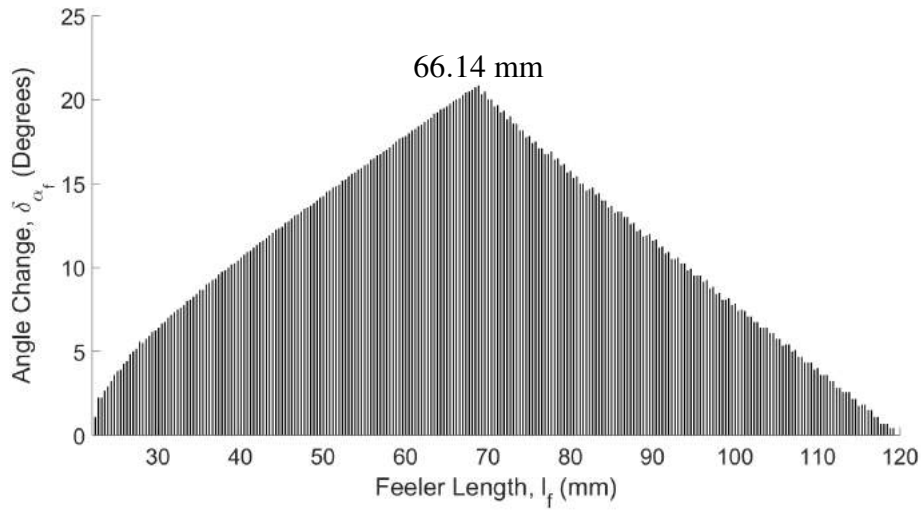


Figure 4.3: Plot of change in angle vs feeler length

It is desirable to maximise the change in feeler angle (δ_{α_f}) as it gives a wider detectable range. The feeler arm length that gives the maximum change of $\delta_{\alpha_f} = 20.83^\circ$ is estimated to be $l_f = 66.14$ mm, for a short elbow ($R = 150$ mm, $r = 75$ mm) with a mounting height of 22 mm. It can be seen from Figure 4.3 that the feeler length peaks at this value and then quickly reduces as l_f increases. The manufactured length was rounded to the nearest millimetre giving a feeler length of $l_f = 66$ mm. A triggering threshold of 1 mm was selected for this combination of feeler length and elbow size, based on practical experimentation. The effects of manufacturing tolerances will be reviewed later in the chapter. Despite the feeler being designed for the 150 mm pipe it will still be effective in a different pipe size, however if the nominal size of the pipe is known a new l_f can be found for that pipe diameter and the feeler manufactured to that length.

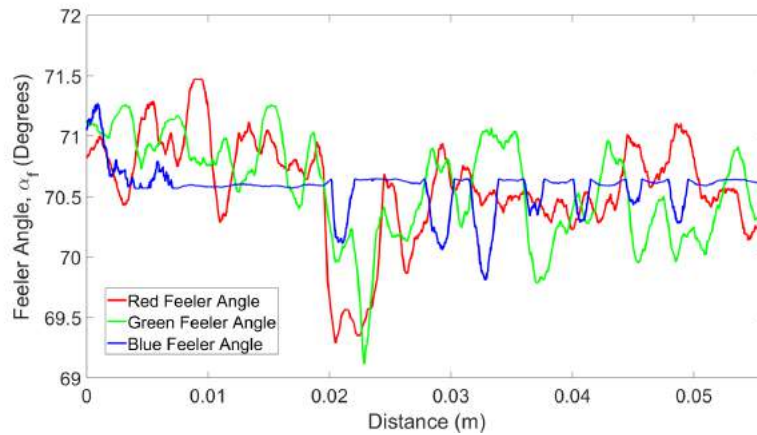


Figure 4.4: Feeler data for a straight section of pipe

To characterise the feeler sensors, they were moved through a straight section of pipe and their resistance recorded (through a potential divider). The recorded data was converted to feeler angle and the results are shown in Figure 4.4. It can be seen in the figure that there is noise present in the recorded data. This is likely due to the low-cost POTs and the minor imperfections on the inside face of the real pipe.

4.1.2 Linear Translation Test Rig

The experiment was designed to give feeler data for an accurate estimation of the corner parameters. The test pipe consisted of a 150 mm diameter section of straight pipe with a coupler to a 90° elbow with $R = 152.4$ mm.

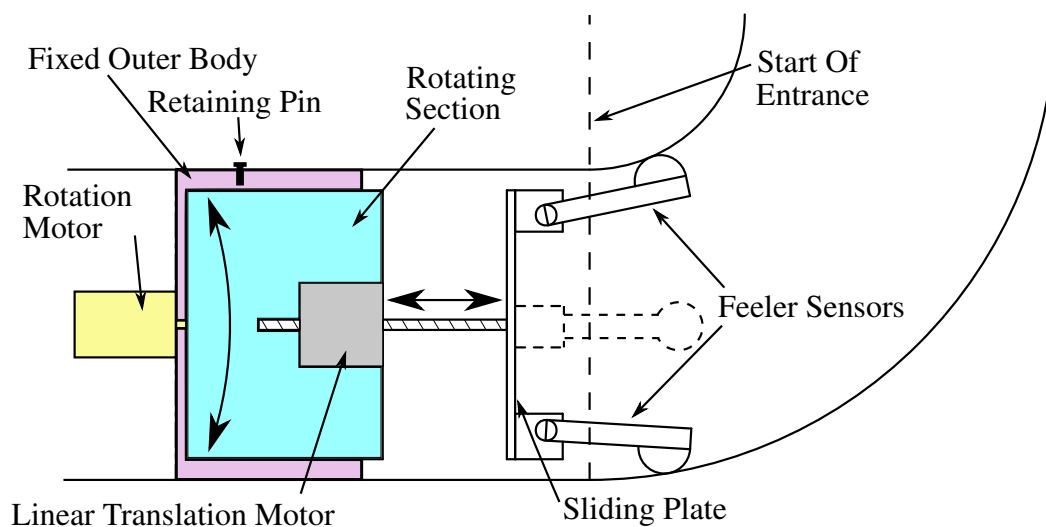


Figure 4.5: Simplified diagram of test rig

The test rig was designed and constructed in house to fit within the pipe and is locked in place with a retaining pin. This held the rig with the feelers in line with the entrance to the pipe. A linear translation stepper motor drove a plate with the feelers attached to it into the corner in 0.01 mm increments with an accuracy of $\pm 5\%$ [72]. The step distance of the test rig will be smaller than the actual robot, however this was used to characterise the feelers and the method will still be applicable to the deployable robot. The translating plate was mounted inside a large bearing which can rotate the whole assembly within the pipe. The rotation controlled the direction of the corner in relation to the robot, θ_d . A motor drove this rotation with an accuracy of 0.54° [73]. A simplified diagram of the experiment is shown in Figure 4.5 and a photo of the real rig is shown in Figure 4.6.

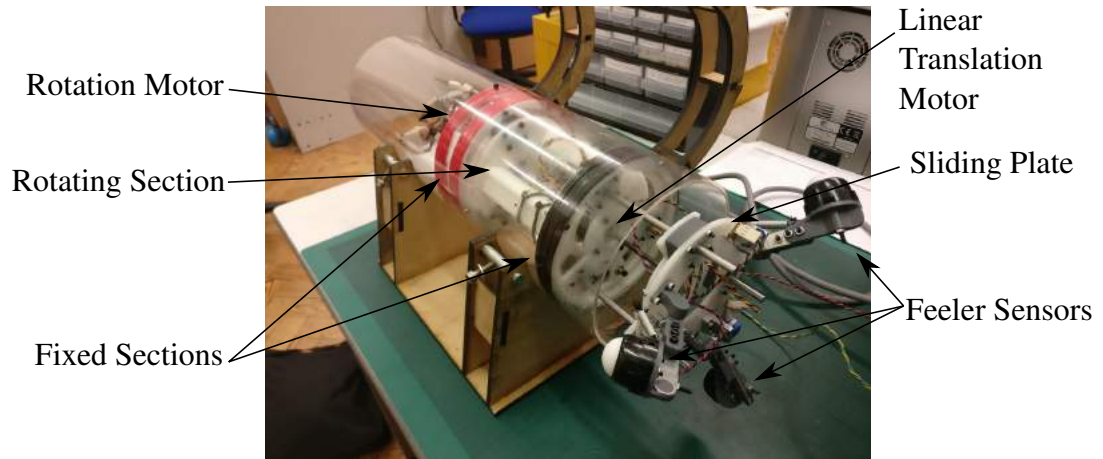


Figure 4.6: Simplified diagram of test rig

The specification of the linear test rig is summarised in Table 4.1.

Table 4.1: Linear translation test rig specification

Rotational Step Size	10°
Rotational Accuracy	0.54°
Rotational Range	$\pm 180^\circ$
Linear Translation Step Size	0.01 mm
Linear Translation Accuracy	$\pm 5\%$
Linear Translation Range	0 - 0.065 m

4.1.3 Experimental Procedure

The rotation motor held the rotating section at the specified angle (θ_d). For each θ_d the feeler sensors were stepped into the corner using the linear translation stepper motor. On each step, the feeler angles (α_{fi}) were sampled and logged. This process is called a pass and is repeated a minimum of five times.

Once complete, θ_d was then incremented and the passes repeated. θ_d was varied in increments of 10° between $\pm 180^\circ$ to give full 360° coverage of the elbow.

The raw data was then run through the corner estimation algorithm. This was compared with the actual corner direction and radius to evaluate the performance of both the feeler sensors as well as the algorithm.

4.2 Results and Discussion

This section reviews the results taken from the feeler rig then follows with a discussion. The experimental method used to gain the data is explained in Section 4.1.3.

4.2.1 Results

As such a large volume of data was gathered from the experiment, first a single data set which is representative of the whole set will be analysed in detail, then the averaged data for each direction will be presented for the full analysis.

Single Pass: The selected set of data for detailed investigation was taken from the $\theta_d = -70^\circ$ set, as the results for this direction are the closest to the mean error and can be viewed as representative of the full data set.

First the raw feeler data was compared to the simulated expected change to prove the feasibility of using the feeler sensor as a detection method.

Figure 4.7 shows the simulated progression of the end points of the three feelers at $\theta_d = -70^\circ$. Where $P_{i_{s_1}}$ is the end point of the Red, Green or Blue feelers at the start of the Corner Entrance and $P_{i_{s_n}}$ is the end point at the end of the Corner Entrance.

It can be seen that for the Blue feeler, the end point (P_B) moves closer to the centre of the robot (P_c) increasing the feeler angle by a large magnitude. For the Red feeler (P_R), the movement is away from the centre (P_c) decreasing the feeler angle but with a small magnitude. The Green feeler end point (P_G) also moves away from P_c decreasing the feeler angle, but with a larger magnitude than the Red feeler. It should be noted that

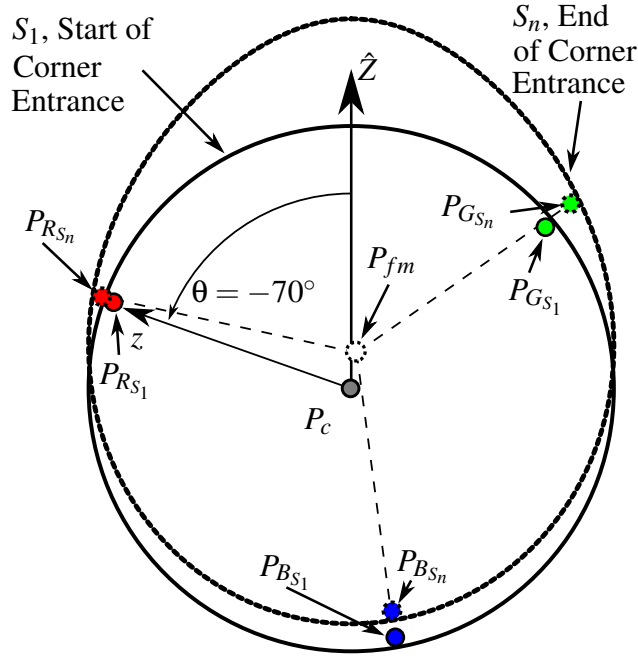


Figure 4.7: Leg layout of feelers at start (S_1) and end of corner (S_n) entrance for $\theta_d = -70^\circ$

as the selected $\theta_d = -70^\circ$ contains 10 passes into the corner. This expected change is applicable for any elbow satisfying the assumptions of the estimation system (defined in Section 3.5.1), with a corner direction of $\theta_d = -70^\circ$ as the feeler sensors will pass along the same paths in the elbow.

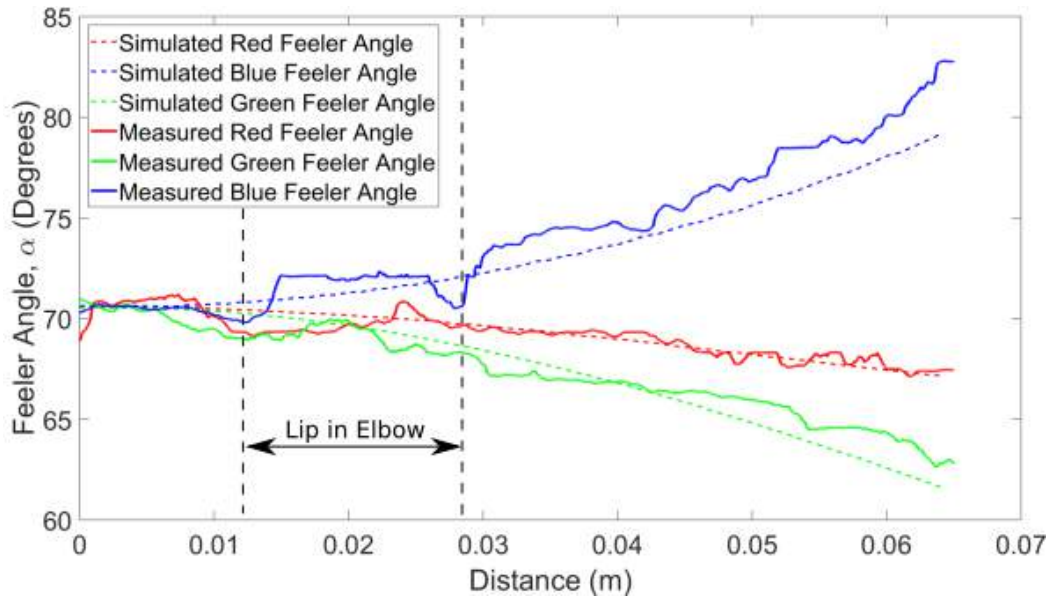


Figure 4.8: A single pass (Pass 5) of raw feeler angle data at $\theta_d = -70^\circ$

Figure 4.8 shows the raw data from one of the passes (pass 5) with the simulated angles added for comparison. It is very noisy, however there is a trend in direction for each feeler angle as the distance into the corner increases. The Blue feeler has a large positive change in angle (α_{f_B}), the Red feeler has a slight decrease in the angle (α_{f_R}) and the Green feeler has a decrease in angle (α_{f_G}), which is larger than the Red feeler.

The general trends that were expected for from this data match the expected changes shown in Figure 4.7 and the simulated data in the figure. This proves using the feeler sensors to detect the change in the corner is feasible. Figure 4.8 also highlights the region where the feeler sensors passed over a lip on the coupling of the elbow to the straight pipe, this is very apparent from the Blue feeler data where the bump can clearly be seen. This lip adds an additional error to the measurement, but it is acceptable as the general trend of the data is correct.

Now the sensing method has been accepted, the estimation from that data can be reviewed. Note despite the focus of the proposed estimation method being corner direction, the extension to the radius was also run and its results analysed. Passing the full set of data (all 10 passes) at $\theta_d = -70^\circ$ through the presented algorithm from Section 3.5.1, the final estimation of corner direction ($\theta_{d_{est}}$) and radius (R_{est}) can be found, as shown in Table 4.2. The highlighted row is the estimation from the feeler angles presented in Figure 4.8.

Table 4.2: Predicted angles of the multiple passes for $\theta_d = -70^\circ$

Pass	Predicted Direction ($\theta_{d_{est}}$)	Predicted Radius (R_{est})
	Degrees	m
1	-66.05	0.1524
2	-65.16	0.1522
3	-62.97	0.1521
4	-65.12	0.1523
5	-65.09	0.1522
6	-63.49	0.1522
7	-66.61	0.1523
8	-63.52	0.1521
9	-67.88	0.1523
10	-64.74	0.1522
Average	-65.06	0.1522

The average estimation across the multiple passes was -65.06° with a range of 4.91° ; this gave a mean estimation error of 4.94° . The radius target was 0.1524 m, the average estimation was 0.1522 m giving and average mean error of 0.2 mm.

Full Data Set: For each value of θ_d in increments of 10° between -180° to 180° , there are a set of multiple passes of feeler data. For each pass the feeler angles have been passed through the corner direction estimation algorithm and the estimation logged. To display this data, the mean estimation of each corner direction $\theta_{d_{est}}$ for each of the entry angles θ_d has been plotted in Figure 4.9 with error bars for the minimum and maximum estimation for each set.

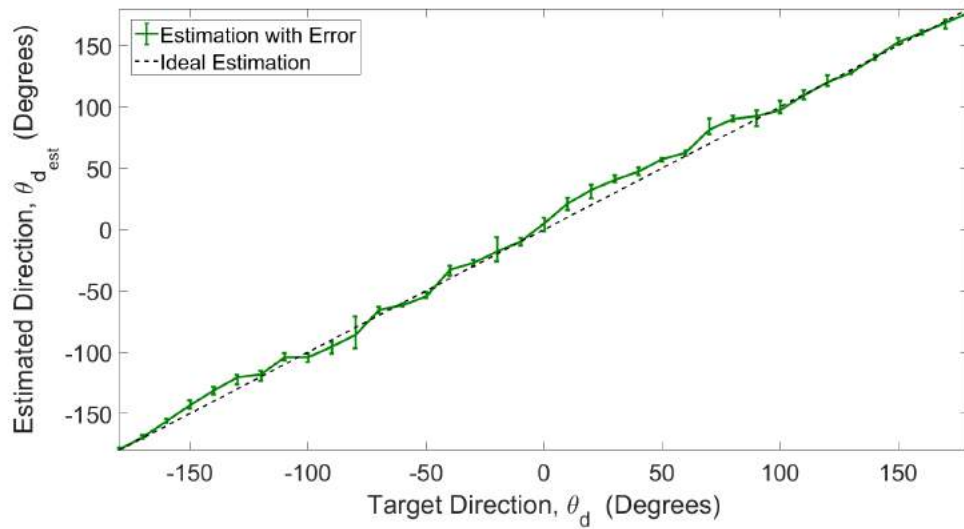


Figure 4.9: Mean estimated angles Vs target angle

It can be seen that the predicted direction follows the ideal estimation with a small amount of error. The largest error for the estimation was at $\theta_d = 70^\circ$ with an error of 20.53° . Reviewing the averaged estimations for each angle, the mean absolute error in the direction was $\bar{\epsilon}_{\theta_d} = 4.69^\circ$. This metric is used to allow it to be compared with MRINSPECT VI [27] and Kim et al. [60] which are being used as the benchmark for this system. For the radius estimation there was a mean absolute error of $\bar{\epsilon}_R = 0.91$ mm over all the samples.

4.2.2 Discussion

The changes in the raw feeler data from Figure 4.8, followed the expected change for the feeler angles. This shows the basic principle of the method is valid and the change in direction can be detected using the feeler sensors.

From the full set of data shown in Figure 4.9, the trend of the estimations followed

the target angles but there were errors present. The mean absolute error in the direction estimation was $\bar{\epsilon}_{\theta_d} = 4.69^\circ$ and the worst case was $\epsilon_{\max} = 20.53^\circ$. However the algorithm provides a good estimation of direction, which was required for the elbow controller. Further analysis on the error from the estimation will be completed in Chapter 6.

Reviewing the requirements of the sensing system (Section 3.3), the corner direction estimation ($\bar{\epsilon}_{\theta_d} = 4.69^\circ$) was an improvement over the target accuracy of $\theta_{d_{\text{target}}} = 10^\circ$. It also achieved the target accuracy of radius estimation (5%) with an error of 0.61%, but this was only tested on a single radius elbow. Finally, the estimation system was able to determine the parameters before the robot entered the elbow, fulfilling the requirements of the system.

Comparing this to the simulated results the expected error was $\epsilon_{\max} = 1.78^\circ$ which was lower than the measured result. This shows the method is viable for predicting corner direction but could be improved. The error in the measurements was due to the low-cost POTs used for measuring the angle. These provided noisy data and require lengthy individual characterisation as the tolerances in the components cause their resistance to vary across the three feelers. Even with the characterisation there was still a large amount of noise in the data from the sensors.

As the three feelers were at a fixed offset to each other of 120° , if the sensors were ideal and had clean responses, the output of feelers and thus error in the estimation would repeat every 120° . It can be seen in Figure 4.9 that the areas where there are large errors, such as $\theta_d = 80^\circ$, the error was not repeated at $\pm 120^\circ$ from it (-40°). This shows the errors are not due to estimation method but due to poor readings from the sensors themselves. Improvements could be made by replacing the low-cost sensors with higher end encoders to reduce the noise from the sensors and improve the accuracy of the estimation system.

4.2.3 Effect of Manufacturing Tolerances on Prediction

The effects of manufacturing tolerances on the length of the feeler was reviewed to see the effect this would have on the final output of the system. The target length for manufacturing was taken as 66.14 mm with the feeler's ideal length of 66.14 mm. Reviewing the worst case errors in manufacturing the maximum and minimum possible feeler lengths were found to be $l_{f_{\max}} = 66.52$ mm and $l_{f_{\min}} = 65.68$ mm. Propagating these values through the system and reviewing the worst case application of two feelers at length $l_{f_{\max}}$ and one feeler at length $l_{f_{\min}}$ led to an absolute mean error in the output

of 4.19° . This includes the maximum simulated error in the method of $\epsilon_{\max} = 1.775^\circ$. Due to this variation and the probability of this case occurring being small, the effect of the manufacturing tolerances in predicting corner direction will be negligible.

4.2.4 Comparison Other Detection Systems

The MRINSPECT VI [27] and Kim et al. [60] are being used as the benchmark for this estimation, they have a mean error ($\bar{\epsilon}_{\theta_d}$) of 2.84° and 0.64° respectively. Comparing this to the results, the mean error of the real system was $\bar{\epsilon}_{\theta_d} = 4.69^\circ$ which shows that both the sensor suits have a more accurate corner detection. However, the aim of this task was to make a comparable estimation method which is scalable for use within a 50 mm pipe, and which is computationally and financially cheap and has a low system load. The cost of the sensors for systems are compared in Table 4.3. All the prices are only for the sensors, additional items such as the processor required to run the algorithms and mounting materials are not included. However, it can be seen that there is a clear advantage in using the feeler based system in terms of cost meeting its aim. It is also the only system to provide practical results for radius estimation.

Table 4.3: Comparison of sensor cost for elbow detection, note as the C905 is no longer sold the equivalent available product was used C920

Method	Sensor Type	Sensor	Quantity	Total Cost
Kim et al. [60]	2D LIDAR	Hokuyo UBG-04LX-F01 [74]	1	£1706.11
Choi et al. [27]	IR	Sharp GP2Y0A41SK0F [75]	10	£152.9
	Camera	Logitech C905 [76]	1	
Brown et al.	POT	Bournes 53 series [77]	3	£21

4.2.5 Scalability

The detection method is simulated and tested at the 150 mm size. This section applies the same simulations to the 50 mm pipe to show the method is scalable. The 50 mm pipe has an optimal feeler length of 23.06 mm for maximum change in its angle (α_f) in a short elbow with scaled dimensions for the prototype. Applying the algorithms presented in Section 3.5, the mean error in direction is found. The miniaturised system has a $\bar{\epsilon}_{\theta_d} = 1.81^\circ$. This shows the method is applicable to both the 150 mm and 50 mm diameter pipes and the detection method is scalable.

4.3 Summary and Contribution

The chapter presents a successful algorithm for predicting the corner direction of an unknown elbow ahead of the robot with an absolute mean error 4.69° . It can be extended to estimate the radius with an absolute mean error of $\bar{\epsilon}_R = 0.91$ mm. The corner direction is comparable to the literature and the addition of radius provides an improvement. This method uses the change in angle of three low-cost feeler sensors developed for this task. The method and sensors are scalable to small pipes and are computationally light.

Chapter 5

Robot Design and Development

To be able to test the autonomous controller a robot is required. This chapter presents the development of the design of an in-pipe robot for the task of navigating elbows, with the final prototype (FURO II) presented at the end of the chapter.

Aim of the Robot: As identified in the literature review (Section 2.3.1) there are no suitable methods for controlling a robot to navigate through an elbow. A method of control to tackle this problem is proposed in Section 3.1. The aim of the design and development of the robot is to create a platform that is suitable to test the proposed cornering controller. The robot will act as a mount for the feeler sensors from Section 4.1.1 and allow the controller to be implemented on it. A successful outcome is a system able to autonomously navigate elbows when the proposed controller is used. As such it must meet the following design.

Design: As identified in Section 2.2 a wall-pressing, differential drive, wheeled or tracked robot is selected. For the final prototype a tracked robot is selected as it offers greater traction in comparison to its wheeled alternate. This is important as there may be fluids left inside the pipework (Section 1.1).

Due to the size restraints of working in a 50 mm pipe, the initial target for the prototype is to navigate within a 150 mm pipe (Section 1.3), miniaturisation will be reviewed in the further work of the project.

The contribution of this chapter is the design and development of a differential drive, in-pipe robot with both active and passive wall-pressing for navigating through 150 mm, horizontal and vertical pipes as well as elbows.

To design the tracked prototype, an analysis of current tracked inspection robots has been undertaken.

5.1 Tracked In-Pipe Robots

Moghaddaml and Hadi [78] provide a very detailed review of the current state of the art of tracked inspection robots. The robots from their review as well as other have been summarised in Table 5.1 (This can act as an extension to Table 2.2). A larger view of the table can be seen in the Appendix Table 9.2.

Table 5.1: Design parameters tracked, differential drive robots

Robot		Size		Length	Number of		Wall-pressing		Maximum Speed	Weight	Tethered	Control	
		Diameter Min	Max		Drive Units	Drive Modules	Passive	Active				Autonomous	Manual
Kim et al.	[33]	600	800	680	3	1	No	Yes	217	80	Yes	No	Yes
PAROYS-II	[34]	400	700	390	3	1	Yes	Yes	41.7	7.8	-	Yes	-
FAMPER	[79]	127	157	148	4	1	Yes	No	72.4	-	No	-	Yes
Kwon et al.	[80]	75	105	75	3	1	Yes	No	-	-	Yes	No	Yes
PIC	[81]	254	508	-	3	1	No	Yes	-	-	Yes	No	Yes
Kakogawa	[82]	136	226	235	3	2	Yes	No	230	1.8	Yes	-	-

Designs like the system developed by Kwon et al. [80], are able to navigate junctions such as the T-junction and elbow. The robot uses passive wall-pressing via a central spring, which means the robot cannot control its diameter. This could lead to problems with certain obstacles in the pipe, such as a step change in diameter.

Active wall-pressing via a lead screw can be found on PAROYS-II [34], [35] and the Pipe Inspection Crawler (PIC) [81] is a key design feature that if miniaturised would be applicable to the prototype.

There is a requirement for an autonomous pipe inspection robot for navigating in 150 mm pipes with elbows, due to this a custom prototype is developed for this task.

The key design ideas taken from the literature which are also requirements of the exemplar robot are, the use of active wall-pressing which is required for climbing vertical sections of pipes and obstacle navigation, and the use of multiple powered DUs to give differential drive.

Three DUs is the most common number from the literature as it is the minimum required number to allow control in any direction, robots such as FAMPER [79] utilise four DUs, which has no apparent advantage over three and only adds excess weight and design complexity. The three DUs are normally radially separated by 120° similar to the PIC robot [78]. This layout will be used for the prototype being developed.

5.2 Design Requirements and Constraints

To develop a prototype, basic design requirements and constraints are defined to allow it to complete its aim and navigate through an elbow in a network.

- Ability to climb in a vertical pipe, using wall-pressing.
- Use of three, equally radially separated differential drive units.
- Use of tracks for increased grip.
- Nominally be able to navigate within a 150 mm pipe.
- Navigate with an average velocity of 10 mms^{-1} .
- Physically fit through a $R = 150 \text{ mm}$ short elbow.
- Low-cost, as the robot is disposable.
- Carry equipment for sensing and communication (0.5 kg payload).

These requirements were developed from reviewing the specifications of the robots from the literature (Section 5.1) as well as conversations with representatives from Selafield Ltd and the National Nuclear Laboratory. The designs to achieve the requirements, they have been expended upon in the following.

Dimensions

The robot is required to turn short elbows, which will dictate the maximum length and width to allow it a fit through the corner, and this is shown in Figure 5.1.

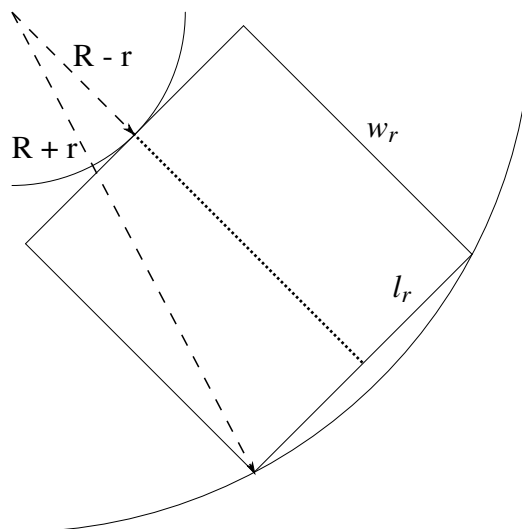


Figure 5.1: Largest robot dimensions to fit around a short elbow

Using Figure 5.1 it can be seen that a triangle can be made to find the length (l_r) and width (w_r).

$$l_r = 2\sqrt{((R+r)^2 - (R-r+w_r)^2)}. \quad (5.1)$$

This formula relates the length and width of the robot. As R and r are known. The ratio can be used in the design process of each prototype.

Mass and Wall-Pressing

To allow the robot to climb in a vertical pipe, the wall-pressing force must be sufficient to stop the robot slipping. To determine the force required (F_N), the weight and coefficient of friction of the robot must be known. The mass of the robot is assumed to be 1 kg with a 0.5 kg payload. This gives a total mass of $m = 1.5$ kg. As the material of the pipe networks are unknown, the coefficient of friction is tested for on multiple materials. To practically test this the track material should be known. The selected tracks for the prototype are the Pololu 30T track set [83], they offer a small, low-cost, fully rubber track that is thin enough to be used on the robot. The coefficient of static friction (μ_s) of the track on the materials is determined by testing the selected Pololu tracks on three surfaces (Aluminium, steel and Perspex). The results are shown in Table 5.2.

Table 5.2: Coefficient of static friction of the selected tracks on various materials

Material	Coefficient of Static Friction
Perspex	0.78
Aluminium	0.56
Steel	0.64

To ensure the robot can climb on all materials, the worst case is used and to take into account any error in the measurements a $\mu_s = 0.5$ is selected.

Now μ_s and m are known, the normal force can be determined,

$$F_N > \mu_s mg, \quad (5.2)$$

where $g = 9.81 \text{ ms}^{-2}$ is the acceleration due to gravity. This gives a required wall-pressing force of $F_N > 7.36 \text{ N}$.

Motor Selection

As discussed in Section 6.2.1, the select number of DUs is three because it is the minimum required number to turn in any direction. To determine the motors for selection a benchmark torque (τ_m) is required.

$$\tau_m = F_m r_w, \quad (5.3)$$

where, τ_m is the torque required by each motor, r_w is the radius of the drive wheel and F_m is the force required by each motor. F_m can be found by reviewing the climbing case again, to accelerate when climbing the robot must overcome the full gravitational force (mg) and the rolling resistance for each track, F_r ($F_r = F_N \mu_r$, where μ_r is the coefficient of rolling friction),

$$3F_m > mg + 3F_N \mu_r. \quad (5.4)$$

μ_r is required to be found, which is done experimentally using the same three materials as the μ_s test (Table 5.2). The results of the rolling resistance test are shown in Table 5.3. Again a worst case is reviewed and a value of $\mu_r = 0.05$ is selected to

Table 5.3: Coefficient of rolling friction of the selected tracks on various materials

Material	Coefficient of Rolling Friction
Perspex	0.043
Aluminium	0.033
Steel	0.035

compensate for any error in the results.

Now μ_r is known and a normal force of $F_N = 7.5$ N is selected to be sufficiently greater than the required wall-pressing force from Section 5.2, the motor force can be calculated using (5.4), $F_m > 5.28$ N and finally the torque can be found, assuming a wheel radius of $r_w = 25$ mm. Therefore, $\tau_m = 0.132$ N.

Another constraint on the motor selection is the physical size of the motor as they must fit in a 150 mm pipe. The selected motors for the robot are GMW32W0950 [84], these are worm gear motors capable of producing 4.30 Nm of torque at stall which comfortably supersedes the required τ_m . The range of GMW32's offer different ratios such that the speed/torque can be altered without changing the design of the robot.

The use of back drivable motors may remove the need for controlling their speeds as the forces in the corner could provide resistance to the motor to alter their velocities

and make the turn. This could be damaging to the robot as the forces from the corner must be greater than the force of the motor, meaning the robot and drive components would be placed under greater stress. It would also have poor efficiency compared to the proposed method of controlling speeds, but would offer a more simple controller as the velocities would not need to be calculated. Due to the large torque requirements of the motors (calculated above), high torque, low-cost motors are not back drivable and the selection of suitable motors would greatly increase the cost of the prototype system.

Now the design constraints are known, the prototyping of the robot can be complete.

5.3 Prototype Development

To reach the final prototype design, took multiple stages of development of the robot, each an improvement of the previous. A short discussion on each will show the evolution of the design and the key challenges faced with each version. Then the final prototype is presented. All the prototype robots were wall-pressing and consisted of three differential drive DUs as highlighted from the literature in Section 5.1. The evolution of the prototypes and their improvements are shown in Figure 5.2.

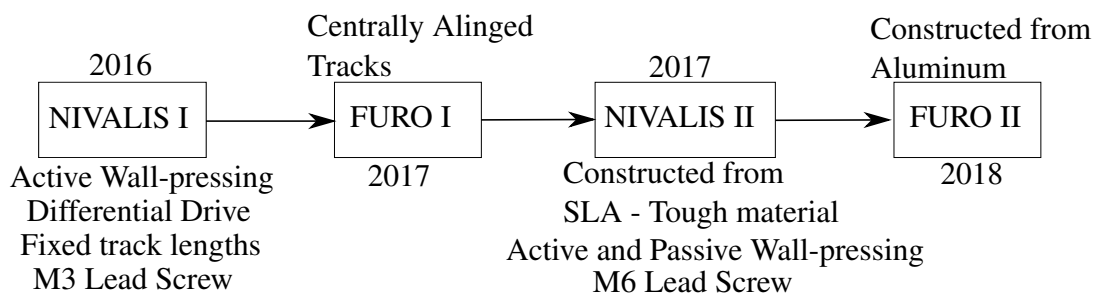


Figure 5.2: Evolution of design improvements through the prototypes

5.3.1 NIVALIS I

There were two versions of the initial NIVALIS I prototype, named from the weasel trinomen ‘*Mustela nivalis*’. NIVALIS I-a (Figure 5.3(a)) used active wall-pressing via a Three Dimensional (3D) printed (PolyLactic Acid (PLA) plastic on a Fused Deposition Modelling (FDM) printer) screw mechanism to provide the normal force required by the robot. The PLA material was found to be too weak to be suitable and was

replaced by an M3 threaded rod in NIVALIS I-b which proved a much sturdier replacement (Figure 5.3(b)). The active wall-pressing using a lead screw is a key design feature from the literature as shown on robots such as the PIC [81].

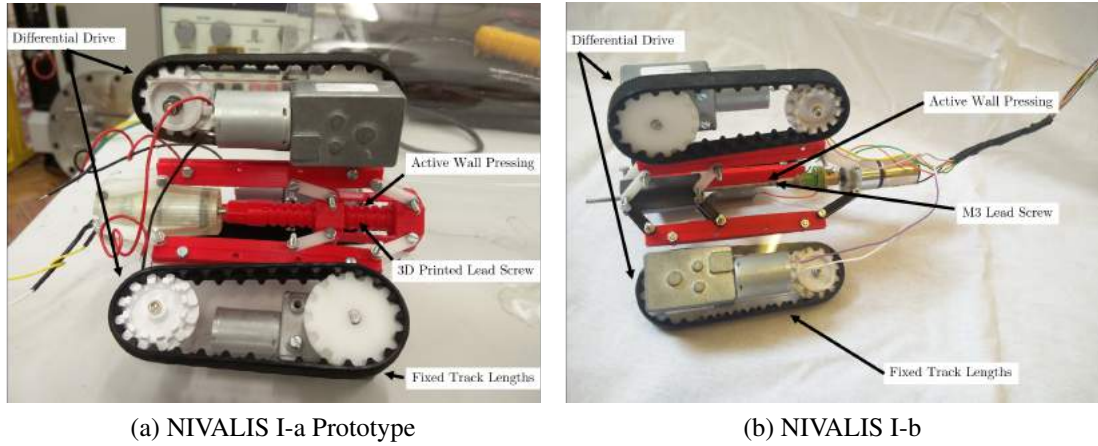


Figure 5.3: NIVALIS I tracked prototypes

The full prototype was constructed for less than £100 and was prominently made from PLA and laser cut acrylic. Both prototypes use the Pololu off the shelf belt kits with a fixed length, but custom cogs were required to allow clearance for the motors on the pipe walls. The NIVALIS I series were a successful prototype achieving both vertical and horizontal navigation in 150 mm pipes. A video can be seen in Appendix, Video 9.1. The major shortcoming with the NIVALIS I design was the tracks not being aligned with the centre of the pipe as shown in Figure 5.4, they have an offset. This causes an uneven force to be put on the track causing it to derail regularly.

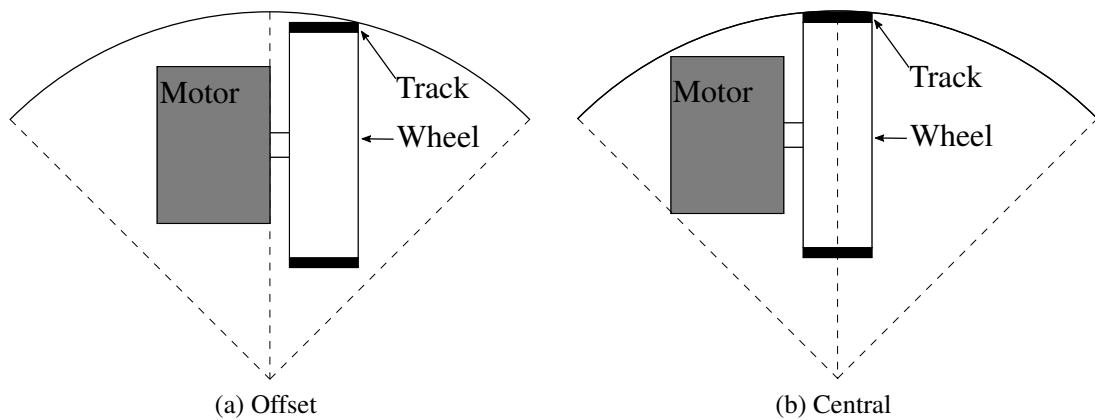


Figure 5.4: Offset and central track alignment

5.3.2 FURO I

FURO I has been inspired by the the design changes and improvements from the NIVALIS I prototypes. It used active wall-pressing via a screw mechanism, fixed track lengths and centrally aligned tracks to remove the derailing issues the NIVALIS I robots faced. FURO is named from the trinomen of the ferret ‘*Mustela putorius furo*’. It is presented in [85] and [86]. The design included guides for the tracks to help reduce the likelihood of derailing. Due to the size of the of the gear motors once the track was centrally aligned custom housings for the gears were made to reduce likelihood of fouling inside the pipe. The robot was constructed from 3D printed PLA and made for less than £100. FURO I is shown in Figure 5.5. It was able to expand and contract between 142.22 - 185.84 mm meaning it could fit in a large range of pipe diameters as well as the target 150 mm.

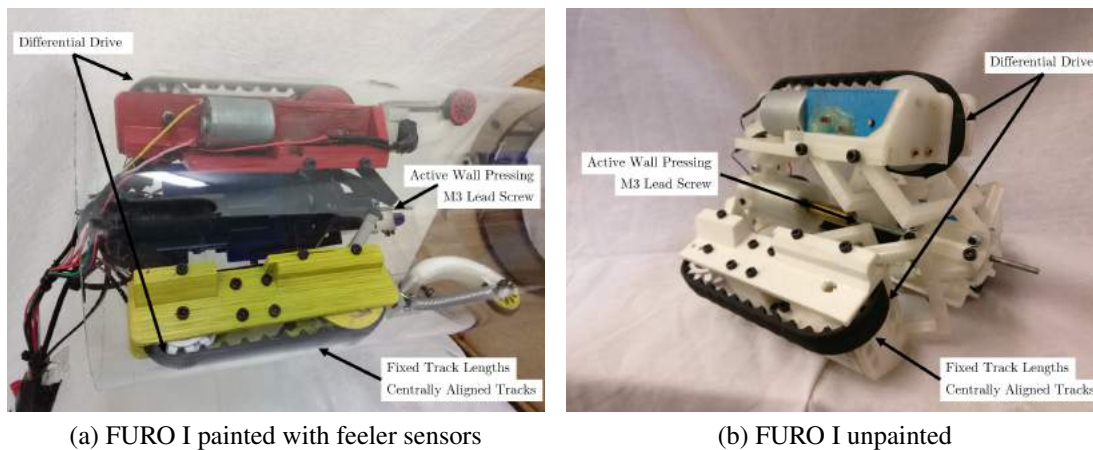


Figure 5.5: FURO I tracked prototype

This was a successful prototype able to navigate through vertical and horizontal pipes and around elbows (see Appendix, Video 9.2). As the robot had a rigid body and no passive wall-pressing there are very large forces exerted on the robot in the corners. This caused the swing arms to break regularly and new materials for construction to be considered as well as some passive compliance to help reduce the effect of the forces. The prototype also had issues with the custom designed gearboxes mainly due to the tolerances of the FDM 3D printed parts.

5.3.3 NIVALIS II

The NIVALIS II prototypes were developed after the FURO I robot. These robots were constructed using a Stereolithography (SLA) printer. This technology offers a higher resolution on prints and materials (Tough [87]) that give higher yield under stress and strain than PLA, which was the major downfall of the FURO I prototype. Designed with all the features of the previous FURO I prototype but with the addition of a sprung sliding section on the lead screw to allow for passive wall-pressing to give compliance in the corners. The combination of both active and passive wall-pressing can be seen in larger robots such as the PAROYS-II [34].

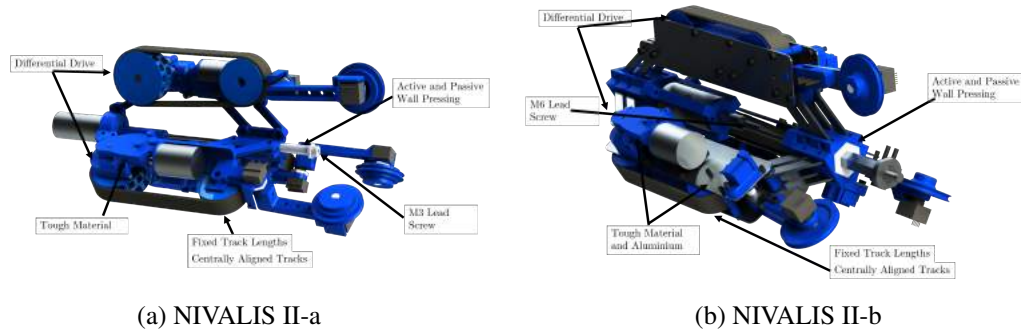


Figure 5.6: NIVALIS II tracked prototypes

The first of the NIVALIS II series of prototypes shown in Figure 5.6(a). They had variable diameters between 121.67 - 151.22 mm for NIVALIS II-a and 125.71 - 171.12 mm for NIVALIS II-b. The use of the SLA printer allowed the structure of the robots to be thinner, such as the custom gearbox housings, meaning they were able to fit in smaller pipes than the FURO I robot which was constructed from PLA. NIVALIS II-a failed due to the thermal effects on the material after being left in a warm environment. The material warped leaving the main structural parts of the robot, such as the swing arms as unusable. This drove the design of NIVALIS II-b to be constructed using aluminium parts in addition to the 3D printed ones for greater support (Figure 5.6(b)). The central lead screw was also uprated to an M6 threaded rod as the M3 flexed under large cornering forces. An extra set of swing arms was added at the rear of the robot to add rigidity to the expansion mechanism. The increase in robustness can be seen in the increase of the minimum diameter of the robot, compared to the previous version.

During early testing it was found the swing arm pairs were placed too close together which allows the DUs to buckle and not keep the tracks parallel with the pipe walls. The

custom gearboxes also proved unable to withstand the forces required by the motors under Brute Force (BF) cornering. Due to this the NIVALIS II series were halted but key design choices such as the addition of passive and active wall-pressing was taken forward to the final prototype.

5.4 Final FURO II Prototype

The final FURO II prototype was designed and built around all the key design features from the previous prototypes. To overcome the derailing which was present on the NIVALIS I prototypes, the tracks are centrally aligned and rail guides are used. Similar to the NIVALIS II robots it featured both active and passive wall-pressing. It also utilised an M6 lead screw to provide greater strength when under cornering forces. The final improvement over the previous prototypes was the selection of aluminium for the main construction to remove the weaker 3D printed parts. The specifics on the design of the robot and implementation of the controller is broken down into sections.

System Architecture

The control of the FURO II robot was implemented on the Robotics Operating System (ROS). ROS is an open-source framework designed for writing software for robots [88]. It is widely used in the robotics community and it offers a flexible solution for programming robots.

A master controller based in a pod on the back of the robot interfaced with the ROS master via a serial link. From here the control was distributed to each DU over a Inter-integrated Circuits (I2C) bus. Figure 5.7 shows the control architecture. Each DU consisted of a micro controller which had a local Serial Peripheral Interface (SPI) bus for reading both the feeler sensor and the track encoder. This microcontroller controlled the motor speed with a velocity PID controller, where the set point was sent from the ROS master and distributed by the FURO master. The set points for the velocity controllers were calculated within a ROS node on the master PC running the autonomous controller.

Active and Passive Wall-Pressing

Similar to PAROYS-II [34] a lead screw mechanism has been designed to give wall-pressing to the system but on a smaller scale. The system had both an active lead screw

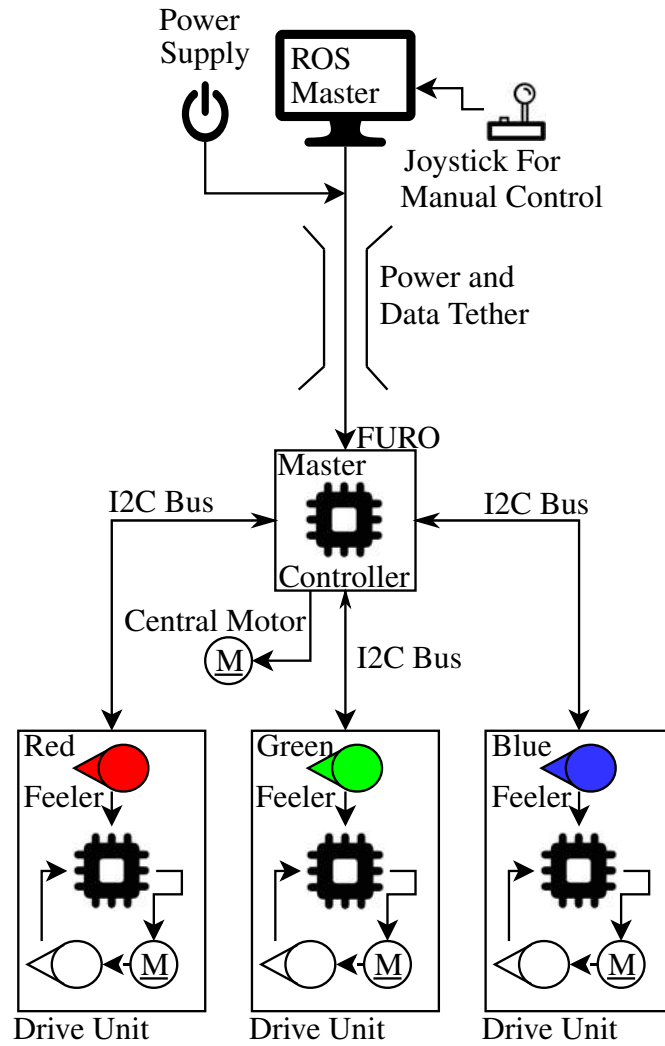


Figure 5.7: System architecture diagram

and a passive spring to press on the walls. A simplified diagram of the setup is shown in Figure 5.8.

To select the spring to give the required force against the walls of the pipe, the worst-case scenario was reviewed, when the robot is climbing in a vertical pipe and is contracted to its minimum. The dynamic model is shown in Figure 5.9.

To ensure the robot will not slip, the normal force calculated in Section 5.2 must be met, $F_N > 7.36$ N. For the case of the FURO II the wall-pressing is a hybrid system with both the lead screw and the spring. For the normal case the spring will provide the wall-pressing force and the lead screw will be fixed, $F_{screw} = 0$ N.

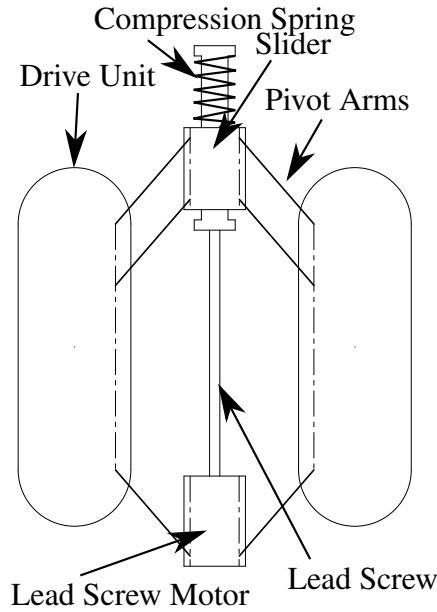


Figure 5.8: Simplified diagram of wall-pressing assembly

The DUs are attached to the centre using pivot arms. As the arms expand and contract their angle changes meaning the transfer of forces varies depending on the radius of the robot. To ensure the robot will work in all pipe diameters, the worst case arm angles (ρ) is reviewed. This occurs when the robot is fully collapsed with $\rho = 5.75^\circ$.

The wall-pressing force is the combination of the individual forces transferred from the three arms,

$$F_N = F_1 + F_2 + F_3. \quad (5.5)$$

Each force can be found using the following,

$$F_1 = \frac{1}{4} F_{\text{spring}} \tan \rho, \quad (5.6)$$

$$F_2 = \frac{1}{4} F_{\text{spring}} \tan \rho, \quad (5.7)$$

$$F_3 = \frac{1}{2} F_{\text{spring}} \tan \rho. \quad (5.8)$$

Combining the forces using (5.5) gives,

$$F_N = F_{\text{spring}} \tan \rho. \quad (5.9)$$

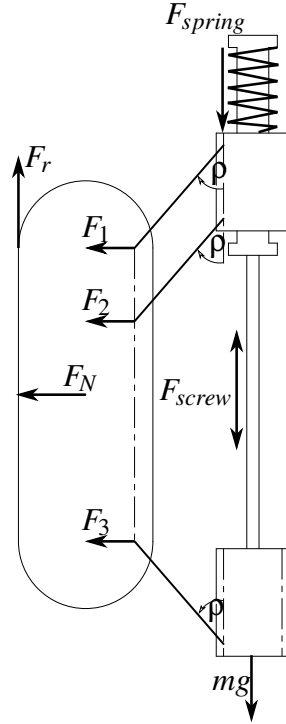


Figure 5.9: Force diagram of wall-pressing

Therefore, to not slide in the pipe when fully contracted,

$$\mu_s F_{\text{spring}} \tan \rho = F_N, \quad (5.10)$$

$$F_{\text{spring}} = \frac{F_N}{\mu_s \tan \rho}. \quad (5.11)$$

Solving to find the required force of the spring gives, $F_{\text{spring}} = 162.53 \text{ Nm}$.

As $F_{\text{spring}} = KX$ where K is the spring stiffness and X is the compression. Using the force an appropriate spring is selected that produces 220.77 Nm at the resting slider displacement of 38 mm. This will provide more than sufficient wall-pressing force.

Using this set up, the passive spring will always apply the required force even in the event of the central motor losing power. The lead screw mechanism can then be used to expand and contract the size as well as provide extra wall-pressing force if required.

Varying Diameter

The passive wall-pressing mechanism presented in Section 5.4 was also designed to give sufficient travel to allow the robot to pass through a corner without the aid of its active mechanism. This means during operation in a 150 mm pipe the robot can

passively reduce its width to the required 137.02 mm to turn the corner. As well as the passive spring there was an active lead screw mechanism. This allowed the diameter to be varied between 137.02 - 243.66 mm. To alter the range of diameters the robot, the pivot arms length can be changed, the selected arms for the given range had a length of 59.5 mm.

To allow the robot to reach the smallest possible diameter, the arms have been designed with opposite bends to allow them to sit parallel with each other at its most compact position (Figure 5.10).

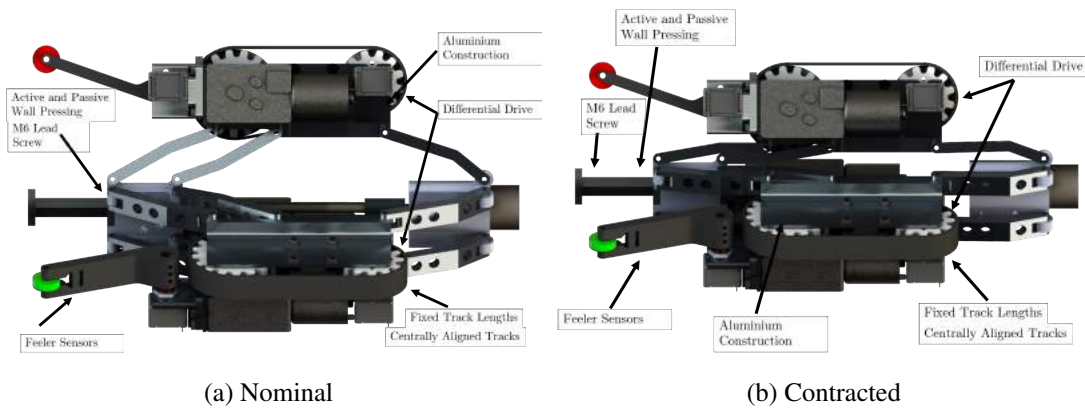


Figure 5.10: FURO II varying diameter

Drive Unit Clearance

As the tracks were centrally aligned and the use of custom 3D printed gearboxes was proven to be problematic, the original gearboxes were used. These were larger than the custom ones previously used which could limit the minimum pipe size, so the laser cut drive wheels were designed to minimise the size of the DU package whilst still clearing the pipe walls. Figure 5.11, shows the method of determining the drive wheel radius (r_w) to give the motor 1 mm clearance on the pipe wall.

$r_w = 23.91$ mm to satisfy the clearance requirements. The assembled DU is shown in Figure 5.12.

The supporting plates were used to not only mount the motors and other components, they also acted as a guide for the track to limit any possible problems with derailing. To aid in velocity control for the robot an encoder was included on the rear custom cog. A custom Printed Circuit Board (PCB) was designed to hold the micro-controller for each 3D. This was responsible for the low-level velocity control on each

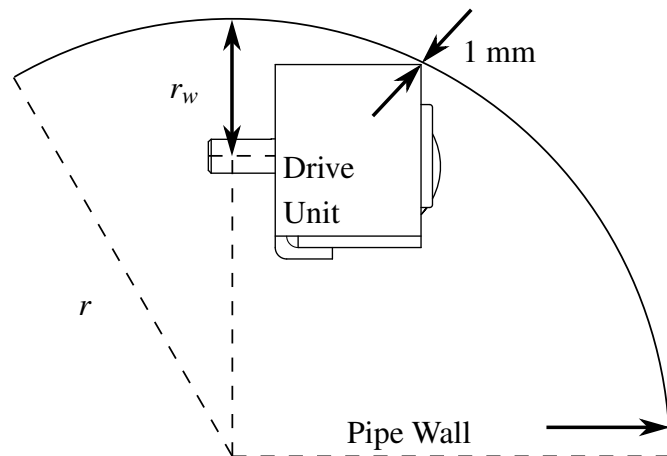


Figure 5.11: Diagram to show drive wheel radius selection to minimise size whilst giving 1 mm clearance

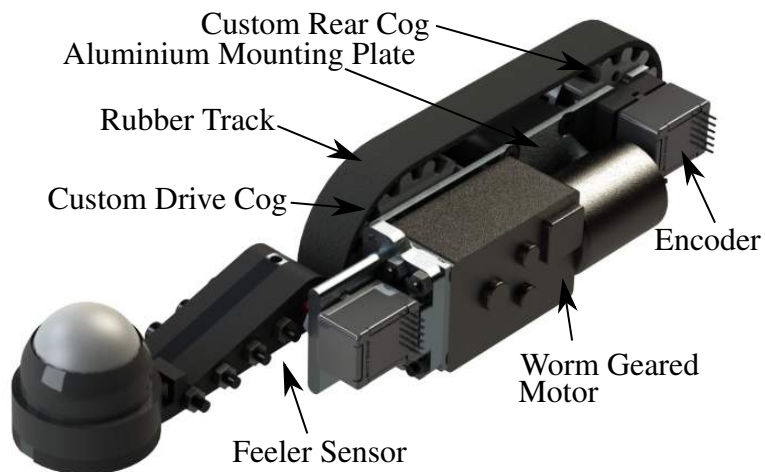


Figure 5.12: Labelled diagram of drive unit

unit and sampling the sensors. The overall control and communication method on the robot is described in the following section.

Final Design

Figure 5.13 shows an annotated image of the prototype. The full design can be found in the Appendix CAD 9.1.

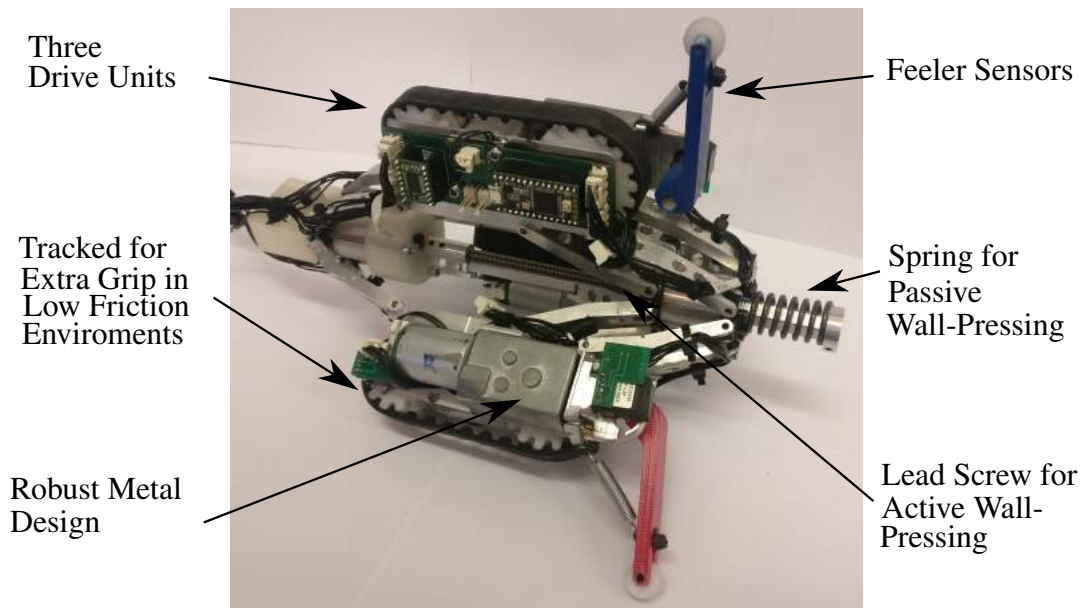


Figure 5.13: FURO II prototype

Table 5.4: Parameters of the custom in-pipe robots developed for this project

Robot		Dimensions			Number of		Wall-pressing		Construction Materials
		Diameter		Length					
		Min	Max		Drive Units	Drive Modules	Active	Passive	
		mm	mm	mm					
NIVALIS	I-a	-	-	-	3	1	Y	N	PLA
	I-a	-	-	-	3	1	Y	N	PLA
FURO	I	142.22	185.84	211.41	3	1	Y	N	PLA
NIVALIS	II-a	121.67	159.22	235.25	3	1	Y	Y	SLA - Tough
	II-b	125.71	172.12	300.12	3	1	Y	Y	SLA - Tough/ Aluminium
FURO	II	137.02	243.66	237.38	3	1	Y	Y	Aluminium

5.5 Summary and Contribution

This chapter presents the development of the final design of the differential drive, wall-pressing, tracked pipe inspection robot FURO II. Five development inspection robots were designed and built with continual improvement before the final design was reached. The key features of each of the robots are summarised in Table 5.4.

The final FURO II is a low-cost platform designed for the task of navigating through 150 mm diameter pipes and turning elbows meeting the requirements at the start of the chapter. FURO II is the test platform that will be used for testing the autonomous elbow controller developed in Chapter 6.

Chapter 6

Autonomous Elbow Navigation Control

It has been identified in that there is a requirement for a differential drive, wall-pressing robot to have a controller to allow it to safely turn corners. From the review of the literature in Section 2.3.1, it can be seen that there are no suitable controllers for navigating around an unknown elbow for the diameters of pipe in question.

The aim of the chapter is the development of an autonomous control system for the navigation of unknown elbows for a differential drive, wall-pressing robot. The controller is designed to overcome the shortcomings in the current methods of turning through elbows in the literature (Section 2.3.1). The full overview of the controller is presented in Section 3.1, this chapter tests the full cycle of the proposed control method. It is tested against the Brute Force (BF) method and will be deemed a success if it shows a significant improvement over this method.

This chapter contains the development of the Autonomous Elbow Controller (AEC). The controller is tested on the FURO II prototype from Chapter 5 and finally the results from the AEC are compared with the BF method to determine its suitability.

The controller takes the inputs from the corner parameter estimation (Chapter 3) to determine the control action and calculate the robots Drive Unit (DU) velocities.

The contribution of this chapter is the development of an AEC that can navigate around elbows with an unknown corner direction θ_d and angle ϕ_d using data from low-cost feeler sensor which is an improvement over the BF method.

Definition Of Autonomy For the presented controller, autonomy is being defined as requiring no human interaction to fully enter, turn and exit the elbow.

6.1 Low-Level Control

Before the development of the full AEC, the low-level control on the FURO II had to be designed and tuned. As introduced in Section 5.4, the low-level control for each Drive Unit (DU) uses a PID controller. This ensures the velocity set points generated by the AEC are followed for each of the DUs.

The controller was implemented using the Arduino PID library [89]. To ensure compatibility with the FURO II micro-controllers as well as the robust design of the controller itself. In order to reduce derivative kick, the derivative gain acts only on the output of the motor rather than the reference signal. The layout of the controller is shown in the Appendix, Figure 9.2. The set point is defined by the overall AEC and the output is the motor velocity measured by an encoder sensor mounted on the idle wheel of the track.

The aim of the low-level controller is to ensure the motor speeds accurately track the set point value. The controller is tuned using a holistic approach, manually adjusting the gains until the desired output is achieved. The final values from the tuning are shown in Table 6.1.

Table 6.1: Low-level controller PID gains

k_p	2.5
k_i	10
k_d	0.005

It can be seen that the integral gain (k_i) is high to ensure the aim of the low-level controller is met and the set point is tracked. Although a high k_i gives quick removal of a steady state error, it can also result in an oscillatory response. However, in this case it is small enough to provide a stable output. The small derivative gain (k_d) gives a slight ramp up to the set point, this reduces current spikes from the motors as the transmission between set points is smoothed out. The proportional gain (k_p) selected as it achieved the required response. A plot of the response of the controller is shown in Figure 6.1.

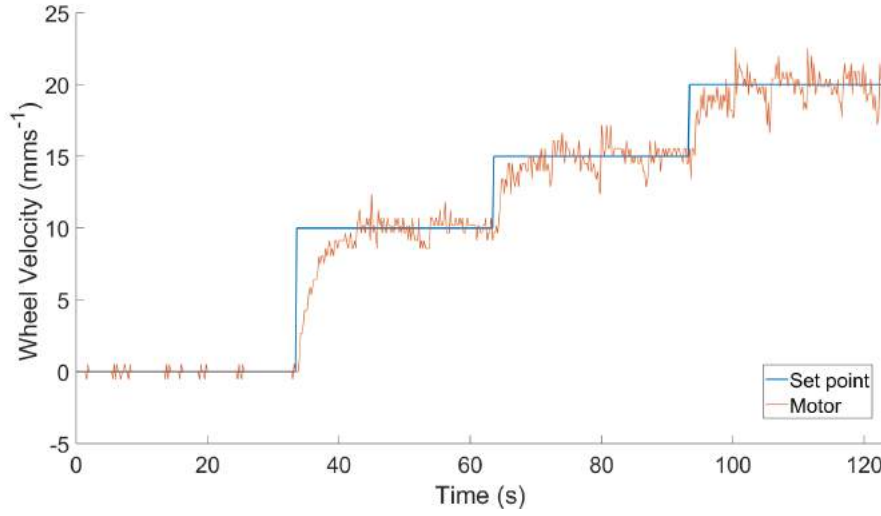


Figure 6.1: Output of the PID controller

It can be seen that there were fluctuations in the output velocity once the set point had been reached, this was due to a mechanical fouling of the drive wheel on the track guides which at a certain point during the rotation would slow the wheel down. Despite the effect of this physical issue, the controller achieved its aim to follow the set point.

6.2 Proposed Method Of Autonomous Elbow Control

The proposed method has two main states of operation, the straight pipe state and the elbow state. The straight pipe state is when the robot is operating within a straight section of pipe, at this time all the differential drive motor speeds are equal and feeler sensors are being monitored for the trigger threshold (T_{start}) to be met. Once the threshold has been triggered the estimation of the corner parameters is completed and the elbow state begins. During the elbow state the AEC is used to navigate through the elbow. Once the elbow state has met its exit conditions (a threshold from feeler data (T_{exit})) it returns to the straight pipe state. Figure 6.3 restates the basic state machine for this with updated information.

Similar to Lee et al.'s [55] method, the elbow is split into three stages: entrance, traversing and exiting. The stages of the controller are shown in Figure 6.2.own further to help explain the processes. In general terms the process is as follows: the robot makes the prediction of corner direction in the entrance phase and calculates the required velocities for each of the robot's DUs based on the estimation. In the traversing stage, the velocities are set for each DU and the robot progresses around the corner.

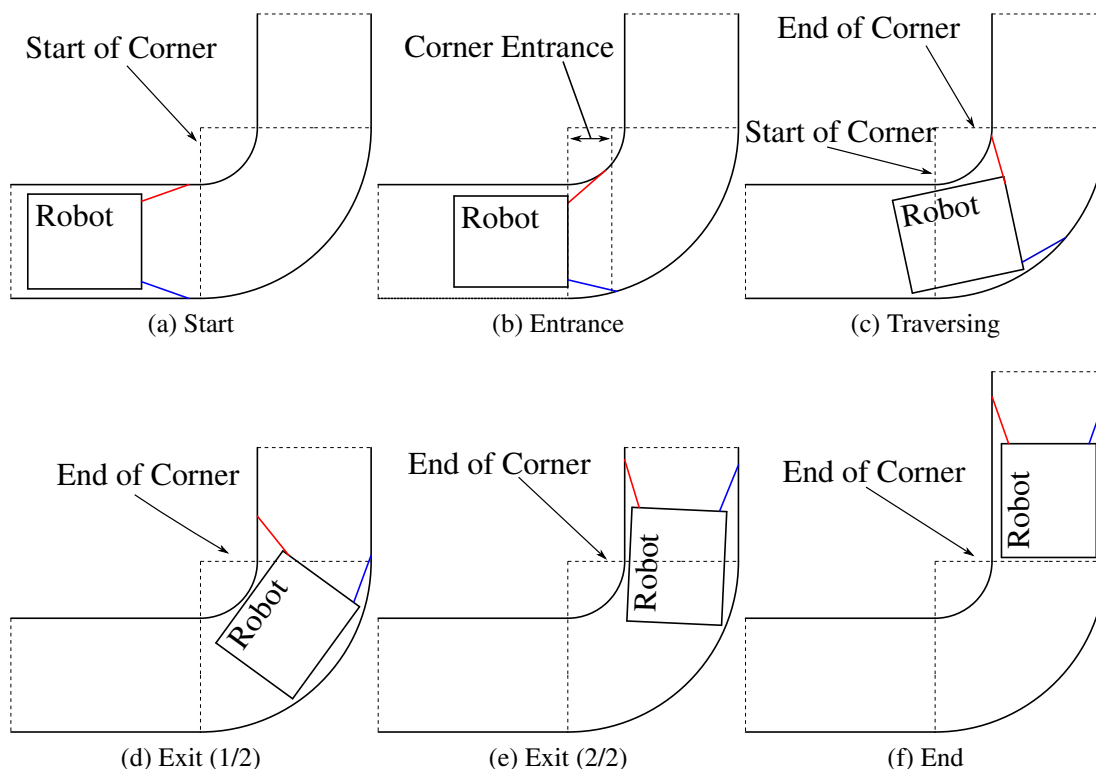


Figure 6.2: Autonomous elbow control stages

The final stage is the exit where the straight pipe is sensed and as the robot leaves the corner the DU velocities are set back to equal and the robot leaves the elbow state. The proposed control algorithm is shown in the Appendix, Figure 9.3.

Note that the velocities being set by the controller are the set points for each of the drive units, $\{V_R, V_G, V, B\}$, each drive unit contains its own closed-loop PID controller to maintain the velocity, as discussed in Section 5.4.

As the proposed method utilises the direction estimation (Chapter 3), the AEC can work in pipes with unknown directions. The required parameters to determine the control action are defined in Section 3.1, all the parameters except the corner angle (ϕ_r) can be determined at the start of the corner. As ϕ_r is unknown the proposed control method of sensing for exit conditions allows the AEC to not need to know the corner angle and is able to navigate an elbow with any angle.

The three stages of the controller are broken down in the following sections.

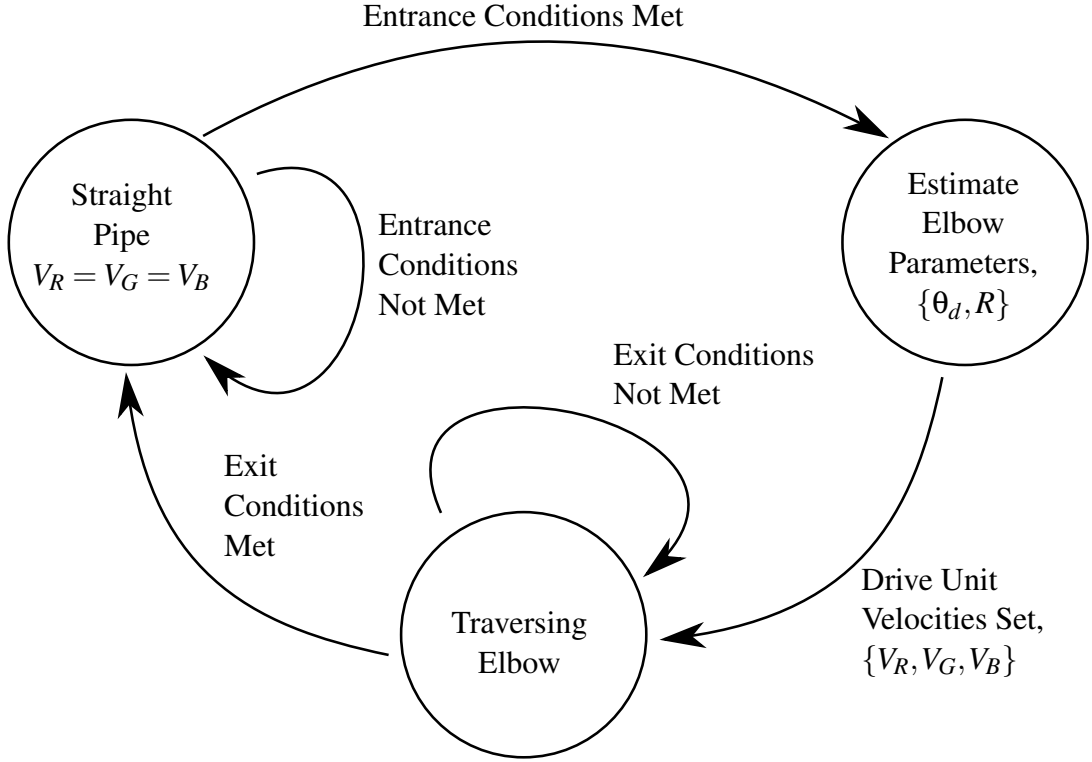


Figure 6.3: Autonomous elbow controller overview updated

6.2.1 Entrance

The entrance section is responsible for the estimation of the corner parameters (Chapter 3). The entrance stage is complete as the main body of the robot enters the elbow. This is when the velocities of each DU are calculated based on the estimation.

To calculate the velocities from the prediction, the radii of the DU paths, R_{path_R} , R_{path_G} and R_{path_B} are calculated. The first step is finding the path length required for each of the three differential DUs. It is initially assumed that the bends are all 90° elbows ($\phi_a = 90^\circ$). Figure 6.4 shows the geometric layout of the three DU's path lengths, l_{path_R} , l_{path_G} and l_{path_B} .

Using Figure 6.4 the equations for the path radii, R_{path_R} , R_{path_G} and R_{path_B} can be found as follows,

$$R_{\text{path}_i} = \sqrt{(R - r \cos(\theta_d + \delta_i))^2 + (r \sin(\theta_d + \delta_i))^2}, \quad (6.1)$$

where $i = R, G$ or B and δ_i is the separation angle of each DU, for this example $\delta_{R,G,B} = [0^\circ, 120^\circ, -120^\circ]$. Once the radii of the path is known, the path length, l_{path_i} , can be calculated,

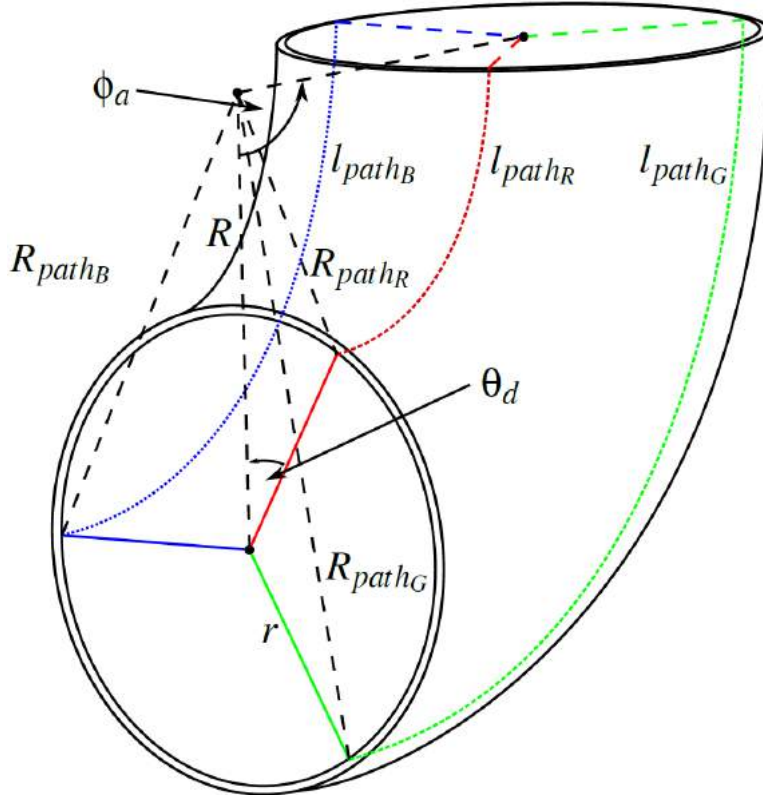


Figure 6.4: Calculating radii

$$l_{\text{path}_i} = R_{\text{path}_i} \phi_a. \quad (6.2)$$

From the path lengths the individual velocities can be determined. The path length of the central path (l_{path_c}) can be calculated and thus the time taken to turn the corner found, $t_{\text{turn}} = \frac{l_{\text{path}_c}}{V_r}$. This can be used to determine the other velocities for their varying path lengths.

Knowing the path lengths vary due to their radii, the prior steps of determining path length and time can be negated as they are constant across all the DUs. This allows the radii to be used to give a ratio with the centre radius which can be treated as a multiplier for the average velocity to give the DU speeds. This also removes the requirement to know ϕ_a if exit conditions can be sensed. The velocities for the drive units, V_i can be found using,

$$V_i = V_r \frac{R_{\text{path}_i}}{R}, \quad (6.3)$$

where V_r is the average required velocity of the robot. Once the velocities are calculated at the end of the corner entrance, completing this stage of the AEC.

6.2.2 Traversing

The traversing phase is categorised as when the robot is within the elbow and driving around the corner. This is where any error in the prediction will show in the form of slip of the tracks.

Due to the reviewed methods in Section 2.3.1 providing limited or no metrics for their cornering methods, the system will be benchmarked and tested against the BF method. The literature is included in the discussion of the experiments for comparison.

The metric selected to review the system is impulse (Ns). Impulse is force multiplied by time, this can be used to not only express the amount of force being exerted on the robot due to error in estimation (causing the tracks to slip) but also the amount of time that is spent slipping by all the tracks. This allows the force exerted on the robot to be expressed whilst also being related to the time. The impulse is used to show the extra force applied to the robot over the time it spends slipping in the corner, it is calculated from the wall-pressing force the robot is able to exert on the walls (Chapter 5). The more force the robot is subjected to, the sooner fatigue and other issues will occur. The amount the robot is required to slip will vary depending on the error in the prediction.

Reviewing the case of a perfect prediction, the required velocities will be calculated correctly and thus no slip will occur, as the paths covered by each DU will end at the same time.

Any error in the prediction will lead to incorrect DU velocities being set for the actual path length. As the robot is a rigid body the DUs will be forced to exit the corner at the same time. Thus, the errors in the velocities must be overcome with slip.

To determine the time spent slipping (slip time, t_{slip}), it is assumed that the cornering time of the robot will be the same as the slowest path, be that a fast track speed on a longer path or a slow track speed on a short path. The difference in path completion time between the drive units is the slip time. Using this slip time the impulse (I) can be determined once the force exerted is known using,

$$I = t_{\text{slip}} F_s, \quad (6.4)$$

where F_s is the force required to overcome static friction. This means it must be greater than the normal force (F_N) being exerted by the robot's spring mechanism and the coefficient of static friction (μ_s),

$$F_s > F_N \mu_s, \quad (6.5)$$

both F_N and μ_s are calculated in Chapter 5. $F_N = F_{spring} \tan(\rho) = 39.05$ N and $\mu_s = 0.5$. $F_{spring} = 220.77$ and $\rho = 10.03^\circ$ these are dictated by design of the robot. ρ is measured from the robot's design when it is at its required width to pass through the corner.

Given both the normal force and the coefficient of friction, the calculated force required to overcome static friction is $F_s > 19.52$ N. Note the force is calculated from the design of the robot rather than measured from the robot. Given this and the slip time, the impulse can be calculated using (6.4) based on the error in the prediction and the BF method.

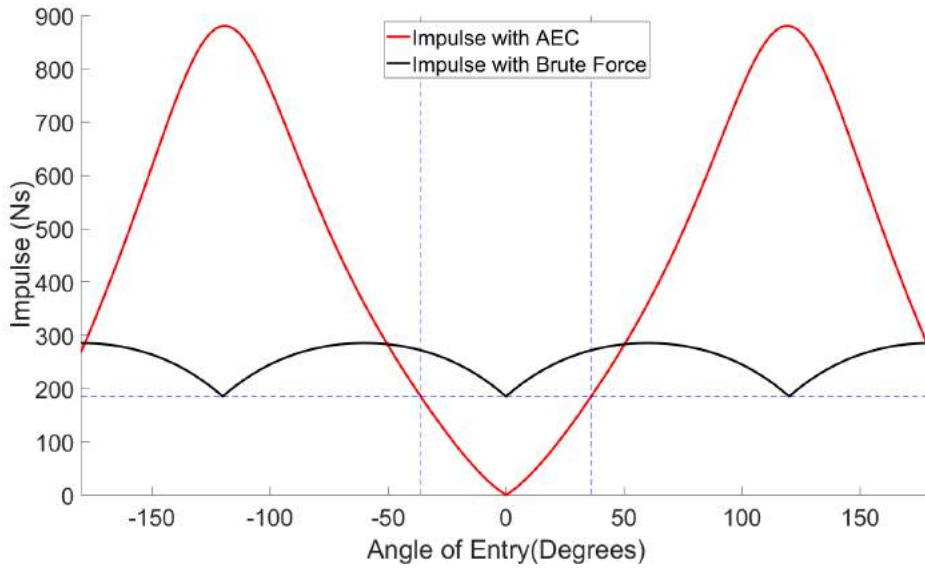


Figure 6.5: Impulse vs angle of entry

Figure 6.5 shows the comparison of the BF method verses corner direction estimation error. Note for the estimation, the prediction is 0° for every orientation, thus making the angle of entry the error in prediction.

The figure shows that as the estimation error increases there is a dramatic increase in the impulse. This peaks at $\pm 120^\circ$ (which are the symmetry points for a robot with three DUs) then drops off again as the predicted velocities become closer to the correct values.

The black dashed plot shows the impulse required using the BF method, again varying as the entry angle changes. The blue horizontal line shows the minimum impulse required using the BF method. With errors in the estimated direction up to $\pm 36^\circ$ the impulse is lower than the minimum of the BF method. Therefore, the target accuracy of the estimate of θ_d must be less than $\pm 36^\circ$, to ensure it is an improvement over BF.

Impulse From Corner Direction Estimation: To determine the suitability of the corner direction estimation from Chapter 3, the error in the estimation of $\bar{\epsilon}_{\theta_d} = 4.69^\circ$ was compared with the required value to better BF $\pm 36^\circ$. It can be seen that the accuracy is sufficient to better BF. Reviewing the error in terms of the increased impulse using Figure 6.5 gives Figure 6.6.

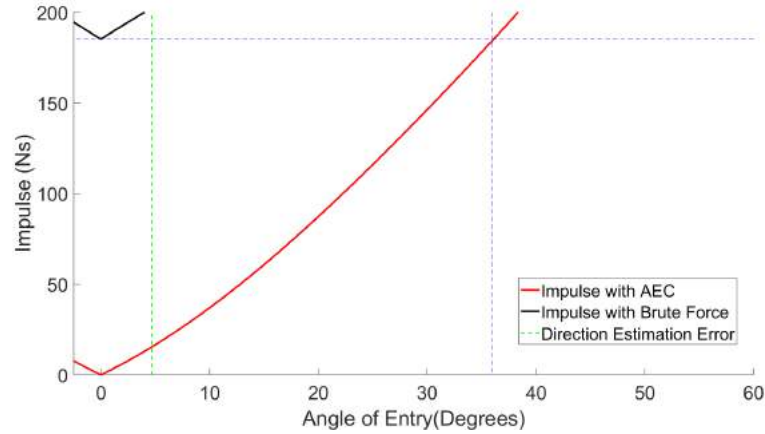


Figure 6.6: Impulse vs angle of entry

The increase in impulse was $I_{\bar{\epsilon}_{\theta_d}} = 15.44$ Ns, comparing this to the minimum increase when using BF $I_{BF_{min}} = 185.1$ Ns showed that the accuracy of the direction estimation system is more than sufficient for the controller.

6.2.3 Exit Conditions

The third stage of the controller is responsible for the robot leaving the elbow and returning to the straight pipe. It does this by determining the exit conditions and using this as a trigger. To find the exit conditions a simulation is developed to determine the feeler angles as the robot passes through the elbow.

To simulate the conditions the corner and robot parameters must be known. The parameters of the robot are taken from the FURO II Prototype presented in Section 5.4, and the corner parameters are taken from a 150 mm standard short pipe elbow.

The simulation generates the path of the feelers as the robot passes through the elbow using a kinematic model and determines the contact point on the inside of the pipe to find the angles of the feelers. A Two Dimensional (2D) simplified diagram of this is shown in Figure 6.7. It can be seen from the figure that as the robot progresses around the corner the feeler angles change. A more detailed view of the model can be seen in Figure 6.8, it shows the kinematic model of the robot in the corner.

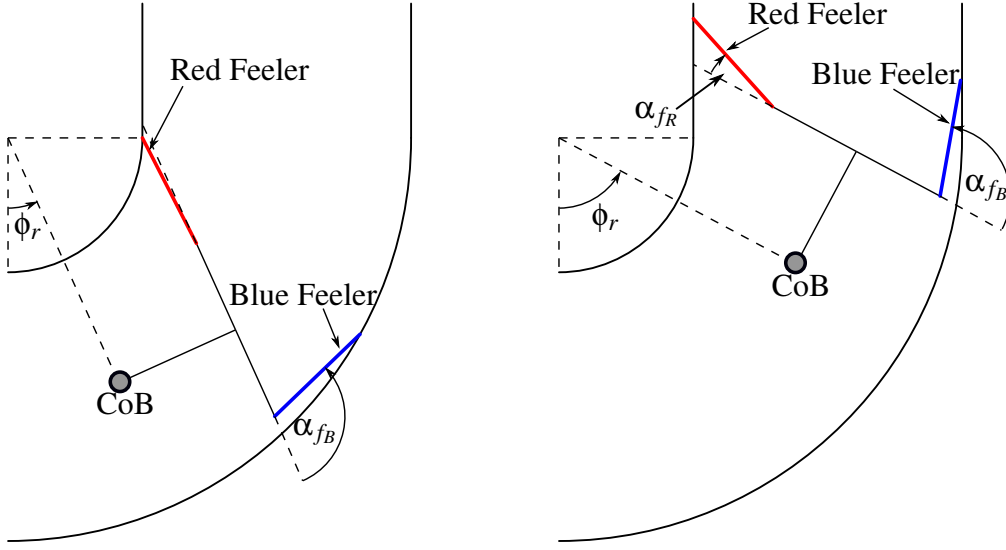


Figure 6.7: 2D simplified diagram of exit conditions

From Figure 6.8, R is the major radius of the pipe, m_l is the length between the Centre of Body (CoB) of the robot to the feeler mounting point, l_l is the height from the feeler mounting point to the centre of the robot and f_l is the length of the feelers. All these variables (except R) are determined by the design of the robot.

To determine the kinematic model intermediate variables, H , A and B are to be found,

$$H = R - (l_l + f_l \cos \alpha_{f_i}) \cos \theta_d, \quad (6.6)$$

where θ_d is the rotation of the robot within the pipe.

$$A = l_l + f_l \sin \alpha_{f_i}, \quad (6.7)$$

$$B = H \sin \phi_r. \quad (6.8)$$

Using A , B and H the feeler end positions can be determined,

$$x = B + A \cos \phi_r, \quad (6.9)$$

$$y = (l_l + f_l \cos \alpha_{f_i}) \sin \theta_d, \quad (6.10)$$

$$z = -H \cos \phi_r + A \sin \phi_r. \quad (6.11)$$

Using the model, the feeler angles can be found as it progresses through the corner. They can be seen in Figure 6.9. Note that it shows only 10 offset angles (in the range 0° to 180°) of rotation, θ_d .

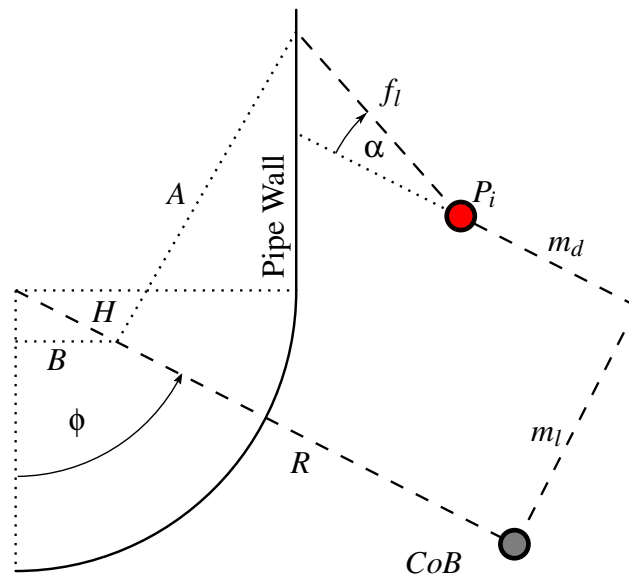


Figure 6.8: Kinematic model of exit conditions

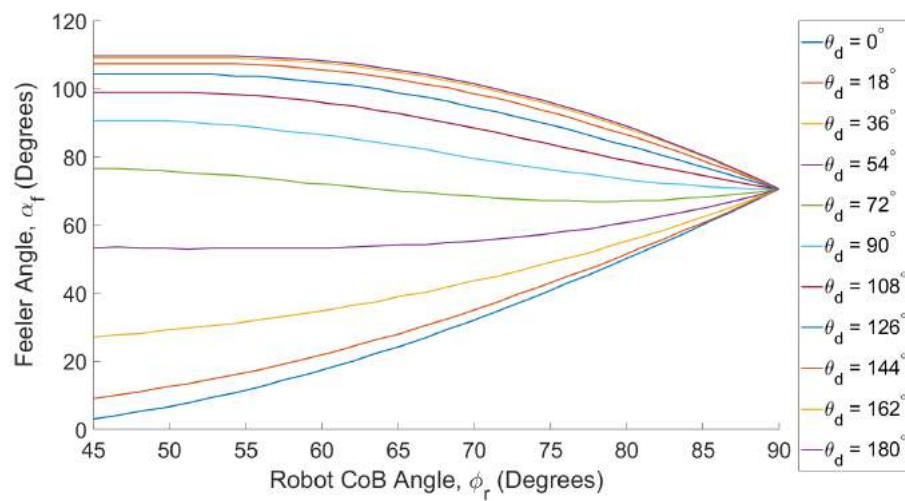


Figure 6.9: Feeler angles of exit conditions

As the robot progresses further into the corner and the feelers transition from the curved elbow to the straight section of pipe, the feeler angles all converge to their normal condition, i.e. when the feeler angle is at $\alpha_i = 70.14^\circ$.

As part of the direction estimation the feeler angles are combined using a kinematic model and summing the end points to give a total change in the robot's local y and z axes (Section 3.5.1). As the magnitude of d_y and d_z is already being calculated (d_{yz}) from (3.9). This magnitude is used for triggering when the robot is back in the straight pipe.

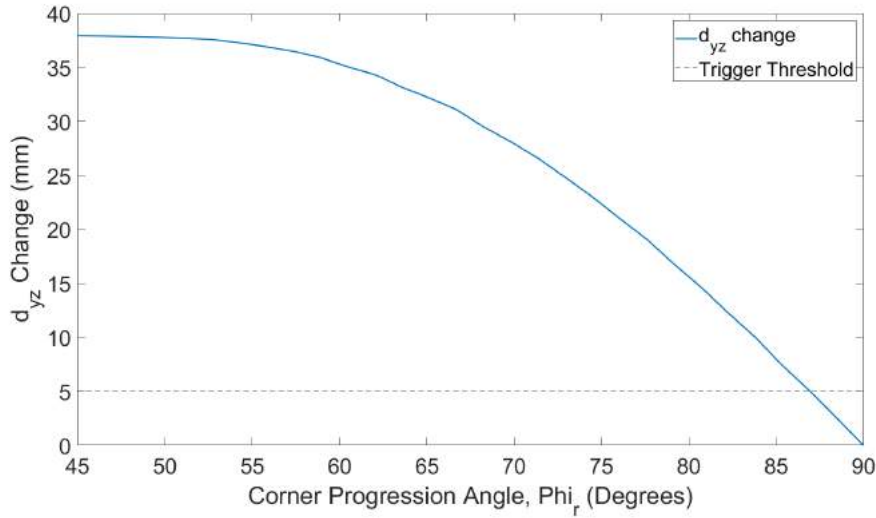


Figure 6.10: Change in d_{yz} as the robot exits the corner

A distance threshold is also set before the straight pipe can be triggered, to overcome any defects in the corner which could artificially lower the d_{yz} value at the start of the traversing stage. Figure 6.10 shows the change in d_{yz} as the robot passes through the corner at $\theta_d = 0^\circ$. As would be expected this tends to zero as the robot enters the straight pipe. The value selected for this was found from experimentation and 5 mm is selected. This ensures the corner is exited and is sufficiently close to the final value to not cause major slipping in the end of the pipe. In the further work section, the possibilities on the tuning of this values will be discussed.

6.3 Experimental Hardware and Method

To test the Autonomous Elbow Controller (AEC), FURO II (Chapter 5) is required to navigate around an elbow and compare the responses for the controlled method and BF method. The data collected as part of this experiment is also used for the verification of the visualisation system. To achieve this a pipe network is required.

Pipe Network: To test the proposed control method, an experimental rig was constructed. The test rig consisted of two 150 mm sections of pipe joined with a short 90° elbow with $R = 152.4$ mm. This is shown in Figure 6.11.

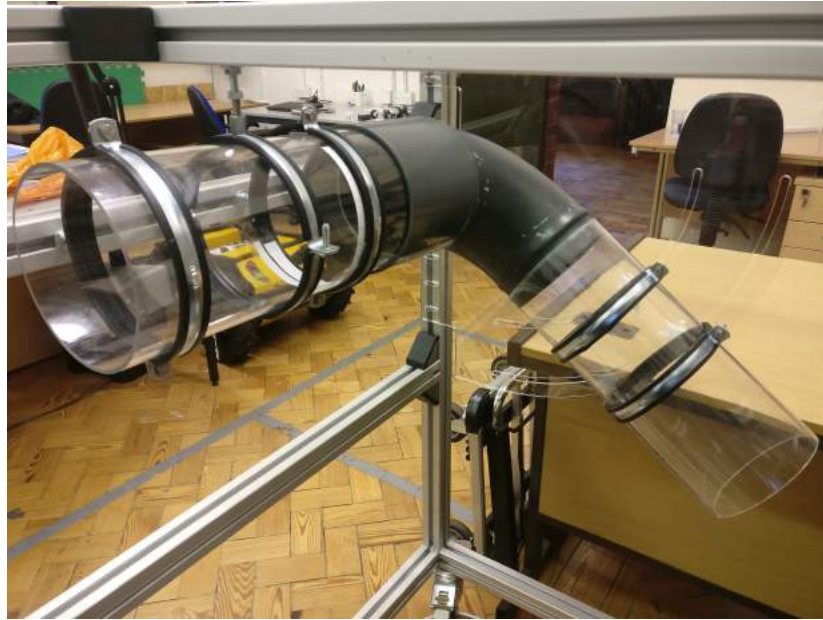


Figure 6.11: Test rig for Autonomous Elbow Controller

Modifications to Feeler Sensor: The feeler sensor designed for the corner direction experiment (Section 4.1.1) when originally mounted on FURO II caused some slight fouling issues at certain orientations within the elbow. Due to this the design was modified to overcome the issues. The feelers' offset from the pipe wall (m_d) was moved from 22 mm to 28 mm and the roller ball was replaced with a smaller low friction wheel. The modified set-up is shown in Figure 6.12. The changes to the feelers were included in the kinematic model for the prediction of corner direction. The Potentiometer (POT)s were also replaced by a high accuracy Bournes EMS22A30-C28-LS6 [90] 1024 ppr encoders to give a less noisy sensor input as recommended in Chapter 4. They have been sampled at 10 Hz, giving approximately 60 samples in the corner entrance.

Experimental Procedure: FURO II was aligned with angle markings on the section of pipe before the elbow in the pipe network and the autonomous mode was started (either AEC or BF), while the robot passed around the corner, the feeler, encoder data and time are recorded. The experiment was run in 10° steps between $\theta = \pm 60^\circ$ and

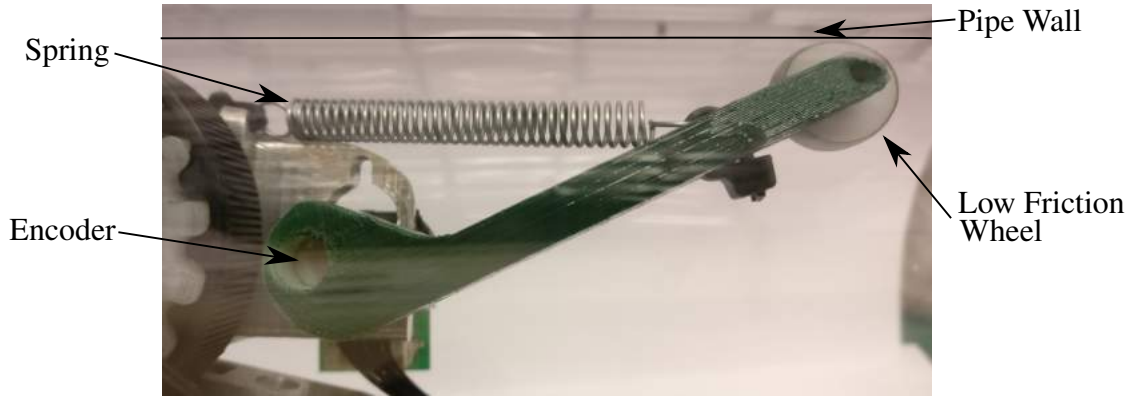


Figure 6.12: Modified feeler sensor

three passes were complete at each angle with AEC running. A smaller sample is taken using the BF method to reduce the damage to the prototype. Both control methods had the same average velocity set point of 10 mms^{-1} . The robot was controlled by ROS, each topic being used is bagged and the time stamp recorded (ROS version: Kinetic, Ubuntu 16.04 LTS [88]). This was be used to determine when the robot is entering and exiting the elbow. The experimental conditions are summarised in Table 6.2.

Table 6.2: AEC experimental conditions

Angle Range	$\pm 60^\circ$
Angle Increment	10°
Angle Repeats	3
Pipe Diameter (r)	150 mm
Elbow Radius (R)	152.4 mm
Elbow Angle (ϕ_a)	90°
Robot	FURO II

6.4 Results and Discussion

This section presents the results from the experiment explained above. It is followed by a discussion of the outcomes of the tests and a comparison with the BF method.

6.4.1 Experimental Results

Figure 6.13 shows the robot passing through the corner, videos of the turning can be found in the Appendix, Video 9.3. In Figure 6.13, the location of the FURO II robot is

Table 6.3: Comparison of target and calculated drive unit velocities

Drive Unit	Target Velocity mms^{-1}	Calculated Velocity mms^{-1}	Absolute Error Velocity mms^{-1}
R	5	5.02	0.02
G	13.23	13.45	0.22
B	13.23	12.99	0.24
Mean			0.16

identified with an arrow. The robot was placed at an entrance angle $\theta_d = 0^\circ$ and was running on the AEC. The robot was able to successfully pass through the elbow for all 39 repeats using the AEC, which proves the effectiveness of the controller.

The results from the experiment are broken down into the three sections to allow a more detailed review of each stage.

Entrance

The entrance stage of the controller is responsible for both the estimation of the corner direction as well as the calculation of drive unit velocities.

The modified feeler sensor are mounted on the FURO II prototype for this set of experiments. The estimation of corner direction was reviewed to determine the effectiveness of the modifications and them being mounted on the robot.

Due to misalignment of the angle marker with the actual corner direction, a systematic error has been removed from the results. The estimate from the AEC testing is shown in Figure 6.14. It can be seen that the predicted angles were close to the true value. The mean absolute error in the prediction was $\bar{\epsilon}_{\theta_d} = 4.01^\circ$ which was an improvement over the results from Chapter 3, which was likely due to the encoders on the upgraded feelers. The estimation was also a significantly less than the required $\pm 36^\circ$ to be an improvement over the BF method.

To review the effect of the mean absolute error on the calculated velocities, they are compared with the target values in Table 6.3 for an average velocity of 10 mms^{-1} and $\theta_d = 0^\circ$. It can be seen that the absolute mean error in velocity was 0.16 mms^{-1} which was a very small differential to overcome.

To express the velocity difference in terms of the time spent slipping, it was assumed that the elbow angle is $\phi_a = 90^\circ$. The $t_{\text{slip}_{\bar{\epsilon}_{\theta_d}}} = 1.36 \text{ s}$ this was calculated by reviewing the time taken to complete each path and summing the difference between them and the maximum time. The slipping force for FURO II in an elbow is calculated

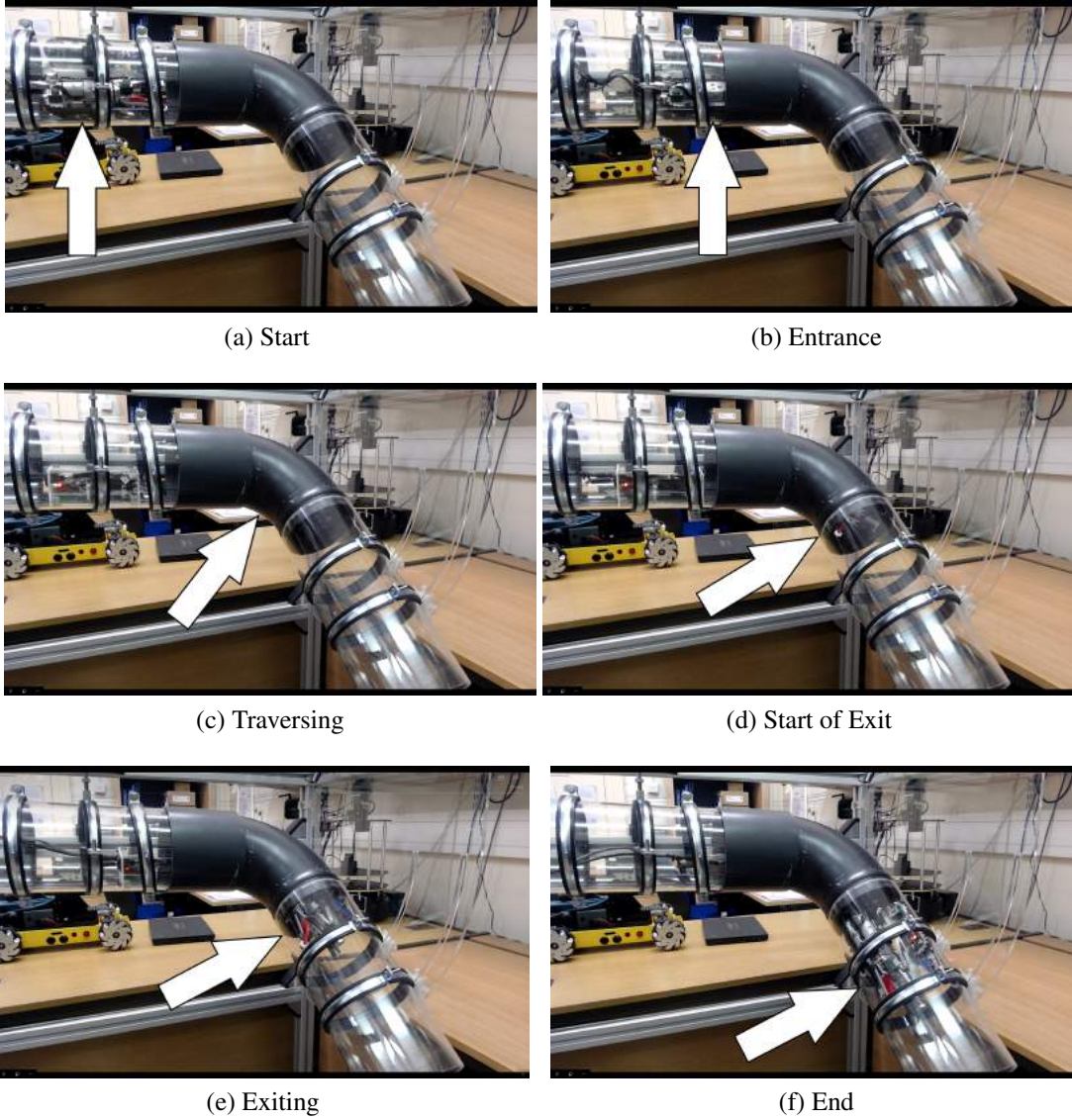


Figure 6.13: FURO-II prototype navigating corner at entrance angle $\theta_d = 0^\circ$

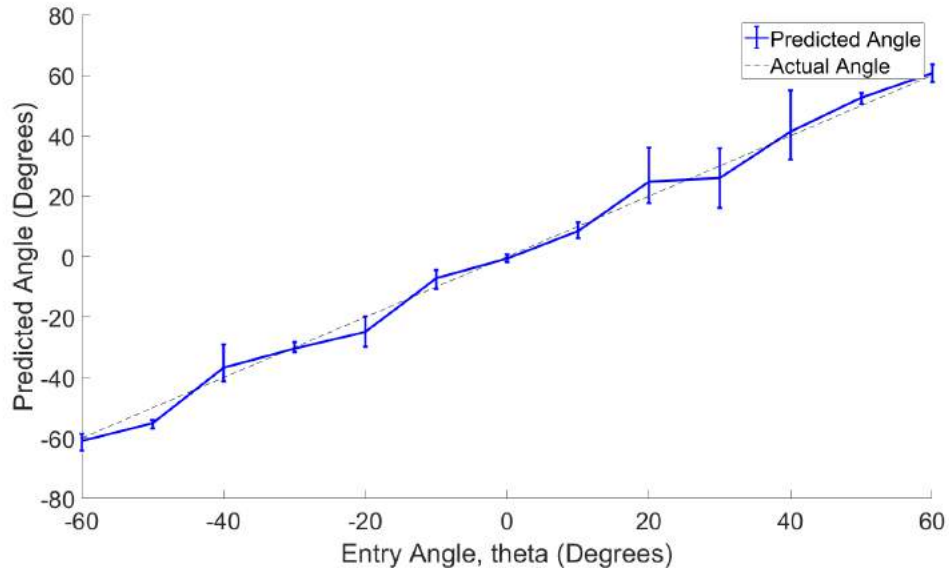


Figure 6.14: Estimated of direction during Autonomous Elbow Controller testing

in Section 6.2.2, $F_s > 19.52$ N. Calculating the impulse from the slip time and force, gives the extra $I_{\epsilon_{\theta_d}} = 26.55$ Ns. For the BF at the same direction and velocity gives, $t_{\text{slip}_{BF}} = 19.39$ s and $I_{BF} = 378.56$ Ns. It can be seen that the estimated value is a significant improvement over the BF method, resulting in a large decrease in impulse exerted on the robot. Thus the estimation with the upgraded feelers on the FURO II robot is suitable for the control algorithm developed in this chapter.

Traversing

To review the traversing section, the time taken for each pass with the AEC is compared with the time taken for BF. Figure 6.15 shows a plot of the time taken for each pass using the AEC and Figure 6.16 for BF. The black bars show when the robot got lodged in the elbow, not completing the turn and receiving a Did Not Finish (DNF) label.

The time for each completed pass is shown in Figure 6.15 and Figure 6.16, the mean values of each entrance direction are shown in Table 6.4. Where Table 6.4 (a) shows the mean time taken for the AEC passes, and Table 6.4 (b) shows the same for BF.

Reviewing the data, it can be seen that the average turning time using the AEC was $\bar{t}_{AEC} = 25.83$ s with a maximum $t_{AEC_{\max}} = 31.20$ s and minimum $t_{AEC_{\min}} = 22.00$ s. For the BF method the average turning time was $\bar{t}_{BF} = 36.08$ (if excluding the DNF results) with a minimum time of $t_{BF_{\min}} = 33.60$ s and maximum of $t_{BF_{\max}} = 41.60$ s.

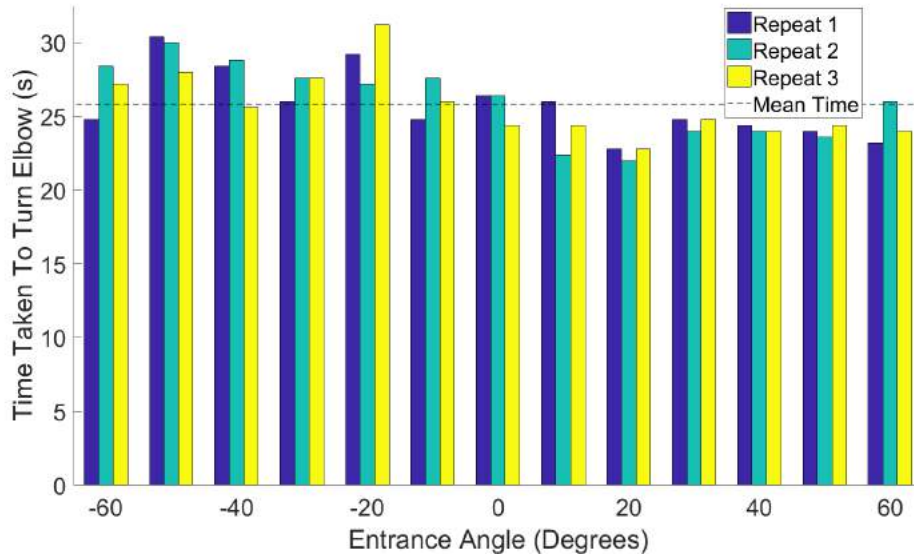


Figure 6.15: Time taken to turn using Autonomous Elbow Controller

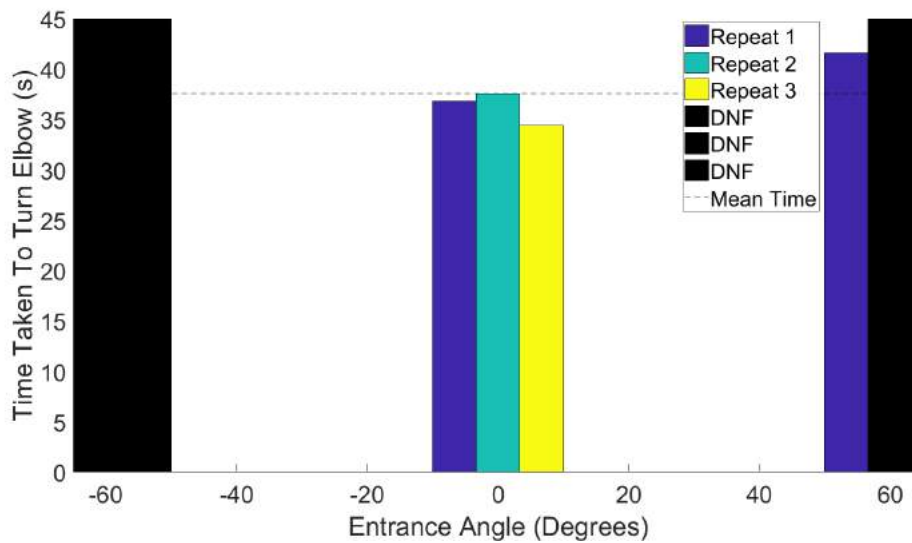


Figure 6.16: Time taken to turn using Brute Force

Reviewing the four DNF passes, three of them occurred at -60° and the final one at $+60^\circ$. The robot was symmetric at those two values where one DU was travelling along the longest path around the outside of the elbow and the other two were equidistant from shortest path. This would mean at $\pm 60^\circ$ the robot would have the most force pushing it in the opposite direction to the corner leading to it getting stuck. This point can be seen in Figure 6.5 where the greatest impulse was subjected on the robot at $\pm 60^\circ$.

Table 6.4: Average time taken for the FURO prototype to turn through an elbow

(a) Autonomous Elbow Controller		(b) Brute Force	
Start Angle	Mean Time Taken	Start Angle	Mean Time Taken
	Closed-loop Control		Brute Force
Degrees	s	Degrees	s
-60	26.80	-60	DNF
-50	29.47	-30	33.60
-40	27.60	0	36.27
-30	27.07	+60	41.60
-20	29.20		
-10	26.13		
0	25.73		
+10	24.27		
+20	22.53		
+30	24.53		
+40	24.13		
+50	24.00		
+60	24.40		

The DNF passes were caused by the force resisting the robot being greater than any forward force the robot can apply, causing the tracks to slip. To overcome this a greater wall-pressing force could be applied. This would increase the friction on the walls of the pipe causing a greater forward force to push the robot through the elbow. The consequence of doing this would be an increase in the forces being exerted on the robot as it is pushing harder against the pipe. This would reduce the amount of slipping time but the impulse (6.4) would still be high as the force component is greater.

An observed event which cannot be seen in the data sets that occurred during the BF testing was the robot skipping teeth on the tracks. This was due to the slipping required and in this case, the slipping occurred on the mating face between the drive cog and the track as opposed to the track on the pipe wall.

The difference in mean time between AEC and BF was $\bar{t}_{\text{diff}} = 10.96$ s. This means on average when using the BF method the robot will slip for 10.96 s more than if using the AEC method. Using the impulse metric presented in Section 6.2.2, to find the average increase in the impulse applied to FURO II in the elbow using the BF method gave, $I_{\text{diff}} = 213.97$ Ns, which was a very large increase meaning there is much greater fatigue on the robot.

Exit

The exit conditions are triggered by monitoring the value of d_{yz} combined with a distance threshold. The simulated change in Figure 6.10 shows all the values converging to zero as the robot exits the corner. The real data of five passes taken at -60° , -30° , 0° , $+30^\circ$ and $+60^\circ$ is shown in Figure 6.17.

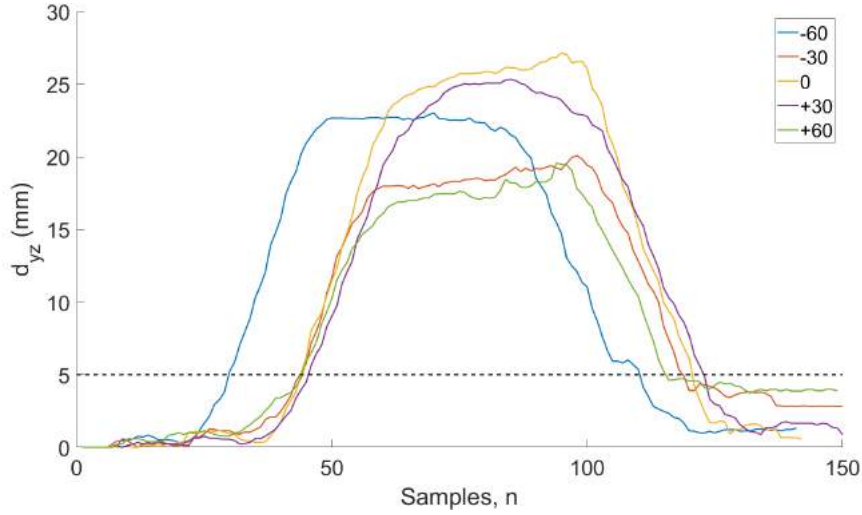


Figure 6.17: Real change in d_{yz} when navigating elbow

The change shown in the figure is for the full turn in the elbow. The initial rise can be seen as the robot enters the corner, the values plateau as the robot is in the traversing phase and finally starts to drop down as the robot exits. The exit triggering threshold of $d_{yz} = 5$ mm is shown on the figure. All the changes dropped below that value, and at that point the DU velocities were set to the straight section of pipe. Further work could be completed on tuning this value.

6.4.2 Discussion

Entrance

The corner direction estimation was an improvement on the experimental values from Chapter 3, with a mean error of $\bar{\epsilon}_{\theta_d} = 4.01^\circ$ comparing to $\bar{\epsilon}_{\theta_d} = 4.69^\circ$. This improvement was likely due to the less noisy encoders used instead of the POTs which were previously used. This result is comparable to the related work by Choi et al. [27] and Kim et al. [60] with mean errors ($\bar{\epsilon}_{\theta_d}$) of 2.84° and 0.64° respectively in their predictions over very limited recorded passes. Both their solutions required large sensors

which would be unsuitable for small pipework and required large amounts of computation.

Comparing the result to the BF method the simulated required accuracy to be an improvement was $\pm 36^\circ$ which the system greatly achieved and reviewing the impulse, it can be seen that the amount exerted on the robot using the AEC was greater than a factor of 10 smaller than the BF method.

This shows that the feeler sensors offers a competitive, low-cost (both financially and computationally) and scalable method for estimating corner direction.

Traversing

The results from the traversing section are shown in Table 6.4. The average increase in time between BF and the AEC was $\bar{t}_{\text{diff}} = 10.96$ s. This was a significant amount of time when the target turning time is $t_{\text{target}} = 23.94$ s. Comparing the AEC time of $\bar{t}_{\text{CLC}} = 25.83$ s to the target time shows there was a small difference. This could be due to errors in the prediction. Despite the slight increase from the target time (t_{target}), the improvement compared to the BF method is clear. The increased time taken by the BF method translates to the extra impulse exerted on the robot of $I_{\text{diff}} = 213.97$ Ns. This is a large amount of force the robot must overcome and could lead to damaging the robot.

In addition to the increased impulse on the robot during multiple passes using the BF method, the robot became lodged in the corner. It would be unsuitable for the intended application of a nuclear environment to deploy a robot which could become irretrievable. The robot did not get lodged during the AEC testing. This clearly highlights the requirement for a controlled method of navigating a corner.

Exit

Looking at the change in d_{yz} from Figure 6.17, the threshold value of 5 mm was suitable to trigger the exit condition and allow the robot to leave the pipe. The final values for each pass are given when the robot is fully in the straight section of pipe. Despite the simulated values returning to zero, in the real results none of them achieve this, with the highest settling around $d_{yz} = 4$ mm. This was due to the robot becoming slightly twisted within the pipe which moved the mounting positions of the feeler sensors. This was caused by slight mismatches in speed of the DUs from errors in the estimation when traversing the corner, as well as minor manufacturing tolerances

in the pivoting legs of the robot which allowed it to move in undesirable ways. This could be addressed in software by resetting the feeler angle when the robot is known to be in a straight section of pipe or manufacturing the robot to tighter tolerances.

6.5 Summary and Contribution

This chapter presents a novel AEC which utilises feeler sensors to safely navigate a pipe elbow with unknown direction and angle. It achieves its aim by using the direction estimation in Chapter 3 as a input to the controller to allow the velocities for each DU to be calculated. The effects of the systematic error were deemed acceptable as the method still offers large benefits over the BF method. The controller exits the corner by sensing a change in the end of the pipe, which allows it to navigate an elbow with any angle (ϕ_a).

From practical experimentation it yielded a decrease of $I_{\text{diff}} = 213.97$ Ns compared to BF and a comparable performance to the state of the art in the literature. Multiple repetitions of the AEC showed that the robot completed the corner on every pass (39 in total), comparing this to the BF method which got lodged in the pipe in four out of nine repetitions shows a significant requirement for the AEC. This method of control is scalable for different sized pipe robots and is low-cost both computationally and financially.

The contribution of this chapter is the development of the AEC controller that is shown to be successful for navigating in-pipe unknown elbows using only three low-cost feeler sensors.

Chapter 7

Pipe Network Visualisation

7.1 Introduction

This thesis presents a controlled method to allow a differential drive, wall-pressing robot to navigating an unknown elbow using low-cost feeler sensors. The aim of the project is to use this robot to navigate unknown pipe networks to geometrically map them. This chapter takes the data from the feeler sensors and on-board encoders and develops the geometric map required for the project.

Aim of the Visualisation System: is to develop a method to generate human readable geometric reconstructions of pipework from the data that would be received from the FURO II robot.

The contribution of this chapter is the development of a mathematical model of a visualisation system that is able to generate pipe networks from the data received from the FURO II prototype, to show the feasibility of the method.

Requirements for Visualisation: As described in the introduction (Chapter 1), the use of the robot being developed is to aid in the decommissioning of pipe networks. The robot will allow only the contaminated section of pipework be identified so they can be removed. The system needs to be human readable so the initial benchmark for the accuracy of the system is ± 0.5 m for straight sections and $\pm 15^\circ$ for elbow angle and direction. This will ensure the generated network is representative of actual one navigated by the pipe robot.

7.2 Pipework Mapping and Reconstruction

There are numerous works on sensing pipe networks, these have been covered in Section 2.4. Few of these are used to generate maps of the pipework as in most cases the map is already known. Yatim et al. [91] provides an overview of various mapping techniques, this as well as others have been expanded upon below.

Much work has been complete using passive Pipe Inspection Gauge (PIG) robots, Santana et al. [92] use an extended Kalman filter to reconstruct the path taken by a PIG using its internal Inertial Measurement Unit (IMU). The landmarks can be detected using this and significantly improved their reconstruction. Ekpemu and Aloba [93] use laser scanners to reconstruct the pipework. However, it is used for the identification of defect in the pipe rather than mapping the network itself as well as this off the shelf laser sensors are unsuitable for miniaturising down to a 50 mm pipe.

Many methods using cameras exist such as, Thielemann et al. [94] use a time-of-flight camera to detect landmarks within the pipe, while being demonstrated as effective further work is required to make the system more robust including the addition of an IMU. Hansen et al. [95] have developed a mapping and visualisation system which uses a camera with a fish eye lens. Cylinder fitting constrains the reconstructed camera images to give the correct distances to ± 1 % and junctions are fitted to the identified areas from the camera. This works only on a single plane which limits the junction directions dramatically.

Most camera based systems use specialist fisheye cameras but Kahi et al. [96] use an off the shelf monocular camera for their Three Dimensional (3D) reconstruction, their method is successful but fell short in pipes with small features, thus requiring specialist lighting to help illuminate objects.

Work on reconstructing unknown pipe networks has been covered by Rho et al. [97] where they combine their camera landmark recognition system and pose sensing with the reconstruction of pipework and successfully recreate the traversed pipe network. Once the camera has identified a junction and direction this feature is added to the map. This method works in systems where the elbow type is known, i.e. its radius and turn angle but could fall short if those were variable.

Lee et al. [56] uses the change of angular velocity to predict corner direction using an IMU. Zhang et al. [98] also use an IMU with the addition of an odometer combined using an extended Kalman filter to successfully map a 3D pipeline with a maximum

height error of 60 mm. The result is compared with a more accurate ductrunner mapping system made by REDUCT which has a more complex sensing suite and a maximum height error of 40 mm. Both these systems have small errors in their maps, due to eventual drift of the IMU, but they are mounted on passive robots and pulled through the pipe, meaning there would be no effect from electromagnetic noise from nearby motors, if applying this to a self-propelling robot, they may become unsuitable. Due to clear success of the IMU methods, the addition of one will be discussed in further work.

The MagneBike [99] utilises 3D odometry and 3D laser scanning to reconstruct images of the complex pipelines the robot is travelling within large 16 inch pipes, again the size of the laser scanner would be unsuitable for this project.

Lee et al. [100] represent the pipe network in a symmetrical matrix by assuming the network consist of nodes (junctions) and lines (straights). This allows a computer to easily handle the map. This matrix is populated by their robot when navigating through the pipe. During their experiments it is shown that the assumed the angle for corners are fixed at 90° and $R = 1.5D$, where D is the diameter of the pipe. As the direction, radius and angle need to be variable for the visualisation, this method is unsuitable.

7.3 Method

The proposed method is similar to the solutions by Rho et al. [97], Hansen et al. [95] and Lee et al [100], which use their sensor data combined with pre-defined features to build the visualisation. The method is also matrix based similar to Lee et al. [100] but instead of using the matrix as the map, a matrix will be used to describe the link between each feature, where a feature is a straight, elbow, junction, etc.

For the proposed application the estimation of the corner direction using the feeler sensors (Chapter 3), combined with the on-board encoder data will be used to fit the feature in the appropriate places.

As the robot can navigate around bends with an unknown direction (θ_a) and angle (ϕ_a) the visualisation method is required to be able to handle and correctly visualise the information to an accuracy of $\pm 15^\circ$. As a method of extending the detection system to estimating the radius is also proposed, being able to visualise different major radii will also be required.

The method utilises homogeneous transformation matrices to describe the changes

in corner angle, direction and radius in elbows as well as pipe length in straight sections. Homogeneous transformations allow us to describe the transforms between different frames using a single standard form matrix [101]. These can be combined to give the change along a whole sequence of frames, where a frame is the local coordinate system of each feature. The homogeneous matrix (H^m) has the general form,

$$H^m = \begin{bmatrix} R^m & T^m \\ 0 & 1 \end{bmatrix}, \quad (7.1)$$

where R^m and T^m are the rotation and translation matrices. They can be found by reviewing the required transformations for the visualisation system. These can be determined by reviewing a simplified example which is shown in Figure 7.1. This shows two straight sections of pipe of length l_1 and l_2 joined by a 75° elbow. The transforms describe the changes each of the feature frames (P_0, P_1, P_2, P_3).

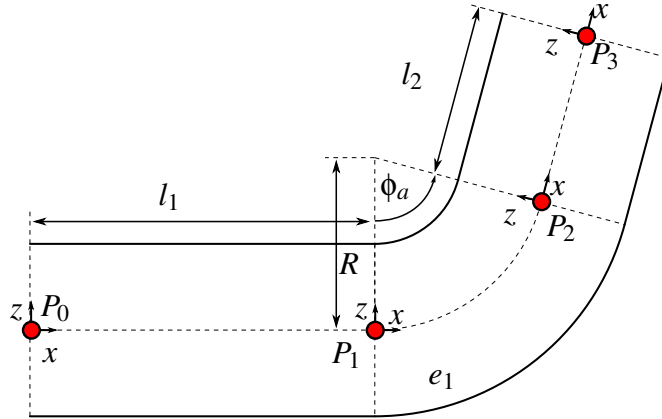


Figure 7.1: Basic example of pipe network

The initial conditions for the starting point are set at the first coordinate frame P_0 . It can be seen to transform from P_0 to P_1 for the straight pipe only a translation in the x direction is required of length l_1 . The elbow transform is more complicated. Figure 7.2 shows a 3D diagram of the exemplar pipe network, where the corner direction (θ_d) and corner angle (ϕ_a) can be seen. The first transform required is to align the frame with the corner axes, which is a rotation around the x axis or roll (Φ). Once the frame is aligned with the corner, two translations are required, one in x (d_x) and one in z (d_z), which is better shown in Figure 7.3. Now the location of the end new frame is correct, one final rotation is required to align it with the direction of the next feature (P_{1_d} to P_2). This final rotation occurs around the y axis or pitch (Θ) and is equal to the inverse of the corner angle (ϕ_r).

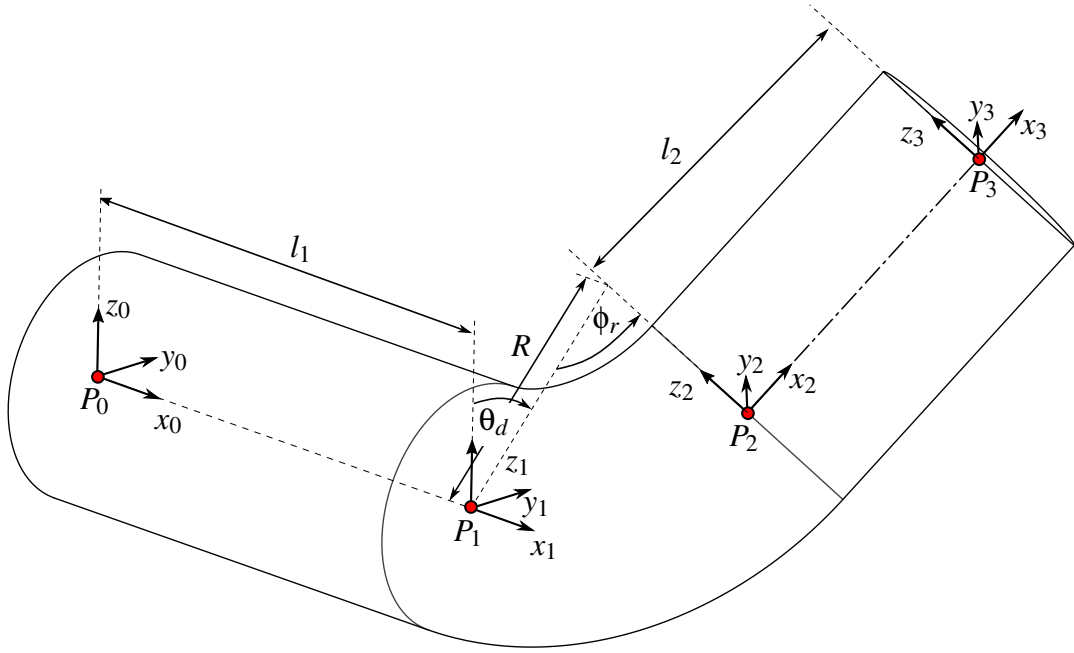


Figure 7.2: Basic example of pipe network (2/2)

The change in x and z shown in Figure 7.3 as d_x and d_z , can be calculated using the corner angle (ϕ_r) and the radius (R),

$$d_x = R \sin \phi_r, \quad (7.2a)$$

$$d_z = R(1 - \cos \phi_r). \quad (7.2b)$$

The transformation matrices for the identified straights and elbows can be determined. For a translation of d_x in x ,

$$T_x^m = \begin{bmatrix} 1 & 0 & 0 & d_x \\ 0 & 1 & 0 & 0 \\ 0 & 0 & 1 & 0 \\ 0 & 0 & 0 & 1 \end{bmatrix}, \quad (7.3)$$

and d_z in z ,

$$T_z^m = \begin{bmatrix} 1 & 0 & 0 & 0 \\ 0 & 1 & 0 & 0 \\ 0 & 0 & 1 & d_z \\ 0 & 0 & 0 & 1 \end{bmatrix}. \quad (7.4)$$

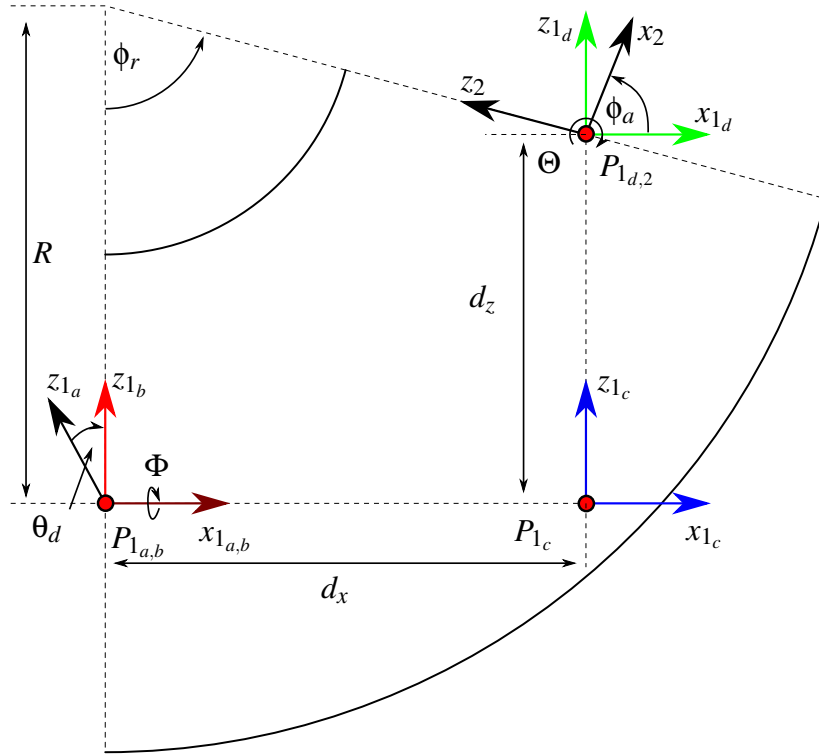


Figure 7.3: Transform of elbow from basic example of pipe elbow

For a rotation of Φ (roll) around x ,

$$R_x^m = \begin{bmatrix} 1 & 0 & 0 & 0 \\ 0 & \cos \Phi & -\sin \Phi & 0 \\ 0 & \sin \Phi & \cos \Phi & 0 \\ 0 & 0 & 0 & 1 \end{bmatrix}, \quad (7.5)$$

and for a rotation of Θ (pitch) around y ,

$$R_y^m = \begin{bmatrix} \cos \Theta & 0 & \sin \Theta & 0 \\ 0 & 1 & 0 & 0 \\ -\sin \Theta & 0 & \cos \Theta & 0 \\ 0 & 0 & 0 & 1 \end{bmatrix}. \quad (7.6)$$

(7.3) - (7.6) are taken from [101].

These can be combined to form the homogeneous transformation matrix (H^m), the order in which they are multiplied is important as that is the order in which they are performed when being used. The roll will be completed first (R_x^m), which will align the axes with corner direction, then the x and z translation to the end point (T_x^m and T_z^m), followed by the final pitch to the corner angle (R_y^m):

$$H^m = R_x^m T_x^m T_z^m R_y^m = \begin{bmatrix} \cos \Theta & 0 & \sin \Theta & d_x \\ \sin \Theta \sin \Phi & \cos \Phi & -\cos \Theta \sin \Phi & -d_z \sin \Phi \\ -\sin \Theta \cos \Phi & \sin \Phi & \cos \Theta \cos \Phi & d_z \cos \Phi \\ 0 & 0 & 0 & 1 \end{bmatrix}, \quad (7.7)$$

this describes the transform from P_i to P_{i+1} .

The variables for each H^m matrix can be determined from the robot's sensor data. The encoder readings from each Drive Unit (DU) are used to determine distances for each feature. For the straight section of pipe, there are no rotations and no translation in z only in x thus $\Theta = 0^\circ$, $\Phi = 0^\circ$, $d_z = 0$ m and $d_x = l_i$ m. The pipe length l_i can be found by taking the average change in distance of each encoder between the previous feature and the next.

The change in features are identified by the triggering points for the cornering controller, the corner parameter estimation acts as the start of a corner and provides its direction and radius and the triggering of the exit conditions acts as the end of the elbow and the start of a straight.

As ϕ_a is not known, it can be determined from the path lengths of the DUs in the elbow. The change in distance for each DU can be easily found as the path length at the trigger points for corner entrance and exit are known. Another constraint on the angle is the standard elbow angles, it is assumed that the elbows are in 45° steps. To find ϕ_a , (6.1) can be used to estimate the path radius (R_{path_i}) for each DU,

$$R_{\text{path}_i} = \sqrt{(R - r \cos(\theta_d + \delta_i))^2 + (r \sin(\theta_d + \delta_i))^2}, \quad (7.8)$$

given the elbows major and minor radii (R and r), the offset of the drive units δ_i . Using this with (6.2) rearranged to make ϕ_a the subject,

$$\phi_{a_i} = \frac{R_{\text{path}_i}}{l_{\text{path}_i}}. \quad (7.9)$$

Note for each DU a separate ϕ_{a_i} is calculated, these are averaged to give a final estimated ϕ_a for the corner. The averaged value is then round to the nearest 45° as manufactured elbows are predominantly produced in those intervals.

Once the H_i^m matrix for each feature has been determined, the coordinates of each frame (P_i) can be found. This gives the path of the Centre of Body (CoB) of the robot. The network shown in Figure 7.1 will be used as an example,

$$P_1 = P_0 H_1^m, \quad (7.10a)$$

$$P_2 = P_0 H_1^m H_2^m, \quad (7.10b)$$

$$P_3 = P_0 H_1^m H_2^m H_3^m, \quad (7.10c)$$

where H_1^m describes the transform from P_0 to P_1 , H_2^m describes the transform from P_1 to P_2 , etc. To extend this to any frame P_i along the path,

$$P_i = P_0 H_1^m \dots H_{i-1}^m H_i^m, \quad (7.11)$$

allows the visualisation system to be extended to very large numbers of junctions. When travelling through a network with multiple elbows the robot's estimations are always made from its local z axis. The visualisation rolls its global axis to be in line with the direction elbow to allow for the generation of the features. The following estimation is then made from the robot's axis again which are now rotated in comparison to the global axis. To compensate for this, the next elbows roll takes the current estimation and negates the previous one from it, which allows for the correct reconstruction of the robot's data.

$$\Phi_i = \theta_{d_i} - \theta_{d_{i-1}}. \quad (7.12)$$

Once the path of the CoB is found the pipe is then constructed around it. It is assumed that the CoB of the robot travels through the centre of the pipe, as wall-pressing robots generally have rigid bodies this is realistic. The pipe is generated in features, a step size and point number can be defined to make a more or less dense image. The features are defined in normal Cartesian space, for a straight pipe,

$$S_x = -\delta_s, \quad (7.13a)$$

$$S_y = R \sin \delta_r, \quad (7.13b)$$

$$S_z = R \cos \delta_r, \quad (7.13c)$$

for an elbow,

$$S_x = (R + r \cos \delta_r) \sin \delta_a, \quad (7.14a)$$

$$S_y = r \sin \delta_r, \quad (7.14b)$$

$$S_z = R - (R + r \cos \delta_r) \cos \delta_a, \quad (7.14c)$$

where δ_s is the step distance, δ_a is the angle step distance, δ_r is the rotation step angle this is defined by the density of points on the plot.

Once these have been generated, they can be transposed to the correct location using the H_i^m matrices, note they are generated back from the frame. The construction of the basic example from Figure 7.1 pipe network is shown in Figure 7.4.

The method of using the H^m matrix allows the elbows direction (θ_d), angle (ϕ_a) and radius (R) to be varied which was a requirement of the system. Figure 7.5 shows examples of different combinations of θ_d , ϕ_a and R .

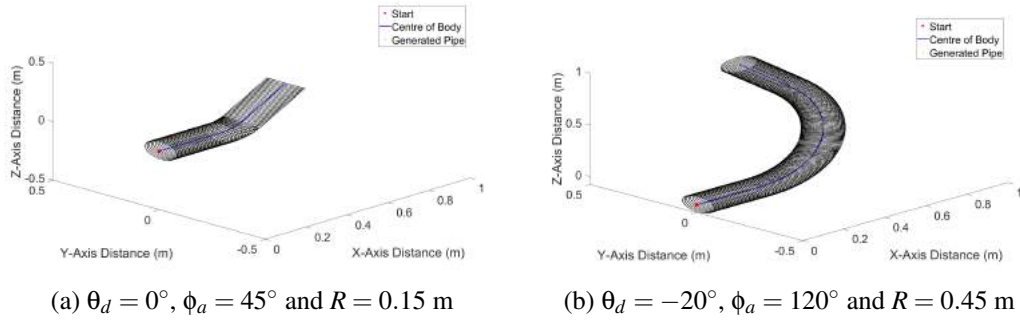


Figure 7.5: Pipe visualisation with varying elbow direction θ_d and angle ϕ_a

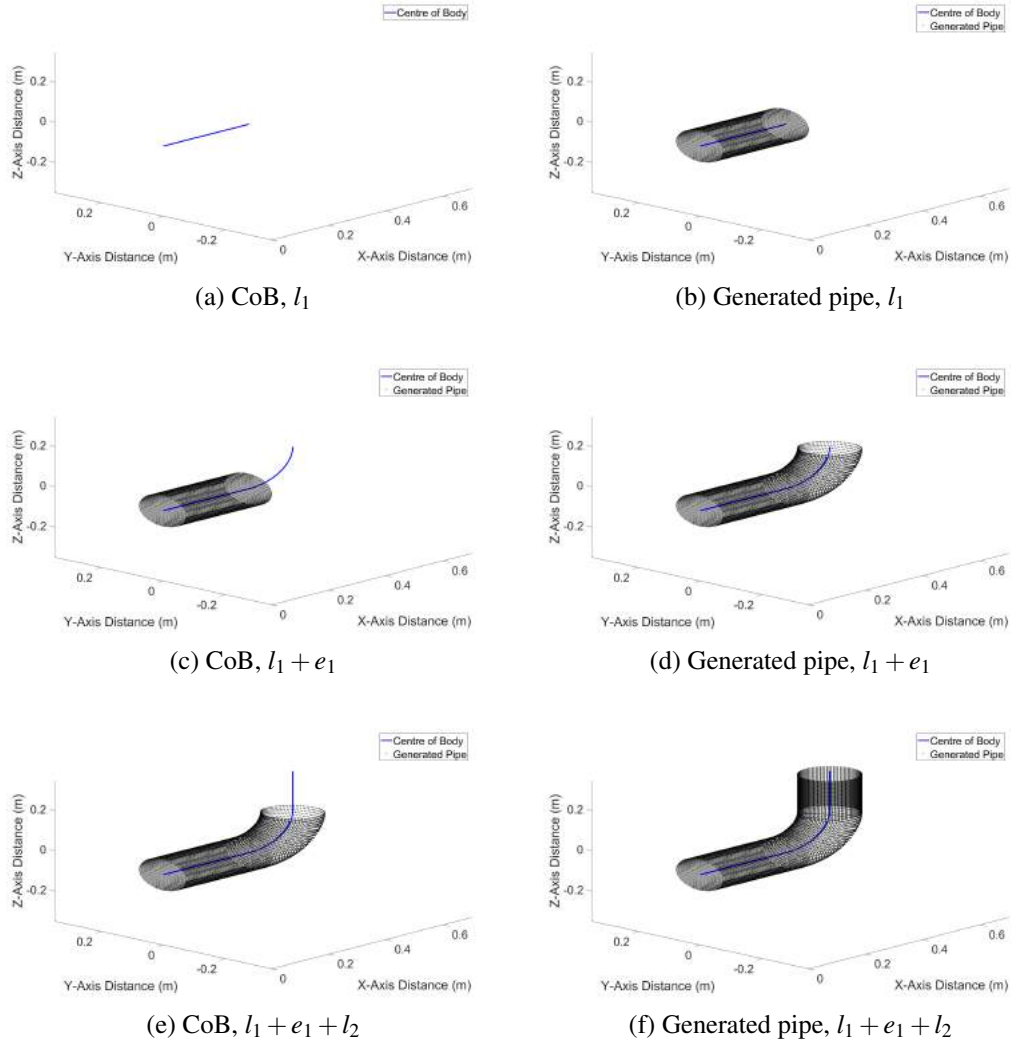


Figure 7.4: Pipe visualisation example

7.4 Simulation of Pipe Networks

To test the extendibility of the visualisation system, the a set inputs (distance and parameter estimation) from the robot have been generated to mimic that of it travelling around a pipe network. As the system takes distance from each DU, corner direction estimation and the trigger points for the elbow entrance and exit these are all generated. For these simulations the radius was assumed to be fixed as a standard short elbow.

7.4.1 Network

The simulated network is a complex example, consisting of four straights followed by four elbows. The parameters are shown in Table 7.1. The Network was successfully visualised, as shown in Figure 7.6.

Table 7.1: Feature parameters for the network

Feature	Length (l_i) m	Direction (θ_d) °	Angle (ϕ_a) °
s1	0.5		
e1		-45	90
s2	0.3		
e2		45	180
s3	0.6		
e3		45	45
s4	0.5		
e4		-15	30

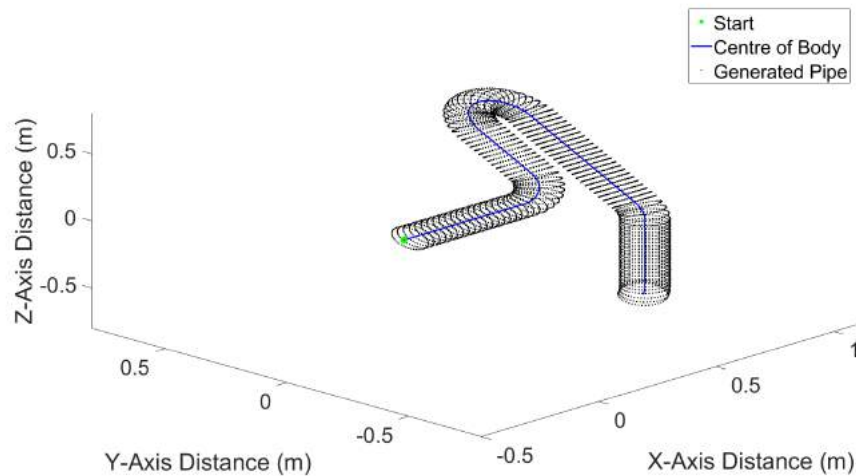


Figure 7.6: Visualisation of the network

This shows the method of visualising the pipework is suitable for large networks. As the system is also required to display the radiological map, simulated hotspots will be added in the following section.

7.5 Simulation of Hotspot Detection within a Pipe Network

The map will be used to determine the location of hotspots of radiation, as no active testing has been completed by the robot this will only be shown in simulation. This is to show the visualisation system's ability to overlay data on to the generated pipe network, which could be used for radiometric characterisation.

Network 2 was used as the template for visualising the hotspots. The inputted data for the visualisation software to simulate the radiometric sensor was given as a positive reading at a specified distance along the pipe.

To visualise that hotspot, the distance was used to determine the feature on which it occurs and the distance along that feature. Once the location had been found a red ring was generated and transformed using the H^m matrices to the correct location. Figure 7.7 shows four visualisations of network 2 with hotspots at different locations, shown as red rings.

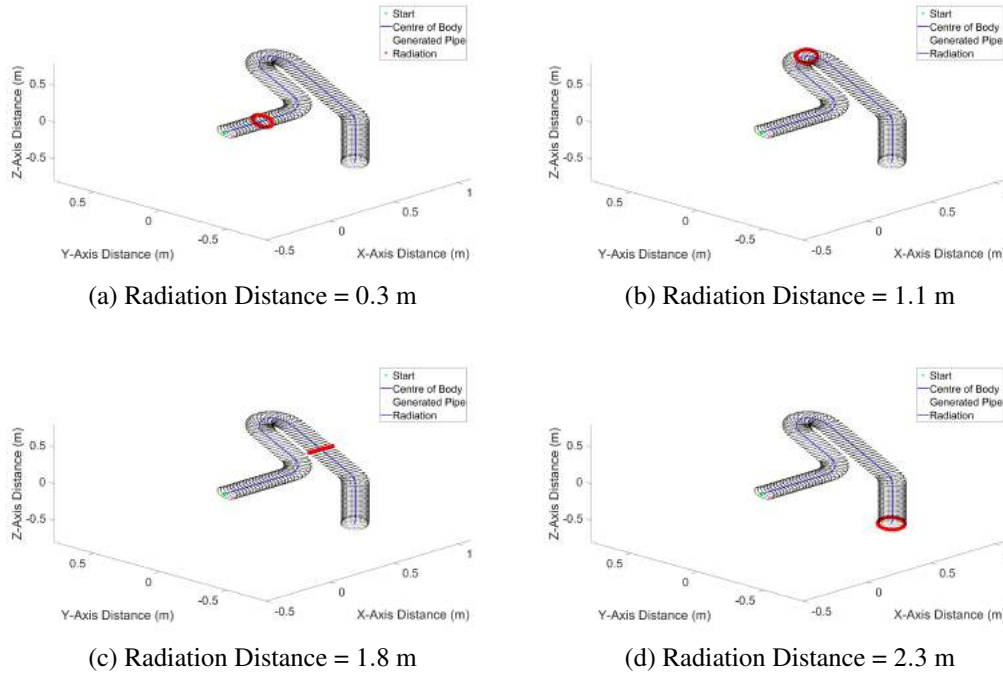


Figure 7.7: Visualisation of Network 2 with radiation hotspots

Despite the ring being in the correct location, as the radiation has been modelled as a single ring it is not truly representative of the data reading a radiometric sensor would

receive, but this proves the feasibility of visualising hotspots on top of the network. This method could be extended to give a more accurate representation of the radiation. However, it will be part of the discussion for the further work of the project.

7.6 Extension To Different Junction Types

This section presents the proposed method of extending the visualisation system to different junction types. The examples used is the T-junction. This assumes the T-junction can be identified as part of the robot's control system. If a T is identified, the transform for one leg of the T-junction will be generated ($H_{T(a)}^m$) depending on the path taken by the robot. This point can now act as a branch to the system as any feature past that point will only be transformed by the $H_{T(a)}^m$ matrix. If the robot returns to the T-junction and goes in another direction, the transform for the other leg will be generated ($H_{T(b)}^m$) and features after that point will only be transformed by the $H_{T(b)}^m$ matrix making a branch in the transforms. This in theory works for any number of splits as long as they can be identified by the robot. Giving an examples of the network shown in Figure 7.8

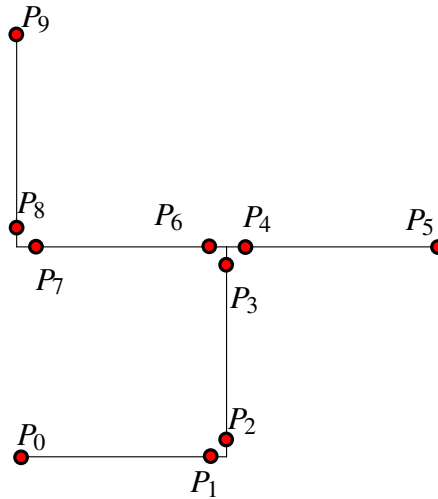


Figure 7.8: Network with T-junction

The position of the frames for each junction is shown on the figure. The order the robot visits the frames can be seen from the number, where it starts at P_0 and ends at P_9 . To show the method of dealing with branches the transforms from P_0 to P_5 and P_0

to P_9 are as follows,

$$P_5 = P_0 H_1^m H_2^m H_3^m H_{T(a)}^m H_5^m, \quad (7.15a)$$

$$P_9 = P_0 H_1^m H_2^m H_3^m H_{T(b)}^m H_7^m H_8^m H_9^m. \quad (7.15b)$$

It can be seen that the transforms for the T-junction, $H_{T(a)}^m$ moves from P_3 to P_4 and $H_{T(b)}^m$ moves from P_3 to P_6 . It can also be seen that to describe the translation to P_9 the transforms for the other side of the T ($H_5^m H_{T(a)}^m$) are not used. This allows more complex junction types to be described by the same format of transformation matrices.

7.7 Visualisation of Real Data

To test the visualisation system on real data from the FURO II robot, the Autonomous Elbow Controller (AEC) test data was post processed for inputs to the system. The test setup for the AEC is shown in Figure 6.11. It was a single elbow linked with two straight sections of pipe. The major radius of the elbow and pipe radius were assumed to be known as $R = 0.1524$ m and $r = 0.075$ m. The corners angle ϕ_a and direction θ_d were be calculated from the sensor data.

Six passes were selected for visualisation, the direction and repeat number were selected randomly to give a representative spread of data. The datasets are, $\theta_d = -50^\circ$ repeat 2, $\theta_d = 40^\circ$ repeat 2, $\theta_d = 60^\circ$ repeat 1, $\theta_d = -10^\circ$ repeat 1, $\theta_d = 30^\circ$ repeat 3 and $\theta_d = -10^\circ$ repeat 2. The selected data sets are compared with the simulated output of the visualisation system. The simulated data was generated from the same elbow parameters as the real elbow but with the target θ_d and a fixed corner angle of $\phi_a = 90^\circ$.

The visualisation system takes the corner direction prediction from the robot and the distances travelled then estimates the corner angle (ϕ_a) for each of the elbows. The resulting visualisations and the simulated outputs are shown in Figure 7.9.

It can be seen that there are some errors present in the difference between the visualisation of the real data and the simulated output. The estimated parameters are shown in Table 7.2. Comparing the results to the required value angular accuracy of $\pm 15^\circ$ (Section 7), it can be see that only the result (a) (-50° , repeat 2) is outside the desired value.

To improve the output, rounding can be used to correct the corner angle (ϕ_a) as elbows are only manufactured to standard angles. The addition of filtering and a better

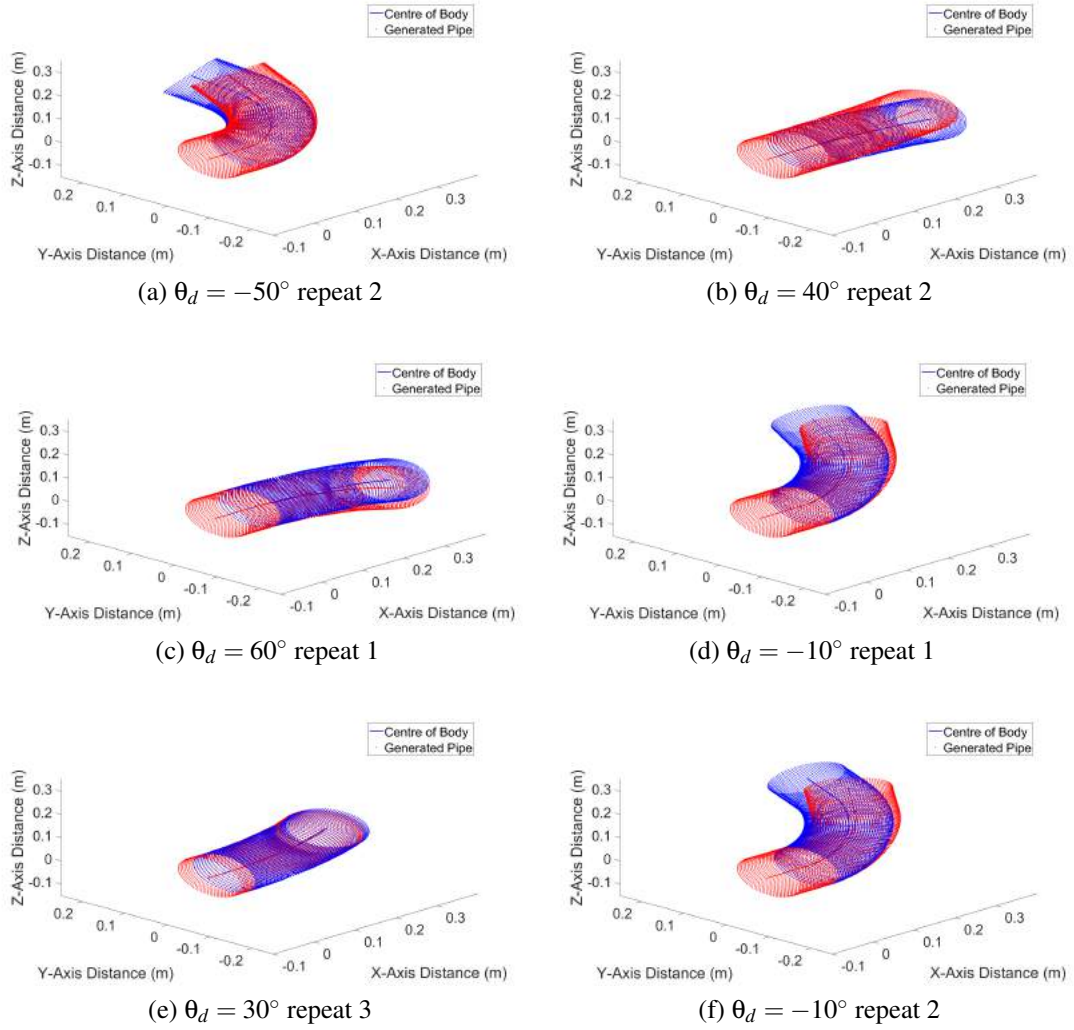


Figure 7.9: Visualisation of real and simulated data

distance estimation system would also improve the system, as the corner angle estimation is based on the distance travelled by the robot.

The visualisation of the real data is human readable, showing a general trend to the direction and angle of the elbows the robot travelled through.

7.8 Limitations

The proposed visualisation is the proof of concept for the final system. The following section discusses some of the limitations of the proposed system and how they could be corrected for in the final system.

Table 7.2: Estimated corner parameters for visualisation system

	Target θ_d ◦	Estimated θ_d ◦	Target ϕ_a ◦	Estimated ϕ_a ◦	Error ◦
(a)	-50	-61.8	90	105.54	15.54
(b)	40	50.09	90	86.17	3.83
(c)	60	52.81	90	95.27	5.27
(d)	-10	-19.82	90	102.58	12.58
(e)	30	30.9	90	93.16	3.16
(f)	-10	-19.72	90	101.74	11.74

Accumulated error poses a large issue to the method, as the distance travelled is determined from only the encoder data on the robot. Slip in the tracks or missed counts from the controller can lead to error building up over time. This means that despite the system being accurate for small pipe networks, if increased to much larger sizes, it may cause very large errors to build up.

It is also the case for the corner direction estimation as the previous value is used to offset the new one when it is being visualised. Error in this estimation could lead to incorrect angles being visualised despite an accurate estimation from the robot. To compensate for the encoder drift, an alternative method of localisation could be used with the data to give a more accurate estimation of the distance travelled. Fusing this data with a more absolute method of positioning would reduce the accumulated error. For the direction estimation, an IMU could be used as the reference for the visualisation, this would introduce its own error to the system but would remove the reliance on the previous estimation, thus removing the accumulation of error.

Unknown rotations pose a challenge for the system as the relative direction of the next elbow to the robot will be different to the previous elbow. This would result in an incorrect visualisation of the elbow direction even though the robot could have an accurate estimation. Similar to the accumulated error an IMU would give a reference to the robot such that rotations could be detected and the elbows correctly visualised.

Visualisation of surface defects is currently not present in the system, the method assumes the pipes are round when generating them. For a future development the feeler data could be used to generate the pipes which would show any deformation or defects the feelers travelled over.

7.9 Summary and Contribution

The contribution of this chapter is a successful method of visualising the data taken from a pipe inspection robot including an initial test of overlaying hotspot data on to it. The method can deal with large networks as the system is based on homogeneous transformations. The visualisation is able to accurately represent elbows with varying directions, angles and radius from only distance and corner parameter estimation data. Despite only being limited to elbows and straights a method of extending the system to work with other junctions such as T-junctions is proposed. Reviewing the visualisation of the real data (shown in Figure 7.9) they are an acceptable representation of the actual elbow used for the AEC experiments.

The extended simulations of networks shown in Section 7.4 that this method of visualisation could be extended to larger real world networks. Reviewing the requirements of the system, the corners angles are within the 15° required accuracy. The distance travelled by the robot is also within the ± 0.5 m tolerance but the robot travelled only a small distance and thus this metric is not fully proved. The discussion of future work will include the possibilities of adding an IMU to the robot to better aid in the visualisation of the networks as well as the inclusion of sensor data.

Blank Page

Chapter 8

Conclusion and Further Work

8.1 Summary

The need for a controlled method of navigating a wall-pressing, differential drive, pipe robot through an unknown pipe network with small pipe size (50 - 150 mm) was identified in Chapter 2. This thesis developed an Autonomous Elbow Controller (AEC) as a solution to that problem.

Before a control action could be calculated, the parameters of the unknown corner need to be detected. Chapter 3 presents a feeler sensor and algorithm to determine the corner direction which can be extended to the major radius. From testing the corner parameter estimation (Chapter 4) it was found to have an absolute mean error of $\bar{\epsilon}_{\theta_d} = 4.69^\circ$ for corner direction and $\bar{\epsilon}_R = 0.91$ mm for radius. This is a good estimate for direction which is comparable with the results of the literature but offers a low-cost and scalable method of detection. For the radius it is the only system to provide practical results from a radius estimation on an in-pipe robot. Comparing this to the requirements of the system from Section 3.3, it is an improvement on the target estimations of $\theta_{d_{target}} = 10^\circ$ for corner direction and 5% for the radius.

To test the controller that was being developed a robot was required. FURO II was designed in Chapter 5, it is a wall-pressing, differential drive, tracked robot that is able to navigate around elbows in 150 mm pipes. It features both active and passive wall-pressing allow it to have some compliance but also able to controllably change its diameter. The aim of the robot was to be a suitable platform to test the AEC by acting as a feeler mount and being able to navigate around an elbow with the appropriate control (Chapter 5). It was successfully able to complete this aim as shown in Chapter 6. The requirements of the robot as highlighted in Section 5.2 have also been achieved.

Once the parameters were estimated and the robot was designed, the full controller could be developed. Chapter 6 presents a method of using the corner parameter estimation to act as an input to the AEC to generate the control action. Once in the elbow the AEC checks for exit conditions, allowing it to navigate through an elbow with any angle (ϕ_a). The AEC was compared with the Brute Force (BF) method, the results showed a decrease in the impulse applied to the robot of $I_{\text{diff}} = 213.97$ Ns when using the AEC. The BF method also caused the robot to become stuck in the pipe which did not occur during any of the 39 AEC passes. This also highlights the need for a differential drive robot to have a controller. The aim of the controller was to propose a suitable method that would be a significant improvement over using the brute force method, which the previous discussion shows has been met.

Finally a visualisation system able to generate a map from the collected data from the robot is designed (Chapter 7). It was able to visualise elbows with varying, angle, direction and radius. It was used to successfully generate visualisations of the AEC tests and showed its extendibility by visualising larger networks from simulated inputs. Comparing the output to the initial aim of the visualisation system ‘To develop a method to generate human readable geometric reconstructions of pipework from the data that would be received from the FURO II robot’ (Chapter 7), it was able to achieve this aim, however improvements to the system could be made to simplify the task for the operators.

8.2 Thesis Analysis

Project Aim: Reviewing the aim of the project from Section 1.3, “The aim of the project is to develop a robotic system that can autonomously navigate through unknown pipe networks, then produce a geometric map of the information gathered.”. It can be seen from the summary above that the aim and objectives (Section 1.3) have been met for networks which only consist of elbows.

The following sections conclude the current progress of the project and discusses how this work could be extended to varying junction types and other improvements of the system. It also involves the further work required to make this system fully deployable in the nuclear environment as well as other industries.

8.2.1 Corner Parameter Estimation

The current progress of the corner parameter estimation is the ability to identify corner direction and radius in an unknown elbow. The direction is thoroughly tested but extensive testing on the radius prediction should be included in further work to correctly characterise the suitability of the algorithm. From analysing the data from the estimation tests, the radius prediction was found to have a mean absolute error of 0.91 mm for a $R = 152.4$ mm elbow. This is a good result with a very small error but is only tested on a single radius.

Also reviewing the results showed, there are differences in the simulated and real estimations. Adding advanced filtering techniques to the feeler sensors would aid in better estimations of the corner parameters.

A particle filter was developed as part of the sensing system for the project. It takes the simulated feeler angles as the state update for the particles then uses the captured data for the measurement update. Using the filter on the data from the corner parameter estimation experiment (Section 4.1) yielded an absolute mean error of $\bar{\epsilon}_{\theta_d} = 11.38^\circ$. Comparing this to the original method ($\bar{\epsilon}_{\theta_d} = 4.69^\circ$) shows that the error is increased when using the particle filter. However, there is potential for the filter to be improved and tuned to better the original method.

8.2.2 In-pipe Obstacles and Junctions

The proposed AEC allows the navigation of networks consisting of elbows. However, to allow the navigation of travelling through more complex networks, methods of using the feeler sensors to detect other junction types should be considered. A method of retracting the feelers would be required for T-junctions as the feeler arm may spring out into an opening which would stop the robot progressing.

Two methods to achieve this would be a central motor to retract all of the feelers, which would only require one extra actuator but makes the mechanical design more complex, or the addition of small motors to the pivot points of the feelers. As example of the latter is the Dynamixel XL series [102], which would also provide angular feedback removing the need for the encoder.

Once the prediction method is extended to other junctions the controller must be developed to also overcome them. A state based approach can be used where each junction type has its own controller state. This would allow for a specific controller for each junction to be developed.

Overcoming T-junctions can be a difficult task as in certain orientations one of the robot's DUs can have no contact with the walls of the pipe. Strategies for overcoming T-junctions with a differential drive robot are presented by Roh and Choi [103] for 8 inch pipes.

Other junctions to consider and test are step and ramp changes in the pipe diameter. FURO II is able to expand and contract between 137.02 - 243.66 mm but it has only been tested in 150 mm pipes. Testing with various step heights and ramp angles should be completed to fully characterise the performance of the prototype.

As part of improving the AEC, the triggering threshold could be tuned to give a more/less accurate entrance and exit threshold for worse/better noise rejection respectively.

8.2.3 Sensing and Visualisation

The visualisation system presented in Chapter 7, provides good reconstructions of the pipework navigated during the AEC testing. However, the accuracy of the system has not been tested on longer, more complex networks. Due to the current method relying on its position from an encoder it is likely to suffer from errors as the distance travelled by the robot become greater.

To improve the accuracy of the localisation system for the robot, the inclusion of an IMU should be considered as it is shown to be successful form the literature (Section 7.2). To combine the data with the encoder data, advanced filtering methods such as an extended Kalman filter could be used. This would not only improve the localisation of the robot but would allow the generated maps to be more accurate as the distance travelled is used to determine the pipe lengths. An IMU could also be used to correctly orientate the map to help with the view for the end user.

External sensing needs to be added to the robot, such as a radiometric sensor. This would allow real sensor data to be overlaid on the visualised pipe networks.

As well as radiometric sensors, other sensors could be added. A camera with live stream to the operator could help with manual identification of objects in the pipeline as well as manual control. Using the feeler data to map the internal dimensions of the pipe could also provide an interesting insight into the conditions of the pipes.

8.2.4 Environmental Hardening

To create a deployable robot for the nuclear environment, hardening the robot to be able to withstand the environmental effects should be considered. As the pipework in question is Post Operational Clean Out (POCO), there should be only small traces of nuclear material and the dose level should not be too high.

To protect from the effects of radiation, shielding can be used. Shielding materials such as lead tend to be very dense and heavy and are more effective when made to be thick. The shielding required may make the robot cumbersome and reduce its lifespan when running on batteries. The robot is also required to work in 50 mm pipes meaning there is very little space for shielding.

Another method of radiation hardening is to be selective with the components used on-board the robot, Nancekievill et al. [104] found power regulators were particularly susceptible to degradation. It also suggests integrated circuits and other electronics could be designed with components that are more radiation tolerant. Methods such as this would allow the robot to keep its small form factor and be hardened to radiation.

During POCO the pipework is flushed with a very acidic solution to help remove any radioactive materials. Residue from the flush may be left in the pipe meaning the materials on the robot must be able to withstand very acidic conditions. Acid resistant plastics and metals should be selected for the manufacturing of the robot. [105] lists some acid resistant materials that could be used as a replacement to the robot's current materials, such as aluminium alloys and Polytetrafluoroethylene (PTFE) plastic. Covers for the electronic components should also be used. This will not only help shield them from the acid but can also help with the decontamination of the robot.

Decontamination is an important factor for the final deployable version of the robot. This will allow the robot to be cleaned down and reused as opposed being disposed of. Wipe clean faces and no traps for contamination are required for this.

Other environmental effects include increased temperatures, which can be overcome by the selection of components that are able to operate in elevated temperatures.

8.2.5 Tether and Communication

The current FURO II robot is tethered, this is to allow for long term running of the robot without the need for changing batteries, which also removes the need for wireless communication. For a final deployable version of the robot it should be tetherless. The addition of a tether within an in-pipe environment can cause excessive drag once the

robot has navigated around junctions. A tether would also be more waste to be disposed after it was used.

To allow the robot to be tetherless all the required power circuitry must be carried on-board the robot. A method of relaying the information back to an operator (if present) will also be required. Extra pods behind the robot could be used to carry excess circuitry and power required by the robot. These pods should be passive and mechanically linked to the robot to allow them to be pushed or pulled. Adding extra pods to the robot would increase the complexity of navigating junctions and the drag on the robot. It also generates more waste when the unit is disposed of.

Communication poses a large issues, Radio Frequency (RF) selection for wireless communication can be difficult as the pipe limits the wavelength that can be used [106]. Other methods of wireless communication can be considered such as acoustics, where the pipe can act as a wave guide for the signal. Branches in the pipeline pose other issues where the signal will be split meaning high powered sources may be required which can reduce the lifespan of the robot when running on battery power.

8.2.6 Retrieval and Autonomous Control

As the robot is tetherless, retrieval poses another problem. Traditionally in-pipe robots have a tether that is reinforced to allow it to be removed in the case it gets lodged. For the FURO II robot this is not an option, therefore any failures in the robot's locomotion method could lead it to become stranded in the pipe. The proposed method to overcome this is the use of failure detection on board the robot. Such as Baghernezhad and Khorasani's [107] work, which is able to detect faults on the robot and Vechet et al.'s [108] which is able to do the same for its sensors. If a fault is detected this could allow the robot to be put into a recovery state and attempt to return to the start of the pipe.

The autonomous control system plays a crucial role in the deployment of the robot for multiple reasons. First it must be able to return to the start of the pipe but it also must be sufficiently robust that no issues occur. This includes knowledge of how to navigate all possible junction types and its own capabilities. I.e. if it reached the end of a pipe to stop and return. Blockages and pipe ends pose a challenge for the robot, a method of autonomously identifying these would be required to stop the robot when they are reached.

Backwards travel will be a requirement of the controller so it is able to return back to where the robot is deployed. As the robot has only one set of sensors, to be able to reverse back through the pipe network, it can use the map it has generated. The

localisation system will have to determine its location on the map. Any errors of the estimation system and undetected rotating in the pipe could lead to incorrectly calculated velocities when the robot is reversing around the junctions. To help reduce this risk a second set of feeler sensors could be added to the rear of the robot which would be able to recompute the corner direction when they are approached. An alternate method to improve this would be a better localisation system and adding an IMU to give it knowledge of its orientation. This information could then be used to give an accurate location on its map and take into account any rotations of the robot.

A small form factor laser range finder could be used to detect the distance of obstacle ahead of the robot. This combined with the feeler data should allow them to be detected. A laser range sensor could also provide another input into the localisation system which could help improve the accuracy.

Coverage algorithms would need to be considered to ensure the largest possible network within the lifespan of the robot. When the robot isn't able to determine its control action, a manual override is already included in the robot's controller.

8.2.7 Miniaturisation

The FURO II prototype is designed for a 150 mm pipe, the final aim of the project is to operate within 50 - 150 mm pipes. Work on miniaturising the robot can be completed. However, new, small, high-torque motors and robot design would be required. Very small pipe inspection robots have been built such as Suzumori et al. [30] as well as many others. This shows making a small form factor in-pipe robot is feasible.

Section 4.2.5 discusses the estimation method when using a 50 mm pipe. It is shown to have a maximum mean error $\epsilon_{\theta_d}^- = 1.81^\circ$ in the predicted angle showing it is still a suitable method in small pipes. Real world testing should be completed to verify this.

8.3 Contribution to Field

The major contributions of the thesis are presented in the following:

1. **A novel feeler sensor and algorithm for the detection of unknown corner parameters.** From practical experimentation it was found to be able to estimate corner direction with an absolute mean error of $\epsilon_{\theta_d} = 4.01^\circ$ and corner radius

with an absolute mean error of $\bar{\epsilon}_R = 0.91$ mm. The corner direction is a comparable solution to the literature but with the ability to scale to smaller pipes and the radius estimation is the first to provide practical results.

2. **The design of a pipe inspection robot for the task of navigating elbows within a 150 mm pipe.** FURO II is a both active and passive wall-pressing, differential drive, tracked, in-pipe robot. It is able to operate in pipes with large diameter range (137.02 - 243.66 mm).
3. **The design of an autonomous controller for the task of navigating a wall-pressing, differential drive, robot around unknown pipe elbows.** The controller is able to navigate around elbows with an unknown, direction, radius and angle. It was tested on an elbow at varying directions and it was shown to be successful by completing all 39 passes through the elbow when using the AEC. It is also a significant improvement over the brute force method leading to a decrease in the impulse applied to the robot of $I_{\text{diff}} = 213.97$ Ns. The extra forces applied to the robot during the brute force method also caused it to become lodged in the pipe, which did not occur during the test with the AEC on the FURO II robot.
4. **A Visualisation System is developed to reconstruct the pipework through which the FURO II robot travelled.** The system uses homogeneous transformation matrices to generate the pipework which allows large complex networks to be mapped and generated. The system takes the sensor outputs from the robot, the encoder counts and feeler predictions. Using this it is able to determine the distances between landmarks (Elbows, Pipes etc.) and generate the visualisation from their estimated parameters. The visualisation system is able to reconstruct elbows with varying radius, angle and direction and is shown to be able to generate complex pipe networks with radiation hotspots also identified on them.

Chapter 9

Appendix

9.1 Electronic Appendix

Please find all contents of the electronic appendix on Mendeley Data: DOI:10.17632/47c9kms7.3

List of Electronic Appendix Contents

Video 9.1: Video of NIVALIS I navigating elbow with manual control and travelling within straight pipe

Video 9.2: Video of FURO I navigating elbow with manual control and travelling within straight pipe

Video 9.3: Video of FURO II navigating elbow with autonomous elbow controller

CAD 9.1: Solidworks files for the design of the FURO II prototype

9.2 Figures

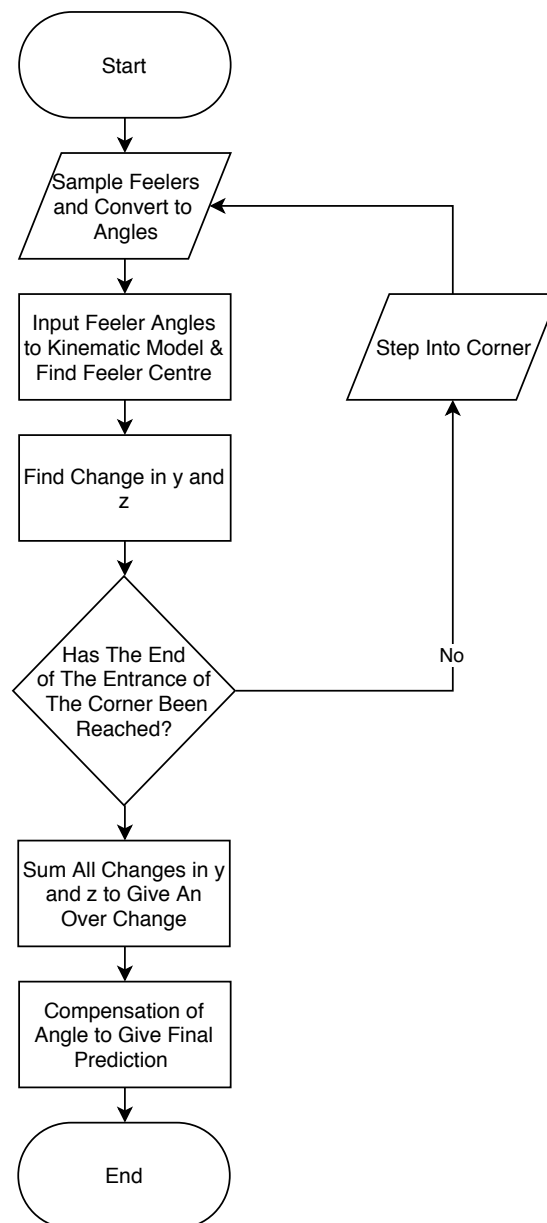


Figure 9.1: Corner Prediction Flow Chart

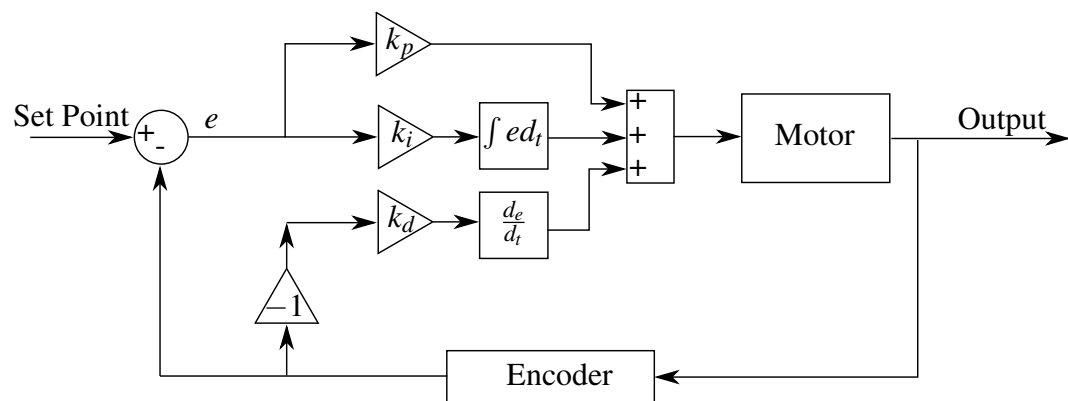


Figure 9.2: PID Controller Architecture

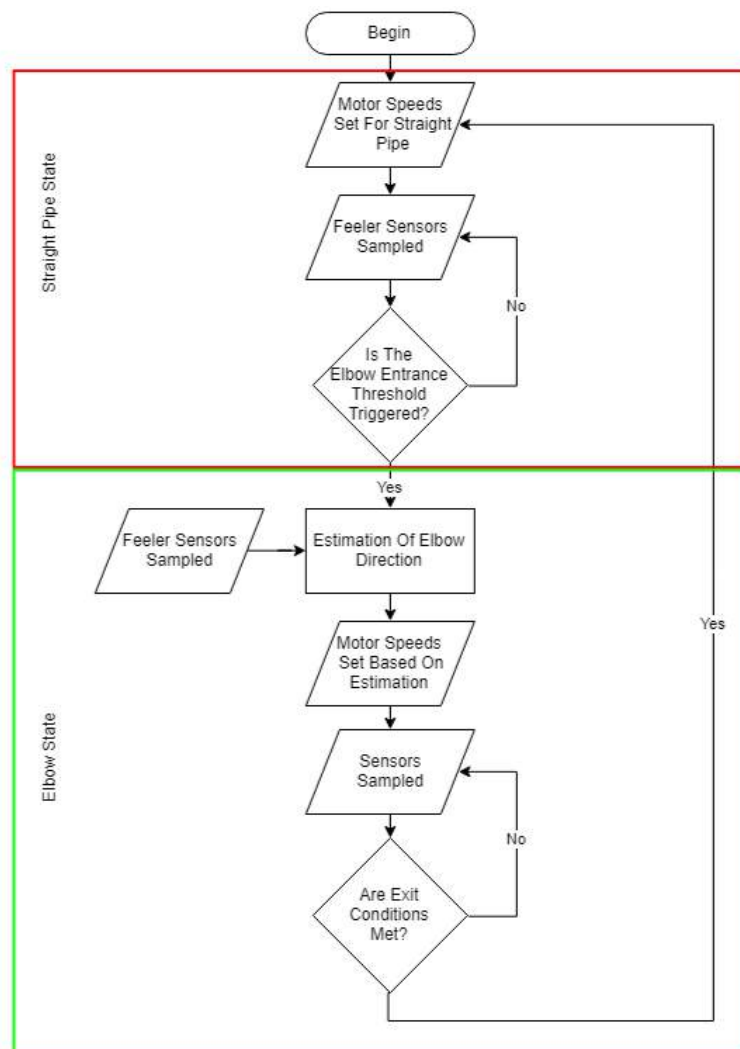


Figure 9.3: Closed-loop Control Architecture

9.3 Tables

Table 9.1: Design parameters of wheeled and tracked, differential drive robots

	Size			Number of		Wall-pressing		Maximum Speed mm s ⁻¹	Weight kg	Tethered	Control	
	Diameter		Length mm	Drive Units	Drive Modules	Passive	Active				Autonomous	Manual
	Min mm	Max mm										
Robots	MRINSPECT VI	150	200	-	3	1	Yes	No	-	Yes	Yes	-
	Choi and Ryew	160	240	-	3	2	Yes	No	-	Yes	Straights	Yes
	MRINSPECT IV	85	109	150	3	1	Yes	No	150	0.7	Yes	Yes
	THES-II	50			2	2	Yes	No	-	-	Yes	Yes
	THES-III	100	200		4	1	Yes	No	-	-	Yes	Yes
	Suzumari et al.	23		110	2	1	No	Limited	6	0.016	Yes	No
	Yoon and Park	110		110	2	1	No	Magnetic	12	0.15	Yes	No
	Kim et al.	600	800	680	3	1	No	Yes	217	80	Yes	No
	PAROYS-II	400	700	390	3	1	Yes	Yes	41.7	7.8	-	Yes
	Sato et al.	69	-	-	1	variable	No	Yes	-	0.613	Yes	-

Table 9.2: Design parameters tracked, differential drive robots

Robot	Size		Length		Number of		Wall-pressing		Maximum	Weight	Tethered	Control	
	Diameter	Max	Min	mm	Drive	Drive	Passive	Active	Speed	kg		Autonomous	Manual
	mm	mm	mm	mm	Units	Modules			mms^{-1}				
Kim et al.	600	800		680	3	1	No	Yes	217	80	Yes	No	Yes
PAROYS-II	400	700		390	3	1	Yes	Yes	41.7	7.8	-	Yes	-
FAMPER	127	157		148	4	1	Yes	No	72.4	-	No	-	Yes
Kwon et al.	75	105		75	3	1	Yes	No	-	-	Yes	No	Yes
PIC	254	508		-	3	1	No	Yes	-	-	Yes	No	Yes
Kakogawa	136	226		235	3	2	Yes	No	230	1.8	Yes	-	-

Bibliography

- [1] Gov.uk, 'Nuclear Provision: the cost of cleaning up Britain's historic nuclear sites - GOV.UK', 2018. [Online]. Available: <https://www.gov.uk/government/publications/nuclear-provision-explaining-the-cost-of-cleaning-up-britains-nuclear-legacy/nuclear-provision-explaining-the-cost-of-cleaning-up-britains-nuclear-legacy>. [Accessed: 12/03/2019].
- [2] C. Wagemans, *The nuclear fission process*. CRC press, 1991.
- [3] Sellafield Ltd., 'Sellafield ltd. Challenge', 2018. [Online]. Available: <http://www.sellafieldsites.com/challenge/>. [Accessed: 29/06/2017].
- [4] Sellafield Ltd., 'History of Sellafield', 2018. [Online]. Available: <https://www.gov.uk/government/organisations/sellafield-ltd/about#history-of-sellafield>. [Accessed: 12/03/2019].
- [5] UK Radioactive Waste Inventory, 'What are the main waste categories?', 2018. [Online]. Available: <https://ukinventory.nda.gov.uk/about-radioactive-waste/what-is-radioactivity/what-are-the-main-waste-categories/>. [Accessed: 12/03/2019].
- [6] UK Radioactive Waste Inventory, 'How do we manage radioactive waste?', 2018. [Online]. Available: <https://ukinventory.nda.gov.uk/about-radioactive-waste/how-do-we-manage-radioactive-waste/>. [Accessed: 12/03/2019].
- [7] Sellafield Ltd, 'Sellafield Magazine Issue 02', 2015. [Online]. Available: <http://www.sellafieldsites.com/wp-content/uploads/2015/12/SEL10536-Q2-Magazine.pdf>. [Accessed: 06/06/2018].
- [8] GameChangers, 'Identifying Unknown Sharps in Gloveboxes - Game Changers - Supporting Sellafield's Nuclear Decommissioning Programme', 2018 [Online].

Available: <https://www.gamechangers.technology/challenges/gloveboxes/>. [Accessed: 30/04/2019].

- [9] EurekaMagazine, ‘The vast task of decommissioning the UK’s nuclear facilities is driving and rewarding technological innovation’, 2018. [Online]. Available: <http://www.eurekamagazine.co.uk/design-engineering-features/technology/the-vast-task-of-decommissioning-the-uks-nuclear-facilities-is-driving-and-rewarding-technological-innovation/182949>. [Accessed: 30/04/2019].
- [10] Health and Safety Executive. ‘Use of Pipeline Standards and Good Practice Guidance’, 2008. [Online]. Available: <http://www.hse.gov.uk/pipelines/resources/pipelinestandards.htm>. [Accessed: 12/03/2019].
- [11] S.-g. Roh and H. R. Choi, “Differential-drive in-pipe robot for moving inside urban gas pipelines,” *IEEE transactions on robotics*, vol. 21, no. 1, pp. 1–17, 2005.
- [12] A. A. F. Nassiraei, Y. Kawamura, A. Ahrary, Y. Mikuriya, and K. Ishii, “Concept and Design of A Fully Autonomous Sewer Pipe Inspection Mobile Robot ”KANTARO”,” in *2007 IEEE International Conference on Robotics and Automation*, pp. 136–143.
- [13] L. Shao, Y. Wang, B. Guo, and X. Chen, “A review over state of the art of in-pipe robot,” in *2015 IEEE International Conference on Mechatronics and Automation (ICMA)*, pp. 2180–2185, Aug 2015.
- [14] S.-g. Roh and H. R. Choi, “Differential-drive in-pipe robot for moving inside urban gas pipelines,” in *IEEE transactions on robotics*, vol. 21, no. 1, pp. 1–17, 2005.
- [15] H.-o. Lim and T. Ohki, “Development of pipe inspection robot,” in *ICCAS-SICE, 2009*, aug 2009, pp. 5717–5721.
- [16] J. Okamoto, J. C. Adamowski, M. S. G. Tsuzuki, F. Buiocchi, and C. S. Camerini, “Autonomous system for oil pipelines inspection,” *Mechatronics*, vol. 9, no. 7, pp. 731–743, 1999.
- [17] A. A. F. Nassiraei, Y. Kawamura, A. Ahrary, Y. Mikuriya, and K. Ishii, “A New Approach to the Sewer Pipe Inspection: Fully Autonomous Mobile Robot

- "KANTARO"," in *IECON 2006 32nd Annual Conference on IEEE Industrial Electronics*. IEEE, pp. 4088–4093.
- [18] S. Ryew, S. H. Baik, S. W. Ryu, K. M. Jung, S. G. Roh, and H. R. Choi, "In-pipe inspection robot system with active steering mechanism," in *Proceedings, 2000 IEEE/RSJ International Conference on Intelligent Robots and Systems (IROS 2000)*, vol. 3. IEEE, pp. 1652–1657.
- [19] K. A. Papadopoulou, M. N. Shamout, B. Lennox, D. Mackay, A. R. Taylor, J. T. Turner, and X. Wang, "An evaluation of acoustic reflectometry for leakage and blockage detection," in *Proceedings of the Institution of Mechanical Engineers, Part C: Journal of Mechanical Engineering Science*, vol. 222, no. 6, pp. 959–966, 2008.
- [20] R. Buckingham and A. Graham, "Nuclear snake arm robots," in *Industrial Robot: An International Journal*, vol. 39, no. 1, pp. 6–11, jan 2012.
- [21] OCRobotics, "LaserSnake," 2015. [Online]. Available: <http://www.ocrobotics.com/lasersnake--nuclear-decommissioning/>. [Accessed: 08/05/2018].
- [22] T. Okada and T. Sanemori, "MOGRER: A vehicle study and realization for in-pipe inspection tasks," *IEEE Journal of Robotics and Automation*, vol. 3, no. 6, pp. 573–582, 1987.
- [23] T. Okada and T. Kanade, "A three-wheeled self-adjusting vehicle in a pipe, FERRET-1," *The International journal of robotics research*, vol. 6, no. 4, pp. 60–75, 1987.
- [24] G. H. Mills, A. E. Jackson, and R. C. Richardson, "Advances in the Inspection of Unpiggable Pipelines," *Robotics*, vol. 6, no. 4, p. 36, 2017.
- [25] J. Okamoto, J. C. Adamowski, M. S. G. Tsuzuki, F. Buiocchi, and C. S. Camerini, "Autonomous system for oil pipelines inspection," *Mechatronics*, vol. 9, no. 7, pp. 731–743, 1999.
- [26] G. Canavese, L. Scaltrito, S. Ferrero, C. F. Pirri, M. Cocuzza, M. Pirola, S. Corbellini, G. Ghione, C. Ramella, F. Verga, A. Tasso, and A. Di Lullo, "A novel smart caliper foam pig for low-cost pipeline inspection-Part A: Design and laboratory characterization," *Journal of Petroleum Science and Engineering*, vol. 127, pp. 311–317, 2015.

- [27] Y. S. Choi, H. M. Kim, H. M. Mun, Y. G. Lee, and H. R. Choi, "Recognition of pipeline geometry by using monocular camera and PSD sensors," *Intelligent Service Robotics*, vol. 10, no. 3, pp. 213–227, jul 2017.
- [28] H. R. Choi and S. M. Ryew, "Robotic system with active steering capability for internal inspection of urban gas pipelines," *Mechatronics*, vol. 12, no. 5, pp. 713–736, 2002.
- [29] S. Hirose, H. Ohno, T. Mitsui, and K. Suyama, "Design of In-pipe Inspection Vehicles for $\phi 25$, $\phi 50$, $\phi 150$ pipes," *IEEE International Conference on Robotics and Automation*, no. May, pp. 2309–2314, 1999.
- [30] K. Suzumori, T. Miyagawa, M. Kimura, and Y. Hasegawa, "Micro inspection robot for 1-inch pipes," *IEEE/ASME Transactions on Mechatronics*, vol. 4, no. 3, pp. 286–292, 1999.
- [31] K. H. Yoon and Y. W. Park, "Design, fabrication, and characterization of in-pipe robot with controllable magnetic force," in *2012 IEEE International Conference on Automation Science and Engineering (CASE)*. IEEE, 2012, pp. 786–789.
- [32] HoneyBee Robotics. 'Pipe Inspection Robot', 2015. [Online]. Available: <http://www.honeybeerobotics.com/portfolio/pipe-inspection-robot/>. [Accessed: 12/03/2019].
- [33] Y.-G. Kim, D.-H. Shin, J.-I. Moon, and J. An, "Design and implementation of an optimal in-pipe navigation mechanism for a steel pipe cleaning robot," in *2011 8th International Conference on Ubiquitous Robots and Ambient Intelligence (URAI)*. IEEE, 2011, pp. 772–773.
- [34] J. Park, T. Kim, and H. Yang, "Development of an actively adaptable in-pipe robot," in *ICM 2009 IEEE International Conference on Mechatronics*. IEEE, 2009, pp. 1–5.
- [35] J. W. Park, W. Jeon, Y. K. Kang, H. S. Yang, and H. Park, "Instantaneous kinematic analysis for a crawler type in-pipe robot," in *2011 IEEE International Conference on Mechatronics (ICM)*. IEEE, 2011, pp. 381–385.
- [36] K. Sato, T. Ohki, and H.-o. Lim, "Development of in-pipe robot capable of coping with various diameters," in *2011 11th International Conference on Control, Automation and Systems (ICCAS)*. IEEE, 2011, pp. 1076–1081.

- [37] X. Yu, Y. Chen, M. Z. Q. Chen, and J. Lam, "Development of a novel in-pipe walking robot," in *2015 IEEE International Conference on Information and Automation*. IEEE, 2015, pp. 364–368.
- [38] S. Savin, S. Jatsun, and L. Vorochaeva, "Trajectory generation for a walking in-pipe robot moving through spatially curved pipes," in *12th International Scientific-Technical Conference on Electromechanics and Robotics "Zavalishin's Readings"- 2017*. . MATEX Web Conf., 2017s, pp. 1–5.
- [39] A. Zagler and F. Pfeiffer, "MORITZ a pipe crawler for tube junctions," in *2003 IEEE International Conference on Robotics and Automation (Cat. No.03CH37422)*, vol. 3. IEEE, pp. 2954–2959.
- [40] J. Gao and G. Yan, "Locomotion Analysis of an Inchworm-Like Capsule Robot in the Intestinal Tract," *IEEE Transactions on Biomedical Engineering*, vol. 63, no. 2, pp. 300–310, feb 2016.
- [41] a.M. Bertetto and M. Ruggiu, "In-pipe inch-worm pneumatic flexible robot," *2001 IEEE/ASME International Conference on Advanced Intelligent Mechatronics. Proceedings (Cat. No.01TH8556)*, vol. 2, no. July, pp. 1226–1231, 2001.
- [42] A. Kakogawa and S. Ma, "Mobility of an in-pipe robot with screw drive mechanism inside curved pipes," in *2010 IEEE International Conference on Robotics and Biomimetics (ROBIO)*. IEEE, 2010, pp. 1530–1535.
- [43] A. Kakogawa, T. Nishimura, and S. Ma, "Development of a screw drive in-pipe robot for passing through bent and branch pipes," in *2013 44th International Symposium on Robotics, ISR*. IEEE, pp. 1–6.
- [44] T. Nishimura, A. Kakogawa, and S. Ma, "Pathway selection mechanism of a screw drive in-pipe robot in T-branches," in *2012 IEEE International Conference on Automation Science and Engineering (CASE)*. IEEE, 2012, pp. 612–617.
- [45] K. Suzumori, S. Wakimoto, and M. Takata, "A miniature inspection robot negotiating pipes of widely varying diameter," in *Proceedings, 2003 IEEE International Conference on Robotics and Automation (ICRA)*, vol. 2. IEEE, 2003, pp. 2735–2740.

- [46] A. Kakogawa and S. Ma, “Design of a multilink-articulated wheeled inspection robot for winding pipelines: AIRo-II,” in *I2016 IEEE/RSJ International Conference on Intelligent Robots and Systems (IROS)*. IEEE, 2016, pp. 2115–2121.
- [47] J.-y. Nagase and F. Fukunaga, “Development of a novel crawler mechanism for pipe inspection,” in *2016 42nd Annual Conference of the IEEE Industrial Electronics Society (IECON)*. IEEE, oct 2016, pp. 5873–5878.
- [48] Q. Li, Y. Sun, H. Liu, M. Zhang, and X. Meng, “Development of an In-Pipe Robot with a Novel Differential Mechanism.” Springer, Singapore, oct 2018, pp. 1079–1097.
- [49] H. M. Kim, Y. S. Choi, Y. G. Lee, and H. R. Choi, “Novel Mechanism for In-Pipe Robot Based on a Multiaxial Differential Gear Mechanism,” *IEEE/ASME Transactions on Mechatronics*, vol. 22, no. 1, pp. 227–235, feb 2017.
- [50] Y. G. Lee, H. M. Kim, Y. S. Choi, H. Jang, and H. R. Choi, “Control strategy of in-pipe robot passing through elbow,” in *2016 13th International Conference on Ubiquitous Robots and Ambient Intelligence (URAI)*. IEEE, aug 2016, pp. 442–443.
- [51] Z. Zhang, G. Meng, and P. Sun, “Kinematic modeling and simulation of wheeled pipe robot in elbow at planar motion stage,” in *2017 2nd Asia-Pacific Conference on Intelligent Robot Systems (ACIRS)*. IEEE, jun 2017, pp. 227–233.
- [52] J. Chen, X. Cao, and Z. Deng, “Kinematic analysis of pipe robot in elbow based on virtual prototype technology,” in *2015 IEEE International Conference on Robotics and Biomimetics (ROBIO)*. IEEE, dec 2015, pp. 2229–2234.
- [53] L. Zhang and X. Wang, “Stable motion analysis and verification of a radial adjustable pipeline robot,” in *2016 IEEE International Conference on Robotics and Biomimetics (ROBIO)*. IEEE, dec 2016, pp. 1023–1028.
- [54] J.-H. Kim, “Sensor-based autonomous pipeline monitoring robotic system,” Ph.D. dissertation, Louisiana State University, 2011.
- [55] J.-S. Lee, S.-g. Roh, H. Moon, H. R. Choi, and Others, “In-pipe robot navigation based on the landmark recognition system using shadow images,” in *Robotics*

- and Automation, 2009. ICRA'09. IEEE International Conference on.* IEEE, 2009, pp. 1857–1862.
- [56] C. H. Lee, D. Joo, G. H. Kim, B. S. Kim, G. H. Lee, and S. G. Lee, “Elbow detection for localization of a mobile robot inside pipeline using laser pointers,” *2013 10th International Conference on Ubiquitous Robots and Ambient Intelligence, URAI 2013*, pp. 71–75, 2013.
- [57] A. S. Zainal Abidin, S. C. Chie, M. H. Zaini, M. F. A. Mohd Pauzi, M. M. Sadini, S. Mohamaddan, A. Jamali, R. Muslimen, M. F. Ashari, and M. S. Jamaludin, “Development of In-Pipe Robot D300: Cornering Mechanism,” *MATEC Web of Conferences*, vol. 87, p. 02029, aug 2017.
- [58] Y. Tamura, I. Kanai, K. Yamada, and H.-o. Lim, “Development of pipe inspection robot using ring-type laser,” in *2016 16th International Conference on Control, Automation and Systems (ICCAS)*. IEEE, oct 2016, pp. 211–214.
- [59] A. Kakogawa, T. Yamagami, Y. Tian, and S. Ma, “Recognition of pathway directions based on nonlinear least squares method,” in *2015 IEEE International Conference on Robotics and Biomimetics (ROBIO)*. IEEE, dec 2015, pp. 1596–1601.
- [60] S. H. Kim, S. J. Lee, and S. W. Kim, “Weaving Laser Vision System for Navigation of Mobile Robots in Pipeline Structures,” *IEEE Sensors Journal*, pp. 1–1, 2018.
- [61] Y. S. Choi, H. M. Kim, J. S. Suh, H. M. Mun, S. U. Yang, C. M. Park, and H. R. Choi, “Recognition of inside pipeline geometry by using PSD sensors for autonomous navigation,” in *2014 IEEE/RSJ International Conference on Intelligent Robots and Systems (IROS)*. IEEE, 2014, pp. 5024–5029.
- [62] D.-H. Lee, H. Moon, and H. R. Choi, “Autonomous navigation of in-pipe working robot in unknown pipeline environment,” in *2011 IEEE International Conference on Robotics and Automation (ICRA)*. IEEE, 2011, pp. 1559–1564.
- [63] T. Pipe and M. J. Pearson, “Whiskered Robots,” in *Scholarpedia of Touch*. Paris: Atlantis Press, 2016, pp. 809–815.
- [64] M. Kaneko and T. Tsuji, “A whisker tracing sensor with 5 μm sensitivity,” in *Proceedings, 2000 ICRA. Millennium Conference. IEEE International*

- Conference on Robotics and Automation. Symposia Proceedings (Cat. No.00CH37065)*, vol. 4. IEEE, pp. 3907–3912.
- [65] D. Jung and A. Zelinsky, “Whisker Based Mobile Robot Navigation,” in *Proceedings of IEEE/RSJ International Conference on Intelligent Robots and Systems. IROS*. IEEE/RSJ, 1996, pp. 497–504.
- [66] R. Russell, “Using tactile whiskers to measure surface contours,” in *Proceedings, 1992 IEEE International Conference on Robotics and Automation*. IEEE Comput. Soc. Press, pp. 1295–1299.
- [67] M. H. Evans, C. W. Fox, N. F. Lepora, M. J. Pearson, J. C. Sullivan, and T. J. Prescott, “The effect of whisker movement on radial distance estimation: a case study in comparative robotics,” in *Frontiers in Neurorobotics*, vol. 6, p. 12, jan 2013.
- [68] N. J. Cowan, E. J. Ma, M. Cutkosky, and R. J. Full, “A Biologically Inspired Passive Antenna for Steering Control of a Running Robot,” in *Robotics Research. The Eleventh International Symposium* Springer, Berlin, Heidelberg, 2014, pp. 541–550.
- [69] Jusuk Lee, S. Sponberg, O. Loh, A. Lamperski, R. Full, and N. Cowan, “Templates and Anchors for Antenna-Based Wall Following in Cockroaches and Robots,” in *IEEE Transactions on Robotics*, vol. 24, no. 1, pp. 130–143, feb 2008. [Online].
- [70] A. Lamperski, O. Loh, B. Kutscher, and N. Cowan, “Dynamical Wall Following for a Wheeled Robot Using a Passive Tactile Sensor,” in *Proceedings of the 2005 IEEE International Conference on Robotics and Automation*. IEEE, pp. 3838–3843.
- [71] Math Open Reference. ‘Radius of an Arc or Segment’, 2011. [Online]. Available: <http://www.mathopenref.com/arcradius.html>. [Accessed: 12/03/2019].
- [72] SparkFun, “Hybrid Linear Actuators,” 2019. [Online]. Available: <https://cdn.sparkfun.com/datasheets/Robotics/39BYGL.pdf>. [Accessed: 10/06/2019].
- [73] R. Inc., “12V DC Motor 146RPM w/Encoder,” 2019. [Online]. Available: <https://www.robotshop.com/eu/en/12v-dc-motor-146rpm-encoder.html>. [Accessed: 10/06/2019].

- [74] Robotshop, “Hokuyo UBG-04LX-F01 (Rapid URG) Scanning Laser Rangefinder - RobotShop,” 2019. [Online]. Available: <https://www.robotshop.com/en/hokuyo-ubg-04lx-f01-laser-rangefinder.html>. [Accessed: 10/06/2019].
- [75] Pololu, “Pololu - Sharp GP2Y0A41SK0F Analog Distance Sensor 4-30cm,” 2019. [Online]. Available: <https://www.pololu.com/product/2464>. [Accessed: 10/06/2019].
- [76] Amazon, “Logitech, C920 HD Pro Webcam,” 2019. [Online]. Available: <https://www.amazon.co.uk/Logitech-C920-Pro-Webcam-Recording/dp/B006A2Q81M>. [Accessed: 10/06/2019].
- [77] RS Components, “53AAA-B28-A15L — Bourns 1 Gang Rotary Cermet Potentiometer,” 2017. [Online]. Available: <https://uk.rs-online.com/web/p/potentiometers/7899428/>. [Accessed: 10/06/2019].
- [78] M. M. Moghaddam¹ and A. Hadi, “Control and Guidance of a Pipe Inspection,” *International Symposium on Automation and Robotics in Construction*, vol. 1001, no. 3128, pp. 1–5, 2005.
- [79] J.-H. Kim, G. Sharma, and S. S. Iyengar, “FAMPER: A fully autonomous mobile robot for pipeline exploration,” in *2010 IEEE International Conference on Industrial Technology (ICIT)*. IEEE, 2010, pp. 517–523.
- [80] Y.-S. S. Kwon, E.-J. J. Jung, H. Lim, B.-J. J. Yi, Y.-s. K. E.-j. Jung, and H. Lim, “Design of a reconfigurable indoor pipeline inspection robot,” in *International Conference on Control, Automation and Systems (ICCAS)*. IEEE, 2007, pp. 712–716.
- [81] M. M. Moghaddam and A. Hadi, “Control and guidance of a pipe inspection crawler (PIC),” in *Proc. International Symposium on Automation, Robotics*, 2005, pp. 11–14.
- [82] A. Kakogawa, S. Ma, and S. Hirose, “An in-pipe robot with underactuated parallelogram crawler modules,” in *2014 IEEE International Conference on and Automation (ICRA)*. IEEE, 2014, pp. 1687–1692.
- [83] Pololu, ‘Pololu 30T Track Set - White’, 2019. [Online]. Available: <https://www.pololu.com/product/3035/pictures>. [Accessed: 12/03/2019].

- [84] Motionco, ‘Worm Gearmotor, Ratio 950:1’, 2019. [Online]. Available: <http://www.motionco.co.uk/worm-gearmotor-ratio-9501-p-644.html>. [Accessed: 12/03/2019].
- [85] L. Brown, J. Carrasco, S. Watson, and B. Lennox, “Elbow Detection in Pipes for Autonomous Navigation of Inspection Robots,” *Journal of Intelligent & Robotic Systems*, pp. 1–15, aug 2018.
- [86] L. Brown, J. Carrasco, S. Watson, and B. Lennox, “FURO: Pipe Inspection Robot for Radiological Characterisation,” in *UK-RAS Proceedings*, vol. 1, no. 1, 2017, pp. 56 – 58.
- [87] Go3D Print, “Tough Resin 1L Cartridge for Form 2 - Go-Print3D,” 2019. [Online]. Available: <https://www.goprint3d.co.uk/formlabs-tough-resin-cartridge>. [Accessed: 06/06/2019].
- [88] M. Quigley, J. Faust, T. Foote, and J. Leibs, “ROS: an open-source Robot Operating System,” *willowgarage.com*.
- [89] B. Beauregard, “Arduino Playground - PIDLibrary,” 2019. [Online]. Available: <https://playground.arduino.cc/Code/PIDLibrary/>. [Accessed: 29/05/2019].
- [90] Bourns, “EMS22A - Non-Contacting Absolute Encoder,” 2017. [Online]. Available: <https://www.bourns.com/docs/product-datasheets/EMS22A.pdf>. [Accessed: 03/06/2019].
- [91] N. M. Yatim, R. L. A. Shauri, and N. Buniyamin, “Automated mapping for underground pipelines: An overview,” in *Electrical, Electronics and System Engineering (ICEESE), 2014 International Conference on*. IEEE, 2014, pp. 77–82.
- [92] D. D. S. Santana, N. Maruyama, and C. M. Furukawa, “Estimation of trajectories of pipeline PIGs using inertial measurements and non linear sensor fusion,” in *2010 9th IEEE/IAS International Conference on Industry Applications (INDUSCON)*. IEEE, nov 2010, pp. 1–6.
- [93] U. Ekpemu and S. Aloba, “Pipeline Laser Imaging and Metrology Using Laser Smart Pig,” in *Nigeria Annual International Conference and Exhibition*. Society of Petroleum Engineers, apr 2010.

- [94] J. T. Thielemann, G. M. Breivik, and A. Berge, "Pipeline landmark detection for autonomous robot navigation using time-of-flight imagery," in *2008 IEEE Computer Society Conference on Computer Vision and Pattern Recognition Workshops*. IEEE, jun 2008, pp. 1–7.
- [95] P. Hansen, H. Alismail, P. Rander, and B. Browning, "Pipe mapping with monocular fisheye imagery," in *2013 IEEE/RSJ International Conference on Intelligent Robots and Systems*. IEEE, nov 2013, pp. 5180–5185.
- [96] S. El Kahi, D. Asmar, A. Fakh, J. Nieto, and E. Nebot, "A vision-based system for mapping the inside of a pipe," *2011 IEEE International Conference on Robotics and Biomimetics, ROBIO 2011*, no. 1, pp. 2605–2611, 2011.
- [97] S.-G. Roh, D. W. Kim, J.-S. Lee, H. Moon, and H. R. Choi, "In-pipe Robot Based on Selective Drive Mechanism," *International Journal of Control, Automation, and Systems*, vol. 7, no. 1, pp. 105–112, 2009.
- [98] P. Zhang, C. Hancock, L. Lau, and G. Wyn Roberts, "Integration of low cost IMU and odometer for underground 3D pipeline mapping Algorithms and Stochastic models for Positioning, Tracking and Navigation View project," Tech. Rep., 2016.
- [99] F. Tache, F. Pomerleau, W. Fischer, G. Caprari, F. Mondada, R. Moser, and R. Siegwart, "MagneBike: Compact magnetic wheeled robot for power plant inspection," in *2010 1st International Conference on Applied Robotics for the Power Industry (CARPI 2010)*. IEEE, oct 2010, pp. 1–2.
- [100] D. H. Lee, H. Moon, J. C. Koo, and H. R. Choi, "Map building method for urban gas pipelines based on landmark detection," *International Journal of Control, Automation and Systems*, vol. 11, no. 1, pp. 127–135, 2013.
- [101] L. R. Groves, *Now it can be told: The story of the Manhattan Project*. Da Capo Press, 1983.
- [102] Dynamixel, 'Dynamixel CL 320', 2019. [Online]. Available: <http://www.robotis.us/dynamixel-xl-320/>. [Accessed: 12/03/2019].
- [103] Se-gon Roh and Hyoukryeol Choi, "Strategy for navigation inside pipelines with differential-drive inpipe robot," in *Proceedings, 2002 IEEE International*

- Conference on Robotics and Automation (Cat. No.02CH37292)*, vol. 3. IEEE, pp. 2575–2580.
- [104] M. Nancekievill, S. Watson, P. R. Green, and B. Lennox, “Radiation Tolerance of Commercial-Off-The-Shelf Components Deployed in an Underground Nuclear Decommissioning Embedded System,” in *2016 IEEE Radiation Effects Data Workshop (REDW)*. IEEE, 2016, pp. 1–5.
- [105] “Acid-Resistant Materials,” in *The Great Soviet Encyclopedia, 3rd Edition*, 3rd ed, 1979.
- [106] T. Nagashima, Y. Tanaka, and S. Ishihara, “Measurement of wireless communication characteristics in sewer pipes for sewer inspection systems using multiple wireless sensor nodes,” in *2015 IEEE 26th Annual International Symposium on Personal, Indoor, and Mobile Radio Communications (PIMRC)*. IEEE, aug 2015, pp. 2055–2060.
- [107] F. Baghernezhad and K. Khorasani, “Computationally intelligent strategies for robust fault detection, isolation, and identification of mobile robots,” in *Neurocomputing*, vol. 171. Elsevier, 2016, pp. 335–346.
- [108] S. Vechet, J. Krejsa, and K.-S. Chen, “Sensor failure detection in autonomous mobile robot application,” in *Proceedings, 16th International Conference on Mechatronics - Mechatronika 2014*. IEEE, dec 2014, pp. 375–380